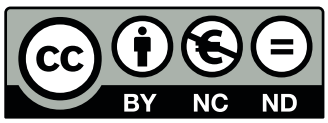
Beyond slurry cast: battery electrodes by design

Samuel Hair

Department of Materials
Imperial College London

This thesis is submitted for the degree of *Doctor of Philosophy.*



This thesis is the result of my own work and includes nothing which is the outcome of work done in collaboration except as declared in the preface and specified in the text. It is not substantially the same as any work that has already been submitted before for any degree or other qualification except as declared in the preface and specified in the text. It does not exceed the prescribed word limit for the Degree Committee.

Samuel Hair (2023)

The copyright of this thesis rests with the author. Unless otherwise indicated, its contents are licensed under a Creative Commons Attribution-Non Commercial-No Derivatives 4.0 International Licence (CC BY-NC-ND). Under this licence, you may copy and redistribute the material in any medium or format on the condition that; you credit the author, do not use it for commercial purposes and do not distribute modified versions of the work. When reusing or sharing this work, ensure you make the licence terms clear to others by naming the licence and linking to the licence text. Please seek permission from the copyright holder for uses of this work that are not included in this licence or permitted under UK Copyright Law.

Executive summary

All commercial battery electrodes today are manufactured by slurry-casting active material powder on to a metal current collector foil. This manufacturing process has been proven over decades and is embedded, but the resulting electrodes limit cell performance. This thesis documents a quantitative, first-principles re-design of the battery electrode for improved gravimetric energy density at commercial cell level.

First, an existing commercial lithium-ion battery is quantitatively analysed to establish a baseline and identify the key sources of loss. The LGM50 cell only achieves 52% of its theoretical gravimetric energy density at a discharge rate of 0.1C, and less than 20% at a discharge rate of 4C. This finding highlights that there is potentially substantial opportunity to improve cell performance using existing cell chemistries. Inactive materials and overpotentials are identified as the key sources of loss, prompting research into the design of a low inactive mass, low overpotential battery electrode.

Next, pyrolytic graphite sheet is identified as a promising material for manufacture of a low inactive mass, low overpotential electrode. However, initial trials reveal very low gravimetric active material capacity of less than $10\,\mathrm{mA\,h\,g^{-1}}$. Laser drilling to form channels is successfully demonstrated and used to manufacture pyrolytic graphite sheet electrodes with arrays of electrolyte channels. Following the introduction of electrolyte channels, the gravimetric active material capacity of pyrolytic graphite sheet is measured to increase by a factor of 40 to $450\,\mathrm{mA\,h\,g^{-1}}$.

Although gravimetric active material capacity is a useful metric for assessing the extent of lithiation of novel active materials, it is insufficient for designing an improved commercial cell. A model is therefore developed to estimate the gravimetric energy density of a commercial cell from electrode characterisation data. This model reveals that the manufactured pyrolytic graphite sheet electrodes would severely restrict the gravimetric energy density of a commercial cell, despite having high gravimetric active material capacity. The manufactured electrodes perform poorly due to low areal capacity and high electrode porosity, highlighting that their design needs to be optimised for use in a commercial cell. The model is deployed as a web app to help other researchers contextualise their research.

Finally, the design of a practical pyrolytic graphite sheet electrode is investigated. The gravimetric energy density of a commercial cell that incorporates pyrolytic graphite sheet electrodes is a strong function of gravimetric active material capacity and electrode porosity. These two parameters are themselves interdependent and a function of several other parameters. A two-step model is developed to estimate the gravimetric active material capacity and then the gravimetric energy density of a commercial cell for a given electrode design. Using the model, the channel diameter and pitch of a pyrolytic graphite sheet electrode is optimised for improved gravimetric energy density at commercial cell level. Results show that whilst channel diameter should be minimised, the channels should not be too closely packed to avoid excessive porosity. A pyrolytic graphite sheet electrode with a hexagonal array of 5 µm diameter, 20 µm pitch channels could increase the gravimetric energy density of a LGM50 cell by 15% to $302\,\mathrm{W\,h\,kg^{-1}}$.

Contents

1 The world needs better batteries **13**
1.1 Better batteries are essential for a transition away from fossil fuels 13
1.2 Designing a better battery 16

2 The modern lithium-ion battery **18**
2.1 Battery fundamentals 18
2.2 The modern lithium-ion battery 20
2.2.1 Active materials 21
2.2.2 Electrolyte 24
2.2.3 Commercial electrodes 25
2.2.4 Commercial cells 26
2.3 Battery modelling fundamentals 27
2.3.1 Conservation and transport of mass 28
2.3.2 Conservation and transport of charge 31
2.3.3 Closing the model 32
2.3.4 Modelling in practice 32

3 A quantitative assessment of commercial cell energy density **34**
3.1 Establishing baseline gravimetric energy density 34
3.2 Identifying the losses 37
3.3 Understanding the losses 39
3.3.1 Inactive materials 40
3.3.2 Overpotentials 42
3.4 Conclusions 45
3.5 Methods 46

4 Proof of concept: Patterned pyrolytic graphite sheet electrodes **50**
4.1 Battery electrodes today 50
4.1.1 Low overpotential electrodes 51
4.1.2 Low inactive material content electrodes 53
4.2 Graphite feedstocks 54
4.3 Pyrolytic graphite sheet 56
4.4 Creating through-plane channels in pyrolytic graphite sheet 59
4.5 Electrode manufacture 60
4.6 Electrode characterisation 61
4.6.1 Discharge-charge rate ramp 62
4.6.2 Extended cycling at 1C 64
4.7 Gravimetric surface area 66
4.8 Effective conductivity 68

4.9 Conclusions . . . 68
4.10 Methods . . . 70

5 Estimating commercial cell performance from laboratory results 79
5.1 Normalising to active material mass . . . 79
5.2 Estimating gravimetric energy density of a commercial cell . . . 82
5.2.1 Existing material-to-cell models . . . 83
5.2.2 Model inputs . . . 83
5.2.3 Model calculation . . . 85
5.2.4 Model deployment . . . 86
5.3 Using the model . . . 87
5.4 Conclusions . . . 93
5.5 Methods . . . 94

6 Design of a low inactive mass, low overpotential battery electrode 100
6.1 Assuming complete lithiation . . . 100
6.1.1 A non-porous pyrolytic graphite sheet electrode . . . 101
6.1.2 A porous pyrolytic graphite sheet electrode . . . 103
6.2 Estimating gravimetric active material capacity . . . 107
6.3 Conclusions . . . 119
6.4 Methods . . . 121

7 Conclusions and further work 123
7.1 A design methodology for battery electrodes . . . 124
7.2 Structured, monolithic electrodes . . . 126
7.3 Future work . . . 127

A Supplementary information 143
A.1 Feasibility of laser cutting pyrolytic graphite sheet . . . 143
A.2 Planar diffusion . . . 150

List of Tables

3.1 Summary of parametrisation data for LGM50 cell 41
3.2 Summary of Batemo performance data for LGM50 cell 47

4.1 Specification of the Oxford Lasers A series micromachining system 71
4.2 Five different electrode types were manufactured. 71
4.3 Protocol for half cell galvanostatic cycling 74

5.1 Summary of parameters for normalisation model 84

6.1 Summary of parameters for gravimetric active material capacity model 109

List of Figures

1.1 Global energy flow by sector . . . 14
1.2 Historic global lithium-ion battery demand . . . 15
1.3 Graphical summary of thesis chapters . . . 17

2.1 Average discharge potential for typical lithium-ion battery active materials plotted as a function of gravimetric active material capacity . . . 22

3.1 Commercial cells are complex systems that span multiple length scales . . . 35
3.2 Ragone plot for commercial lithium-ion cells in Batemo data set . . . 36
3.3 Schematic showing a practical and theoretical LGM50 cell cross-section . . . 38
3.4 Gravimetric energy density of the practical and theoretical LGM50 cell . . . 39
3.5 A break down of the losses for gravimetric energy density of a commercial cell . 40
3.6 Mass and volume loadings of individual components in LGM50 jelly roll . . . 41
3.7 A Pareto of solid and electrolyte mass by component for the LGM50 cell . . . 43
3.8 A schematic of the overpotentials that exist in a battery during charging . . . 45
3.9 Dimensions of LGM50 21700 cell casing . . . 48

4.1 Schematic showing electrode manufacture with the slurry cast process . . . 51
4.2 Optical image and scanning electron micrographs for pyrolytic graphite sheet . . 57
4.3 Optical micrographs of laser drilled pyrolytic graphite sheet . . . 60
4.4 CAD model of pyrolytic graphite sheet patterned with hexagonal array of channels 60
4.5 Characterisation data for the pyrolytic graphite sheet electrodes . . . 62
4.6 Galvanostatic cycling data at different discharge-charge rates . . . 63
4.7 Galvanostatic cycling data for 100 cycles at a discharge-charge rate of 1C . . . 65
4.8 Gravimetric surface area of a hexagonal unit cell . . . 66
4.9 Estimating effective conductivity of a sheet with channels . . . 67
4.10 Components of a coin cell stack . . . 73
4.11 Raw data for galvanostatic discharge-charge cycling . . . 74
4.12 Irreversible capacity during first cycle of galvanostatic discharge-charge cycling . 75
4.13 Couloumbic efficiency during galvanostatic discharge-charge cycling . . . 75

5.1 Schematic showing active material, dry electrode and wet electrode . . . 80
5.2 Galvanostatic discharge-charge data normalised to active material, dry electrode and wet electrode mass . . . 81
5.3 Calculation of cylindrical cell energy density from laboratory measurements . . . 85
5.4 Screenshot of model deployed as web app. . . . 87
5.5 Full cell stacks based on 25 µm thickness pyrolytic graphite sheet electrodes . . . 88
5.6 Mass and volume breakdown for LGM50 cell using 25 µm thickness pyrolytic graphite sheet electrodes . . . 90

5.7 Model results with areal capacity of the pyrolytic graphite sheet cells matched to the LGM50 cell . . . 91
5.8 Mass and volume breakdown for LGM50 cell using pyrolytic graphite sheet electrodes with matched areal capacity . . . 92

6.1 Schematic showing LGM50 cell with non-porous pyrolytic graphite sheet . . . 101
6.2 Schematic showing the replacement of the negative electrode of a LGM50 cell with pyrolytic graphite sheet in 2 steps . . . 102
6.3 Gravimetric energy density as function of pyrolytic graphite sheet porosity . . . 104
6.4 Full cell stacks for pyrolytic graphite sheet with porosity . . . 105
6.5 A schematic of the different stacks and associated gravimetric energy densities . 106
6.6 Hexagonal unit cell geometry used for COMSOL model . . . 108
6.7 Lithium concentration in the hexagonal unit cell when surface concentration reached cut-off value . . . 110
6.8 Gravimetric active material capacity as a function of channel diameter and channel pitch . . . 112
6.9 Two-step model to predict gravimetric energy density for a pyrolytic graphite sheet electrode . . . 113
6.10 Parameter sweep for values of channel diameter between 5 µm and 100 µm and values of porosity between 5% and 40% . . . 114
6.11 Parameter sweep for values of channel diameter between 2 µm and 20 µm and values of porosity between 5% and 75% . . . 115
6.12 Full cell stacks for manufactured and optimised pyrolytic graphite sheet electrode designs . . . 116
6.13 Computer-aided design drawings for the LGM50 stack with manufactured pyrolytic graphite sheet electrode design . . . 118
6.14 Computer-aided design drawings for the LGM50 stack with optimised pyrolytic graphite sheet electrode design . . . 118

7.1 A design methodology for battery electrodes . . . 125

A.1 Rectangular arrays of 100 µm diameter channels . . . 144
A.2 Scanning electron micrographs showing deposition of metal on pyrolytic graphite sheet . . . 145
A.3 Scanning electron micrographs showing percussion drilled channel . . . 146
A.4 Scanning electron micrographs showing arrays of laser drilled channels . . . 146
A.5 Scanning electron micrographs of percussion drilled channels . . . 147
A.6 Scanning electron micrographs showing results of on-the-fly drilling trial . . . 149
A.7 Optical micrographs of channel arrays with 10 µm or 20 µm pitch . . . 150
A.8 Optical micrograph showing arrays of cut channels . . . 151
A.9 Planar diffusion model for constant charge rate . . . 153

Nomenclature

c	Concentration [$\mathrm{mol\,m^{-3}}$]
D	Diffusivity [$\mathrm{m^2\,s^{-1}}$]
F	Faraday constant [$\mathrm{A\,s\,mol^{-1}}$]
i	Current density [$\mathrm{A\,m^{-2}}$]
j	Reaction current density [$\mathrm{A\,m^{-2}}$]
N	Molar flux [$\mathrm{mol\,m^{-2}\,s^{-1}}$]
Q	Capacity [$\mathrm{mA\,h\,g^{-1}}$]
t	Transference number [-]

Greek symbols

η	Overpotential [V]
μ	Chemical potential [$\mathrm{J\,mol^{-1}}$]
ϕ	Electrical potential [V]
σ	Electrical conductivity [$\mathrm{S\,m^{-1}}$]

List of abbreviations

NAM	Negative active material
PAM	Positive active material
SOC	State of charge

Glossary

(Dis)charge rate

The current during discharge or charge expressed as a fraction of the current that would discharge or charge the cell in 1 hour.

Capacity

The amount of charge delivered by a fully charged cell when discharged under specified conditions of load and temperature. For instance, the LGM50 data sheet [1] specifies a nominal capacity of a constant current charge at 0.3C to 4.2 V followed by a constant voltage hold until charging current falls to 0.01C. The cell is then discharged within one hour after reaching full charge to measure nominal capacity. The cell is discharged at 0.2C to 2.50 V. All steps are performed at a room temperature of $25 \pm 2\,^{\circ}\mathrm{C}$. The nominal capacity is the capacity reported in the manufacturer's data sheet.

State of charge

The ratio of the available capacity at low discharge rate to the nominal capacity [2].

Current (continuous)

The highest current for complete cell discharge (10% residual state of charge) without overheating. Measured using constant current discharge from 100% state-of-charge at 25 °C until either the cut-off voltage of 2.5 V is reached or the surface temperature reaches 90% of maximum (e.g. 90% of 70 °C= 63 °C) [3].

Current (peak)

The highest current the cell can deliver for 5 minutes without exceeding a surface temperature of 70 °C. Measured using constant current discharge from 100% state-of-charge at 25 °C until either the cut-off voltage of 2.5 V is reached or the surface temperature reaches 70 °C [3].

Energy

The amount of energy delivered by a fully charged battery when discharged under specified conditions of load and temperature. Calculated as the product of the (nominal) capacity measurement and the average voltage during this measurement.

Power (continuous)

The highest power for complete cell discharge (10% residual state of charge) without overheating [3]. Calculated as the product of the continuous current measurement and the average voltage during this measurement.

Power (peak)

The highest power the cell can deliver for 5 minutes without exceeding a surface temperature of 70 °C [3]. Calculated as the product of the peak current measurement and the average voltage during this 5 minute measurement.

Gravimetric energy density

The amount of energy delivered per unit mass by a fully charged battery when discharged under specified conditions of load and temperature. Calculated by dividing the energy by the cell mass.

Volumetric energy density

The amount of energy delivered per unit volume by a fully charged battery when discharged under specified conditions of load and temperature. Calculated by dividing the energy by the external cell volume.

Active material

An electrochemically active material that directly participates in the electrochemical reactions that allow the battery to store and release energy [4].

Inactive material

A material that does not participate directly in the electrochemical reactions that allow the battery to store and release energy.

Gravimetric active material capacity

The capacity normalised to the mass of active material.

Chapter 1

The world needs better batteries

1.1 Better batteries are essential for a transition away from fossil fuels

A transition away from fossil fuels is necessary to both avert climate disaster and help defuse geopolitical tensions [5]. The problem is that modern society runs on fossil fuels. In 2019, 81% of global primary energy generation (165 PW h) was from fossil fuels [6]. There are two key parts to a transition away from fossil fuels: energy generation and energy storage.

The first part of a transition away from fossil fuels is to replace fossil fuel supplies with renewable energy supplies. Renewables and biomass only accounted for 19% of primary global energy generation in 2019. Non-biomass renewables such as solar, wind and hydro-power are being rolled out worldwide and are expected to account for 50% of global energy generation in 2050 [5]. Meanwhile, biomass energy generation is under scrutiny and without proper regulation could release more carbon into the atmosphere than burning gas or coal [7]. It is interesting to note that only 36% of the global primary energy generation today is used for useful work and heat (Figure 1.1) [6]. If renewables are more efficiently converted into useful work and heat then the required primary energy generation could be much lower.

Fossil fuels do not just, however, allow energy to be generated. Fossil fuels are a convenient chemical store of energy that permits spatial and temporal separation of energy generation and demand. Transportation and grid stability both rely on the storage and transport of fossil

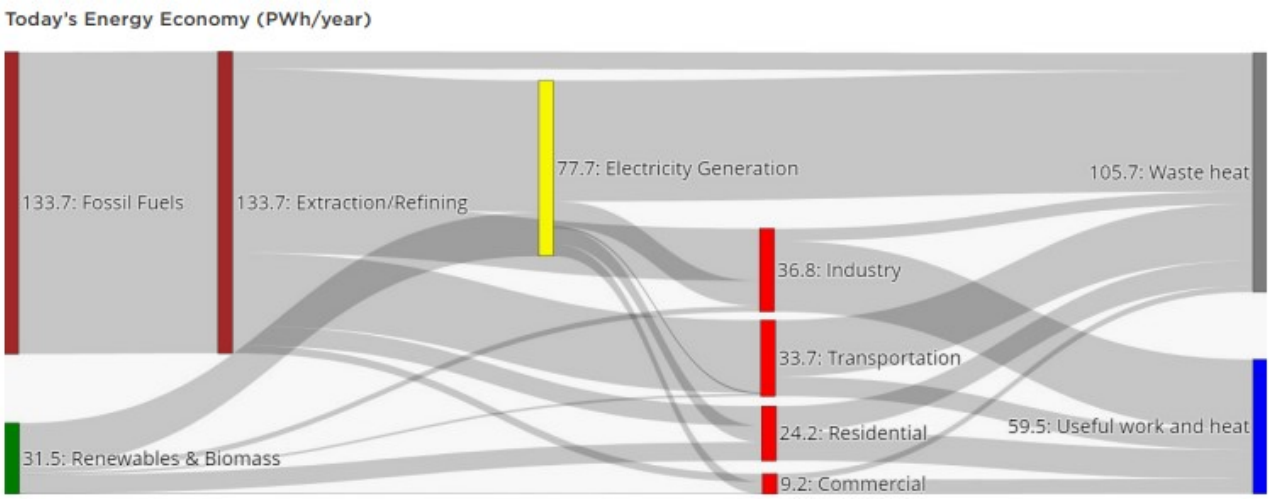


Figure 1.1: Global energy flow by sector (IEA & Tesla analysis) as presented in Tesla Master Plan [6]. In 2019, 81% of global primary energy generation (165 PW h) was from fossil fuels. Most of these fossils fuels are consumed directly by industry, transportation and residential and commercial users rather than as electricity. Only 36% of global primary energy generation today is used for useful work and heat.

fuels for combustion on demand [8, 9]. As shown in Figure 1.1, most of the energy supply to industry and transportation is directly as fossil fuels rather than electricity. Conversely, the key renewable energy supplies that we have today (primarily wind and solar) are both intermittent and cannot be directly stored. The second crucial part of this transition away from fossil fuels is therefore to deploy significant energy storage capacity.

Batteries are an efficient and portable means of storing electrical energy as chemical energy. Lithium-ion batteries were first commercialised by Sony in 1991 [10]. Compared to the original 80 W h kg^{-1} and 200 W h L^{-1} cell [11], both gravimetric and volumetric energy density of lithium-ion batteries have since increased by 3-4 times [12]. The price of a lithium-ion cell has also almost dropped below 100 \$/kWh [13]. These improvements have opened up new markets, such as consumer electronics and transportation, and lithium-ion batteries dominate today as the storage system of choice for portable applications.

Lithium-ion batteries are essential for electrification of road transport and, accordingly, demand has soared. Global demand for lithium-ion batteries increased by 8 times from 90 GWh/year to over 700 GWh/year in the 7 year period from 2015 to 2022 (Figure 1.2) [14]. This increase was primarily driven by new demand for passenger electric vehicles (EVs). By 2030, demand is forecast to increase by a further 6 times to 4700 GWh/year, largely due to the electrification

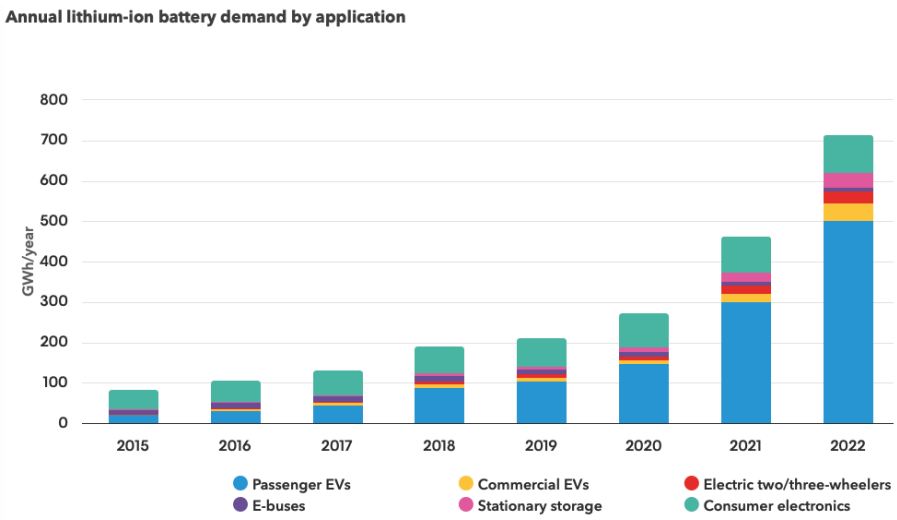


Figure 1.2: Global lithium-ion battery demand in 2022 was over 700 GWh/year, which is 8 times higher than in 2015. Figure from the 2023 BloombergNEF Electric Vehicle Outlook Report [14].

of transportation and in particular, passenger electric vehicles [9].

Despite the significant improvements since first commercialisation, the performance of lithium-ion batteries remains a bottleneck in the electrification of transport. Firstly, the gravimetric and volumetric energy density of lithium-ion batteries remains an order of magnitude or two lower than petrol (12 900 $\mathrm{W\,h\,kg^{-1}}$ and 9500 $\mathrm{W\,h\,L^{-1}}$, although arguably the mass of equipment required to deliver energy should be included in these figures for a fair comparison [15]). As such, electric vehicles today have lower range than their fossil fuel counterparts. Secondly, there is a limit to how fast batteries today can be charged [16]. Electric vehicles therefore take hours to fully charge compared to the minutes required to refill a tank with fossil fuels.

In light of the required improvements, national targets have been set for battery research and development. The US Vehicle Technologies Office aims to research new battery technologies that can increase range of electric vehicles to more than 300 miles, reduce the cell cost to less than 100 \$/kWh and decrease charge time to 15 minutes or less [17]. The UK Faraday Institution has similarly set targets relating to cell cost (50 \$/kWh), cell energy density (500 $\mathrm{W\,h\,kg^{-1}}$ and 1400 $\mathrm{W\,h\,L^{-1}}$), and pack power density (12 $\mathrm{kW\,kg^{-1}}$) [18]. Additional targets relating to safety, first life, operation temperature and recycling have also been set by the Faraday Institution.

In summary, cheaper batteries with higher energy and power density could accelerate our

transition away from fossil fuels. This thesis focuses on the design of battery electrodes for improved commercial cell performance.

1.2 Designing a better battery

All commercial battery electrodes today are manufactured by slurry-casting active material powder on to a metal current collector foil. This manufacturing process has been proven over decades and is embedded, but limits commercial cell performance. This thesis documents a quantitative, first-principles re-design of the battery electrode for improved gravimetric energy density at commercial cell level (Figure 1.3).

Chapter 2 provides an introduction to the design, manufacture and modelling of lithium-ion batteries today. Chapter 3 performs a quantitative assessment of a representative commercial lithium-ion cell. A theoretical cell is used as a reference to understand the source of losses and prioritise areas for research and development. Guided by the findings from the previous chapter, Chapter 4 identifies pyrolytic graphite sheet as a promising material for manufacture of a low inactive mass, low overpotential battery electrode. The introduction of electrolyte channels is demonstrated to improve the gravimetric active material capacity of pyrolytic graphite sheet by 40 times and could enable its use as a battery electrode. Chapter 5 highlights the limitations of gravimetric active material capacity as a metric for commercial cell design and develops a model to estimate commercial cell energy density from laboratory electrode characterisation data. Finally, Chapter 6 investigates the design of a practical pyrolytic graphite sheet electrode. The impact of design parameters on gravimetric active material capacity is investigated using physics-based modelling and contextualised using the model from Chapter 5. To conclude, the significance of the results in this thesis are discussed and opportunities for future work are identified in Chapter 7.

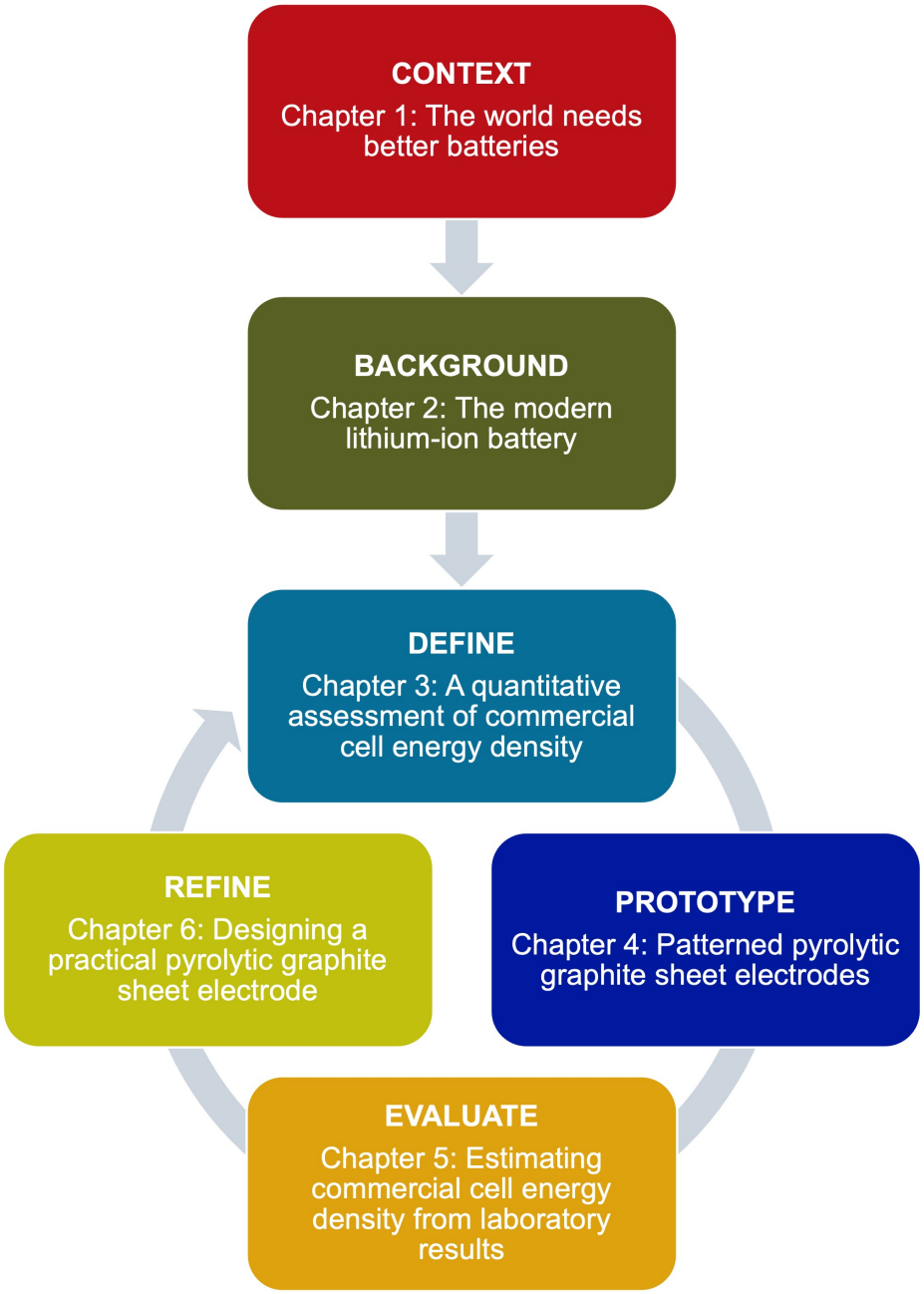


Figure 1.3: This thesis starts by establishing a need for better batteries (Chapter 1) and reviewing the design, manufacture and modelling of a modern lithium-ion battery (Chapter 2). Next, Chapter 3 performs a quantitative assessment of a representative commercial lithium-ion cell to prioritise areas for research and development. Guided by these findings, Chapter 4 demonstrates the introduction of electrolyte channels to improve the gravimetric active material capacity of pyrolytic graphite sheet by 40 times. Chapter 5 highlights the limitations of gravimetric active material capacity as a metric for commercial cell design and develops a model to estimate commercial cell energy density. Finally, Chapter 6 investigates the design of a practical pyrolytic graphite sheet electrode.

Chapter 2

The modern lithium-ion battery

The purpose of this chapter is to provide a qualitative overview of the design and manufacture of lithium-ion batteries today. It will commence by introducing the active materials and electrolyte. Next, it will examine the conventional methods used to incorporate these core materials into a commercial electrode, cell, module, or pack. Finally, this chapter will offer an introduction to the equations used to model batteries.

2.1 Battery fundamentals

What is a battery?

To begin with, let's define what a battery is. In the broadest sense, a battery refers to a device that stores and releases energy as needed. An electrical battery consists of one or more electrochemical cells, which are units designed to convert chemical energy into electrical energy (and potentially vice versa) [19]. Each electrochemical cell is comprised of three essential components: two electrodes and electrolyte.

In a charged battery, the electrodes will have differing chemical compositions, resulting in a potential difference between the electrodes. During the discharge or use of a battery, an electrochemical reaction occurs at each electrode. At the positive electrode, a reduction reaction takes place, where ions from the electrolyte and electrons from the external circuit combine. Simultaneously, at the negative electrode, an oxidation reaction occurs, releasing electrons into the external circuit and ions into the electrolyte. In the electrolyte, ions are able

to travel between the two electrodes. Meanwhile, the flow of electrons in the external circuit from the negative to the positive electrode represents an electric current that can power devices or systems.

In rechargeable batteries, the process can be reversed. When an external potential is applied to the battery during charging, the reactions at the electrodes are reversed. An oxidation reaction takes place at the positive electrode, releasing electrons back into the external circuit, while a reduction reaction takes place at the negative electrode, accepting electrons. A range of terms with specific definitions for batteries are used throughout this thesis and included in the Glossary.

A brief history of batteries

The history of batteries may date back over 2000 years. The earliest possible cells, known as Baghdad batteries, consisted of clay jars, filled with vinegar or lemon juice, that contained an iron rod and a copper cylinder [20]. While their exact purpose is still debated, it is believed they may have been used for electroplating or medical applications.

The next significant advance came in the late 18th century with the work of Luigi Galvani and Alessandro Volta. Galvani's experiments with frog muscles and metals led him to discover the concept of "animal electricity" [21]. Volta, inspired by Galvani's findings, developed the voltaic pile in 1800 [22, 23]. The voltaic pile consisted of alternating layers of zinc and copper discs separated by cloth soaked in saltwater.

The 19th century saw further progress in battery technology. John Frederic Daniell introduced the Daniell cell in 1836, which used a copper electrode in copper sulfate solution and a zinc electrode in sulphuric acid. This cell provided a voltage of 1.1 V and was used in early commercial telegraph systems [22]. In 1859, Gaston Planté invented the lead-acid battery [20], the first rechargeable battery, which later became widely used in automobiles. In 1866, Georges Leclanché invented the Leclanché cell, a zinc-carbon cell that used ammonium chloride as the electrolyte.

The first work on alkaline batteries was reported at the the start of the 20th century. Thomas Edison introduced the nickel-iron battery in 1901 and, around the same time, the

nickel-cadmium battery was invented by Waldemar Jungner. Both of these batteries gave a voltage of 1.2 V and were commercialised [22]. Nickel metal hydride batteries were later developed in 1989, offering three times the volumetric capacity.

In the 1970s, Stanley Whittingham developed the first functional lithium battery [24]. In 1980, John Goodenough doubled the battery's potential using lithium cobalt oxide as the cathode. In 1985, Akira Yoshino produced a safer battery by replacing lithium metal with petroleum coke. The lithium-ion battery was commercialised by Sony in 1991 and has since enabled the development of portable devices, electric vehicles, and renewable energy systems. The 2019 Nobel Prize in Chemistry was awarded to John Goodenough, Stanley Whittingham and Akira Yoshino for the development of lithium-ion batteries. The prize acknowledged their role in creating "the right conditions for a wireless and fossil fuel society" [24].

2.2 The modern lithium-ion battery

The modern lithium-ion battery works by storing lithium in different active materials at each electrode. In its charged state, lithium ions are primarily stored in the negative electrode of a lithium-ion battery. If an an external electrical circuit is provided between the two electrodes, the battery will discharge. During the discharge process, an oxidation reaction occurs at the negative electrode and lithium ions are released into the electrolyte. A corresponding reduction reaction occurs at the positive electrode triggering lithium ions to enter the positive electrode from the electrolyte. Electrons released during the oxidation reaction travel through an external circuit to the other electrode to participate in the reduction reaction. Discharge will normally be terminated (by breaking the external electrical circuit) when the potential difference between the two electrodes falls below a specified value. In its discharged state, lithium ions are primarily stored in the positive electrode. To charge the battery, a potential difference will be applied between the two electrodes such that an oxidation reaction occurs at the positive electrode (lithium ions enter the electrolyte) and a reduction reaction occurs at the negative electrode (lithium ions enter the negative electrode). During charging, electrons will travel from the positive electrode to the negative electrode.

Besides the reversible redox reactions, irreversible reactions can also occur if they are ener-

getically favourable at the electrode potentials present in the cell. The electrode potentials are an indirect measure of the electron energy levels [25, 26]. If the energy level of the electrons in the positive electrode is lower than the highest occupied molecular orbital of a species in solution, an electron will transfer from chemical species to the electrode. Alternatively, if the electron energy level in the negative electrode is higher than the lowest vacant molecular orbital of a chemical species, the chemical species will be reduced. As these electron transfers occur, products of the chemical reactions can accumulate on the electrode surface to form a layer. Upon reaching a critical thickness, the potential drop across this layer may become sufficient to prevent further reaction. This passivation layer is referred to as the solid electrolyte interphase, or SEI [27].

The sections that follow will examine the materials and manufacturing methods used for commercial lithium-ion cells.

2.2.1 Active materials

A range of active materials are used for both the positive and negative electrodes in a lithium-ion battery. Figure 2.1 shows the average discharge potential vs. Li/Li^+ for typical lithium-ion battery active materials plotted as a function of gravimetric active material capacity. To maximise gravimetric energy density, both negative and positive active materials should have high gravimetric capacities. The potential difference between the active materials should also be maximised, so high potential positive active materials and low potential negative electrode materials are favourable.

Positive active materials

Lithium cobalt oxide (LCO) was used in the first commercial lithium-ion battery released by Sony in 1991 [11, 24]. It possesses a layered crystal structure that facilitates lithium intercalation and deintercalation during discharge and charge cycles. LCO offers reasonable gravimetric capacity and good cycle life. However, cobalt is expensive, and there are concerns regarding its limited abundance and ethical sourcing [29, 30].

The lithium nickel manganese cobalt oxide (NMC) family of positive electrode materials

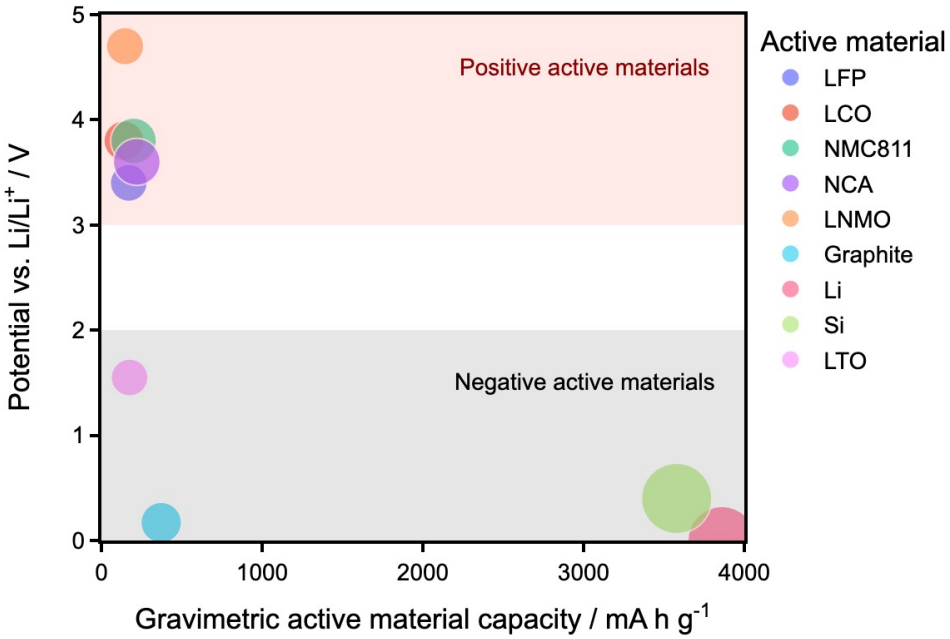


Figure 2.1: The average discharge potential vs. Li/Li^+ for typical lithium-ion battery active materials plotted as a function of gravimetric active material capacity. The diameters of the bubbles indicate the relative volumetric active material capacities. Data from [28] was used to populate this figure.

emerged as a promising alternative to LCO. NMC positive electrodes offer higher energy density and reasonable cycle life for a lower raw materials cost [29]. There has been a trend towards nickel-rich materials such as NMC811 which contain less cobalt and offer higher gravimetric capacity [31, 28]. NMC materials are widely used in electric vehicles due to their high gravimetric capacity and high discharge potential.

Besides NMC, spinel lithium manganese oxide (LMO) offers good thermal stability but suffers from capacity fading. Regardless, it is still used in many electric vehicle batteries due to high rate capability and low cost [31]. Nickel can be added to form spinel lithium nickel manganese oxide (LNMO) which has a higher average discharge potential. However, the high discharge potential, although beneficial for cell energy density, results in irreversible side reactions in most electrolytes which limits cycle life [28]. Lithium nickel cobalt aluminum oxide (NCA) is another alternative to NMC that provides a good balance of gravimetric capacity and power, discharge potential and cycle life. Compared to NMC, NCA offers improved capacity retention and power, but less thermal stability [31].

Although LFP has a comparatively low gravimetric capacity and average discharge voltage,

it has gained significant recent attention due to its low cost, reduced dependency on critical minerals, and excellent safety characteristics [28]. This recent attention is in part in due to innovations in cell design. Although LFP cells have lower energy density, they can offer improved pack-level packing efficiency as they are larger cells (300-1000 W h) and have less stringent thermal management requirements [29]. The pack-level energy density of LFP cells is therefore competitive with packs composed of more energy dense NMC cells.

Negative active materials

Intercalation materials are widely used as the negative active material, with natural and artificial graphites being the most common. Graphite offers both reasonable gravimetric capacity ($372\,\mathrm{mA\,h\,g^{-1}}$) and good cycle life due to the formation of a stable solid electrolyte interphase and limited volume expansion (roughly 10%) during intercalation. Natural graphite is more cost-effective and offers slightly higher gravimetric capacity, whereas artificial graphite enables a longer cycle life [31, 29].

Lithium-titanium-oxide (LTO) is another intercalation material with a lower gravimetric capacity ($172\,\mathrm{mA\,h\,g^{-1}}$) and higher delithiation potential but exceptional thermal stability, high rate capability, and long cycle life [31]. The high delithiation potential of LTO limits cell energy density but lies within the electrochemical stability window of many liquid electrolytes and limits the risk of lithium plating [29].

Alloying-type materials, such as silicon and silicon-oxides, have gained attention for their high gravimetric capacity. However, they suffer from significant volume changes (up to 300%) during lithiation and delithiation that limit cycle life [28, 31]. Silicon and silicon-oxides are often combined with graphite to form an electrode with enhanced gravimetric capacity while minimising the adverse effects of volume expansion. At the moment, the silicon oxide content of graphite-based electrodes is estimated as 2-10%, but higher silicon content battery packs are under development [29].

Lithium metal can be used directly as the negative active material and offers the highest possible gravimetric capacity and lowest delithiation potential. However, there are practical issues related to reactivity, dendrite formation and volume change that hinder safety and cycle

life [31, 28, 29, 32].

2.2.2 Electrolyte

In an electrochemical cell the two electrodes are immersed in electrolyte. The electrolyte must facilitate the transfer of lithium ions between the two electrodes and maintain stability when exposed to low potentials on the negative electrode and high potentials on the positive electrode.

The electrolyte is constantly exposed to reduction on the negative electrode due to exposure to potentials outside of its stability window. Fortunately, a passivation layer called the solid electrolyte interphase (SEI) tends to form on the negative electrode surface [25, 29]. The SEI is composed of the decomposition products from electrolyte reduction and primarily forms during the first charge of a lithium-ion battery. On the positive electrode, the electrolyte is exposed to high potentials and oxidation, which can also lead to the formation of a passivation layer [28]. Both passivation layers should allow the transport of lithium ions while blocking electron transport to prevent further electrolyte degradation.

Typically, a liquid electrolyte is used, consisting of a salt dissolved in a solvent. For lithium-ion batteries, a few lithium salts have been examined, with the most common being $LiPF_6$, used in combination with a nonaqueous organic solvent [31]. The ideal solvent will dissolve the lithium salt effectively to form a solution with high ionic conductivity, high dielectric constant, good thermal stability, low viscosity, low reactivity with other components, and be non-toxic and cost-effective [29]. Often, a combination of different solvents is used to meet specific cell requirements. Established electrolyte solvents include ethylene carbonate (EC), ethyl methyl carbonate (EMC), diethyl carbonate (DEC) and dimethyl carbonate (DMC) [31]. Various electrolyte additives are also used to improve the stability of the passivation layers, enhance ionic conductivity, and improve thermal stability [28].

In addition to liquid electrolytes, other electrolyte technologies have been explored, including solid polymer and gel polymer electrolytes, ionic liquids, and solid electrolytes [33]. However, these alternative electrolyte systems face challenges such as achieving adequate ionic conductivity at room temperature, ensuring mechanical stability, forming a stable SEI, and establishing a stable contact at the electrode interfaces [31]. Consequently, liquid electrolyte

systems remain the preferred choice for current lithium-ion battery technology.

2.2.3 Commercial electrodes

Commercial electrodes are manufactured by casting a slurry of active material on to a metal current collector foil. This process has been used since the first commercialisation of lithium-ion batteries by Sony in 1991 [33]. Slurry casting enables micro-scale active material particles to be assembled into a macro-scale battery electrode. A binder is typically used to hold the active material particles together and a conductive additive may be added to improve electrical conductivity of the slurry. The slurry is cast on to a metal current collector foil that provides both mechanical stability and a low electrical resistance path to the external electrical circuit.

Binder

Polyvinylidene fluoride (PVDF) is often used as binder for the positive electrode [33, 28]. In this case, N-Methyl-2-pyrrolidone (NMP) is typically used as a solvent when preparing the slurry. Negative electrodes were conventionally manufactured in the same way, however have recently transferred from using NMP to water as the solvent. Water based slurries normally use a mixture of styrene-butadiene rubber (SBR) and carboxymethyl cellulose (CMC) [34].

Conductive additive

Carbon black or acetylene black is often added as a conductive additive to both the negative and positive electrode slurries to improve electrical and thermal conductivity [34]. These carbonaceous additives may be electrochemically active in the negative electrode and contribute a small amount of both reversible and irreversible lithium ion capacity [28].

Current collector

The slurry is cast on to a metal current collector for mechanical support and to provide a high thermal and electrical conductivity path. Aluminium is lightweight (density, $2.70\,\mathrm{g\,cm^{-3}}$ [35]) and has high electrical ($37 \times 10^6\,\mathrm{S\,m^{-1}}$ [36]) and thermal ($210\,\mathrm{W\,m^{-1}\,K^{-1}}$ [36]) conductivity. These attributes make aluminium a good choice for the positive electrode, however aluminum

is not electrochemically stable at the lower potentials of the negative electrode so copper is used instead [37]. Copper is stable at lower potentials and has higher electrical ($60 \times 10^6\,\mathrm{S\,m^{-1}}$ [38]) and thermal ($385\,\mathrm{W\,m^{-1}\,K^{-1}}$ [38]) conductivity than aluminium but is 3 times more dense ($8.96\,\mathrm{g\,cm^{-3}}$ [35]). Higher electrical conductivity permits copper current collectors to be thinner, but the mass of copper current collectors is still greater than aluminium current collectors due to the high density of copper [39]. Copper is also more expensive than aluminium so the negative current collector makes up a greater contribution of cell cost. The current collector is coated on both sides in commercial electrodes to minimise the current collector mass, volume, and cost within the cell.

2.2.4 Commercial cells

Separator

In a commercial cell that uses liquid electrolyte, a separator is required to prevent physical contact between the closely-spaced electrodes. The separator must allow the passage of ions but not electrons between the electrodes. A porous membrane, typically made from a polymer with low electronic conductivity such as polypropylene or polyethylene, is used in commercial lithium-ion batteries.

Besides preventing short-circuits, a multi-layer separator may also be designed to safely shut down a cell in case of thermal runaway [40]. Polymers with differing melting points, such as polyethylene and polypropylene, are typically used for the individual layers. In the case of rising cell temperature, polyethylene will melt at temperatures above 120 °C, blocking any pores and inhibiting ion transport. Meanwhile, polypropylene has a higher melting point (160 °C) and will maintain its mechanical integrity to prevent physical contact between the electrodes. Ceramic coatings are also used for commercial separators to improve thermal resistance and reduce shrinkage [41].

Electrode stacks, jelly rolls and cell casings

The electrodes and separators will be stacked and then put inside a cell casing. Three main formats of cell casing are used commercially: cylindrical, pouch and prismatic [34]. The elec-

trode stack will be wound to form a "jelly roll" in the case of cylindrical cells. For pouch and prismatic cells the electrodes will be stacked or flat wound. Cylindrical and pouch cells use a hard case made of aluminium alloy or stainless steel, whereas a pouch cell will typically use a metallised polymer film. For each format, a range of casing dimensions are used. Larger cells enable improved cell-level energy and power density, and can reduce manufacturing costs, but may lead to inhomogeneities in current distribution and temperature.

Modules and packs

For high energy and power applications such as electric vehicles, the individual cells will be connected in series or parallel and incorporated into modules and packs [34]. Additional inactive components (e.g. housing, connections, safety devices, sensors, thermal management) will be added to create the modules and packs. The mass and volume of these inactive components reduces energy and power density at pack level by a factor of 2 compared to cell-level [29]. An electric vehicle pack will have a voltage of between 200 and 800 V and an energy of between 10 and 100 kW h. Pack voltage and energy will influence the power and range of the electric vehicle.

For safe operation and good performance at pack level, an active thermal management system is required to regulate the temperature of cells during charge and discharge [42]. If cell temperature is low, internal resistance will be higher and reaction kinetics will be slower. These factors will increase overpotentials and increase the risk of lithium plating on the negative electrode during fast charging. Conversely at high temperatures, reaction and transport kinetics will be higher which is good during operation (reduced overpotentials), but also increases the rate of parasitic side reactions responsible for cell degradation. Different thermal management strategies exist and include free or forced convective cooling using heat transfer fluids, tab cooling, base plate cooling, and use of phase change materials [42].

2.3 Battery modelling fundamentals

Many researchers and companies are working to improve the design of batteries, with the aim of increasing attributes such as energy density, power density, temperature regulation

and longevity. While experimental approaches to battery design improvement are essential, predictive models can greatly accelerate testing and provide valuable insights into experimental measurements. Various approaches to battery modelling have been developed across different length scales, from atoms to electric vehicle packs [43].

A battery model attempts to simulate cell performance using mathematical equations. The simplest battery models are empirical and will fit a number of equations and parameters to represent the observed cell performance. The simplicity of empirical models makes them fast to run and easier to build, however, the equations in an empirical model are not based on the underlying physics and are only valid for the parametrised data. In comparison, physics-based models use mathematical equations to explicitly represent the physical processes inside a cell. These models are more computationally intensive, but offer greater insight into the underlying physics and permit some level of cautious extrapolation beyond the parametrised data.

For physics-based modelling, three key domains can be identified in a lithium-ion battery: positive active material, negative active material, and electrolyte. The mathematical equations of a battery model that represent the conservation of mass and current across these three domains are recently reviewed [43, 44, 45] and will be introduced in the following sections. The equations are largely adapted from the recent review by Planella *et al.* [43].

2.3.1 Conservation and transport of mass

Active material

Within the negative, n, and positive, p, active material domains, k, the mass of lithium is conserved ($k \in \{\mathrm{n}, \mathrm{p}\}$):

$$\frac{\partial c_k}{\partial t} + \nabla \cdot \mathbf{N}_k = 0 \tag{2.1}$$

where $\mathbf{N}_k$ is the lithium ion flux and c_k is the lithium ion concentration. This flux can be specified in terms of the gradients in lithium ion concentration, c_k:

$$\mathbf{N}_k = -D_k(c_k)\nabla c_k \tag{2.2}$$

where D_k is the lithium ion diffusivity within the active material, which may itself be a function of lithium ion concentration, c_k. Although it has limitations [43], Fick's law is typically used to describe lithium ion transport in the active material.

Interface

At the interface, lithium ions may be exchanged between active material and electrolyte in an electrochemical reaction. To represent this exchange, a boundary condition can be imposed at the interface between active material and electrolyte:

$$F\mathbf{N}_k \cdot \mathbf{n}_k = \mathbf{i}_k \cdot \mathbf{n}_k = j_k \tag{2.3}$$

where j_k is the reaction current density at the interface, $\mathbf{i}_k$ is the current density, $\mathbf{n}_k$ is the unit normal vector pointing outwards from the active material at the interface and F is the Faraday constant. It is implied in this equation that all of the current flowing into the active material is carried by the lithium ion flux, $\mathbf{N}_k$.

The reaction current density, j_k, can be described by the concentration-dependent Butler-Volmer equation [46]. The overpotential, $\eta_{k,\mathrm{ref}}$, is defined with respect to a fixed reference state for the activities of the oxidised and reduced species of the redox couple ($c_{R,\mathrm{ref}}$ and $c_{O,\mathrm{ref}}$):

$$j_k = j_{k0,\mathrm{ref}} \left[\frac{c_R}{c_{R,\mathrm{ref}}} \exp(\frac{\alpha_a F \eta_{k,\mathrm{ref}}}{RT}) - \frac{c_O}{c_{O,\mathrm{ref}}} \exp(-\frac{\alpha_c F \eta_{k,\mathrm{ref}}}{RT}) \right] \tag{2.4}$$

where

$$j_{k0,\mathrm{ref}} = j_{k0,0} c_{R,\mathrm{ref}}^{\alpha_c/n} c_{O,\mathrm{ref}}^{\alpha_a/n} \tag{2.5}$$

and

$$\eta_{k,\mathrm{ref}} = E - E_{\mathrm{eq,\ ref}} \tag{2.6}$$

with

$$E_{\text{eq, ref}} = E_{\text{eq, 0}} - \frac{RT}{nF} \ln \frac{c_{R,\text{ref}}}{c_{O,\text{ref}}} \tag{2.7}$$

In this set of equations, R is the universal gas constant, T is the temperature, α_a is the anodic transfer coefficient, α_c is the cathodic transfer coefficient, n is the number of electrons in the charge transfer reaction, E is the potential, and E_{eq} is the equilibrium potential.

Electrolyte

If a binary electrolyte is considered then charge neutrality dictates that the concentration of positive lithium ions, $c_{\text{e}+}$, must be equal to the concentration of negative counter ions, $c_{\text{e}-}$. The concentration of ions in the electrolyte can therefore be represented simply as c_{e}.

Conservation of positive lithium ions and negative counter ions in the electrolyte can be represented as follows:

$$\frac{\partial c_{\text{e}}}{\partial t} + \nabla \cdot \mathbf{N}_{\text{e}+} = 0 \tag{2.8}$$

$$\frac{\partial c_{\text{e}}}{\partial t} + \nabla \cdot \mathbf{N}_{\text{e}-} = 0 \tag{2.9}$$

Equations for the lithium ion flux, $\mathbf{N}_{\text{e}+}$, and counter ion flux, $\mathbf{N}_{\text{e}-}$, can be derived from the Maxwell-Stefan equations (please see [43] for full derivation):

$$\mathbf{N}_{\text{e}+} = -D_{\text{e}}(c_{\text{e}})\nabla c_{\text{e}} + \frac{t^+(c_{\text{e}})}{F}\mathbf{i}_{\text{e}} \tag{2.10}$$

$$\mathbf{N}_{\text{e}-} = -D_{\text{e}}(c_{\text{e}})\nabla c_{\text{e}} - \frac{1 - t^+(c_{\text{e}})}{F}\mathbf{i}_{\text{e}} \tag{2.11}$$

Both the transference number, t^+, and the ion diffusivity, D_{e}, are a function of ion concentration, c_{e}. The positive transference number represents the fraction of current carried by positive ions. Note it is only necessary to consider either lithium ion flux or the counter ion flux (not both) to arrive at a closed model.

The use of the Maxwell-Stefan equations is typically referred to as "concentrated electrolyte

theory" and considered best practice for the moderate electrolyte ion concentrations used in commercial cells. Regardless, some models will use "dilute electrolyte theory", based on the Nernst-Planck equations instead.

2.3.2 Conservation and transport of charge

Active material

Charge is conserved within the active material:

$$\nabla \cdot \mathbf{i}_k = 0 \tag{2.12}$$

and the current density, $\mathbf{i}_k$, can be specified in terms of the gradients in the electrical potential, ϕ_k, that exist within the active material:

$$\mathbf{i}_k = -\sigma_k \nabla \phi_k \tag{2.13}$$

where σ_k is the electronic conductivity of the active material.

Interface

The boundary condition is:

$$F\mathbf{N}_\mathrm{e} \cdot \mathbf{n}_k = \mathbf{i}_\mathrm{e} \cdot \mathbf{n}_k = -j_k \tag{2.14}$$

where j_k is the reaction current density at the interface, $\mathbf{i}_\mathrm{e}$ is the current density, $\mathbf{n}_k$ is the unit normal vector pointing outwards from the active material at the interface and F is the Faraday constant. It is implied in this equation that all of the current flowing into the active material is carried by the ion flux, $\mathbf{N}_\mathrm{e}$. Note that this coupling is a repeat of equation 2.3.

Electrolyte

Conservation of charge in the electrolyte can be similarly expressed:

$$\nabla \cdot \mathbf{i}_\mathrm{e} = 0 \tag{2.15}$$

with an expression for the current density, $\mathbf{i}_\mathrm{e}$, in terms of ion concentration, c_e, and electric potential, ϕ_e again obtained from the Maxwell-Stefan equations:

$$\mathbf{i}_\mathrm{e} = -\sigma_\mathrm{e}(\nabla\phi_\mathrm{e} - \frac{2}{F}(1-t^+)\frac{\mathrm{d}\mu_\mathrm{e}}{\mathrm{d}c_\mathrm{e}}\nabla c_\mathrm{e}) \tag{2.16}$$

2.3.3 Closing the model

The active material domain will typically interface a current collector. At this boundary there may be a flux of electrons, but not lithium ions. There is no flux of lithium ions or electrons at the remaining outer boundaries of the active material and electrolyte domains.

A potential difference can be prescribed between the two current collectors, with the reference potential normally in the negative current collector. This potential difference can be controlled to achieve a desired applied current.

Finally, initial concentrations of lithium in each domain are assumed:

$$c_k = c_{k0}, \quad c_\mathrm{e} = c_{\mathrm{e}0}, \quad \text{at } t = 0 \tag{2.17}$$

2.3.4 Modelling in practice

To simulate the performance of a conventional commercial cell, a number of extensions to the above framework must be added [43].

Firstly, commercial electrodes typically have a complex microstructure. This microstructure contains additional materials besides the active materials, such as binder and conductivity. These inactive materials should be included as additional domains and will reduce the interface between active material and electrolyte. An accurate representation of the electrode microstructure is also required and the domains must be labelled. A decision must be made on the resolution at which the microstructure is represented for modelling. For instance, nano-scale features such as particle roughness and cracks could be represented, but it would be computationally expensive. In general, the lowest resolution that permits accurate simulation of cell performance is a good target.

Rather than using a heterogeneous, microstructure-resolved model, it is more common to

use a homogenised model for particle based commercial electrodes. Homogenised models reduce computational expense by representing the electrode microstructure as a much simpler homogeneous geometry. The equations are modified to use average fluxes, effective transport parameters and source terms (instead of capturing the interface between active material and electrolyte explicitly). Although these models are homogenised, a micro-scale particle domain is typically retained to explicitly model lithium ion transport in the active material. Homogenised models are widely reviewed for the interested reader [43, 44, 45], but the detailed background is not required for this thesis.

Chapter 3

A quantitative assessment of commercial cell energy density

Commercial cells are complex systems that span multiple length scales [47]. A cylindrical commercial cell will typically be 5-10 cm tall, but contain particles smaller than 1 µm, each with its own nano-scale features (Figure 3.1). Due to this complexity, it is not trivial to trace cell-level performance losses back to individual components.

To prioritise research and development work, this chapter will conduct a quantitative analysis of an existing commercial cell to reveal the key sources of performance loss. The analysis will be conducted in four key steps. A baseline for existing commercial battery performance will first be established and, in doing so, a representative cell will be selected for more detailed analysis. Next, the theoretical performance of the representative cell will be calculated and compared with the measured performance to identify losses. Parameterised cell data will then be used to investigate the losses in more detail to understand their origin. Finally, the most promising areas on which to focus research and development will be identified and prioritised.

3.1 Establishing baseline gravimetric energy density

There are a large number of commercial cells available today, however regrettably there is a lack of high quality open-source data on the performance of these cells. Where open-source data is available, the test methods are often not standardised and the reported information can

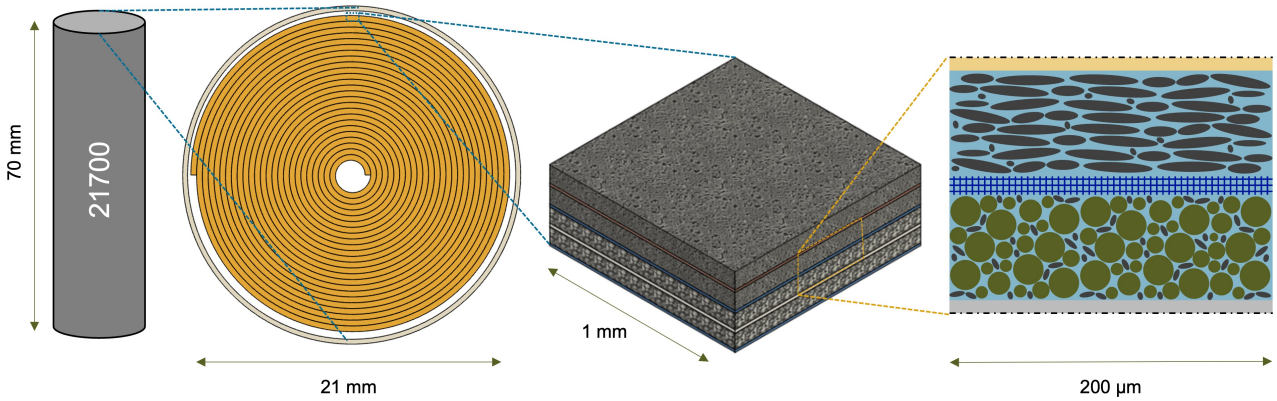


Figure 3.1: Commercial cells are complex systems that span multiple length scales. A cylindrical cell will typically be 5-10 cm tall, but contain particles smaller than 1 µm. The particles themselves will also have nano-scale features. Due to this complexity, it is not trivial to trace cell-level performance losses back to individual components.

be inconsistent across manufacturers and research groups. This gap is widely recognised [29, 48], and several companies are now building and licensing access to databases of commercial cell performance [3, 49]. Fortunately, one such company, Batemo [3], has made some of its data available publicly and this data set provides a good starting point for a quantitative overview of the commercial battery landscape.

The publicly available Batemo data set includes 161 commercial cells. For each cell, Batemo has conducted independent measurements of mass, volume, capacity, current, energy and power to allow cell-level metrics such as energy and power density to be calculated. There are a variety of metrics by which performance of a lithium-ion cell can be assessed, as summarised in the Glossary, and the relevance of each will depend on the application. Gravimetric cell energy density is a key metric for determining how much energy can be stored for a given pack mass and strongly influences range of electric vehicles. As discussed in the introduction, electrification of transport is critical for a transition away from fossil fuels. This thesis will use gravimetric cell energy density as the key metric to assess performance losses and to optimise cell design.

Figure 3.2A shows the gravimetric energy density of the 161 commercial cells in the data set plotted as a function of the peak gravimetric power density. Energy in this case was measured by discharging cells from 100% state of charge under a constant current of 0.1C until a voltage of 2.5 V was reached. Peak power is the maximum power that the cell was capable of delivering for 5 minutes and measured by gradually increasing discharge current until either a voltage of

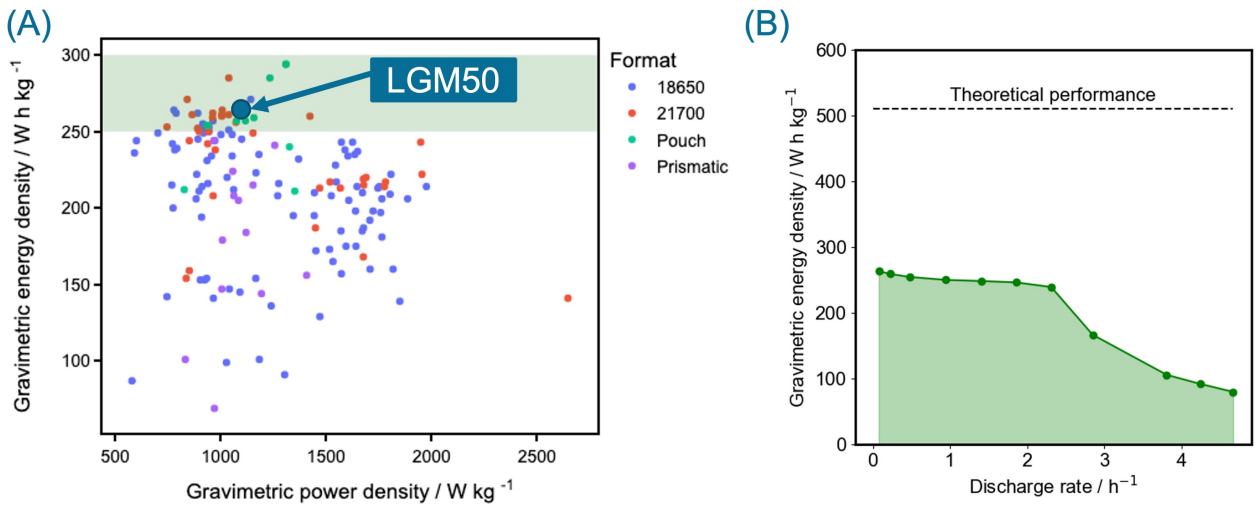


Figure 3.2: (A) Gravimetric energy density of the 161 commercial cells in the Batemo data set [3] plotted as a function of gravimetric power density. State-of-the-art commercial cells have a gravimetric energy density of 250-300 W h kg^{-1} (indicated by green shading). The data point representing the LGM50 cell is highlighted. (B) Gravimetric energy density plotted as a function of discharge rate for the LGM50 cell. At elevated discharge rates, gravimetric energy density falls to less than 30% of the value measured at a discharge rate of 0.1C.

2.5 V or surface temperature of 70 °C was reached after 5 minutes of constant current discharge from 100% state of charge. The energy and peak power were divided by the mass of the cell to obtain the gravimetric energy density and the gravimetric power density.

There are two key takeaways from Figure 3.2A. Firstly, state-of-the-art commercial cells have a gravimetric energy density of 250-300 W h kg^{-1}, as indicated by the green region. This number is a crucial reference point for many of the discussions in this thesis. Secondly, for a given cell format, cells with a higher gravimetric power density tend to have a lower gravimetric energy density. This trend is expected given that cells are typically designed for high-power or high-energy applications, and the architecture of existing commercial cells necessitates a compromise between these two metrics [50]. It is also worth highlighting that the gravimetric energy density data in Figure 3.2A are measured at a discharge rate of 0.1C. Gravimetric energy density is highly dependent on the discharge rate, particularly for high-energy cells which tend to have thicker, more tortuous electrodes.

The data point in Figure 3.2A representing the LGM50 cell is highlighted. This cell is within the 250-300 W h kg^{-1} gravimetric energy density range for state-of-the-art cells, is widely used and is one of the few that have been parametrised in the academic literature [51]. For these

reasons, the LGM50 cell was selected as a representative commercial cell for more detailed analysis in this chapter. Figure 3.2B shows the gravimetric energy density plotted as a function of discharge rate for the LGM50 cell. At elevated discharge rates, gravimetric energy density falls to less than 30% of the value measured at a discharge rate of 0.1C.

3.2 Identifying the losses

The previous section established that state-of-the-art commercial cells have a gravimetric energy density of 250-300 $\mathrm{W\,h\,kg^{-1}}$ (measured at a discharge rate of 0.1C) and the LGM50 cell was selected as a representative commercial cell. However, although the relative performance of different commercial cells can be compared using Figure 3.2, it does not show how well these cells perform compared to their theoretical performance.

Today, commercial cells are complex and contain many components (Figure 3.3). In addition to active material, a typical commercial cell will contain binder, conductive additive, metal current collectors, polymer separators, electrolyte, and a metal casing (complete with its own sub-components). All of these inactive components contribute mass and volume, but not capacity, to the cell. Additionally, for various reasons that will be discussed later, the active material that is present might not be fully lithiated or delithiated during charge and discharge. Given the complexity of commercial cells, to perform a more absolute evaluation of commercial cell performance, we will imagine a theoretical cell (Figure 3.3). This theoretical cell will be composed solely of active material, and we will calculate its gravimetric energy density for comparison to the measured LGM50 performance.

The gravimetric energy density of our theoretical cell depends on the cell chemistry. There are a range of cell chemistries on the market and under development, but we will focus on the graphite-SiO_x/NMC811 chemistry that is used in the LGM50 cell. The positive active material of the LGM50 cell is NMC811 and the negative active material is a composite of graphite (90% mass) and SiO_x (10% mass) [51].

The theoretical gravimetric energy density of an active material pairing depends on the potential difference between the positive and negative active material, and their respective gravimetric capacities:

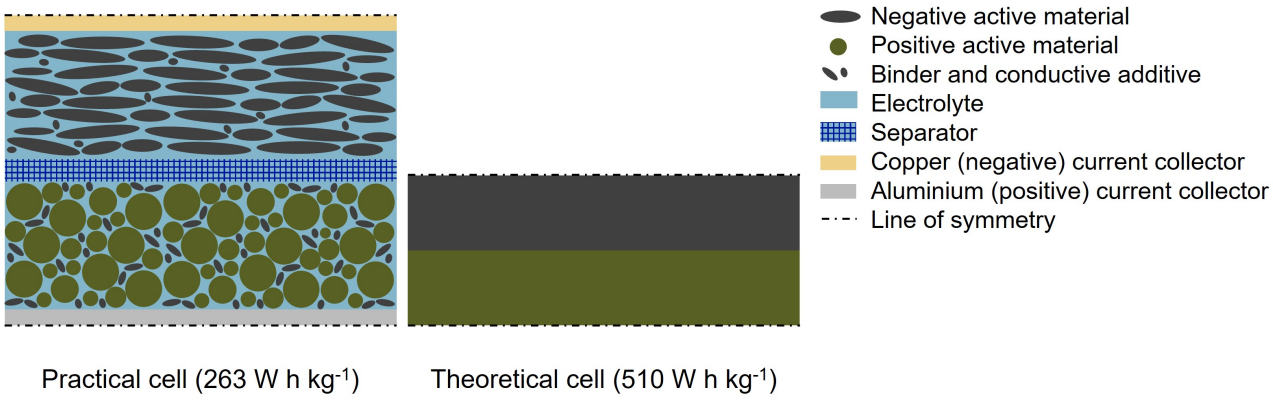


Figure 3.3: Schematic showing a practical and theoretical LGM50 cell cross-section. The dashed lines represent lines of symmetry through the double-sided electrodes. The quoted gravimetric energy densities are as measured for the practical LGM50 cell and calculated for the theoretical cell, assuming a negligible mass for all inactive components (including the electrolyte and casing).

$$\text{Theoretical gravimetric energy density} = \frac{V_{\text{PAM}} - V_{\text{NAM}}}{\frac{1}{\text{Q}_{\text{PAM}}} + \frac{1}{\text{Q}_{\text{NAM}}}} \tag{3.1}$$

where V_{PAM} and V_{NAM} represent the potential against Li/Li^+ of the positive active material and negative active material, and Q_{PAM} and Q_{NAM} represent the gravimetric capacity of the positive and negative active materials.

As shown in equation 3.2, we can calculate the mass of each of the active materials that would be required to deliver 1 mA h and in doing so, calculate the gravimetric capacity of this active material pairing as $140\,\text{mA h g}^{-1}$:

$$\text{Theoretical gravimetric capacity} = \frac{1}{\frac{1}{221} + \frac{1}{386}} = 140\,\text{mA h g}^{-1} \tag{3.2}$$

where the gravimetric active material capacity of the graphite-SiO_x and NMC811 have respective assumed values of $386\,\text{mA h g}^{-1}$ and $221\,\text{mA h g}^{-1}$ [51].

The theoretical gravimetric energy density is subsequently calculated as $510\,\text{W h kg}^{-1}$ by assuming a mean, low-rate discharge voltage of 3.63 V:

$$\text{Theoretical gravimetric energy density} = 140\,\text{mA h g}^{-1} \times 3.63\,\text{V} = 510\,\text{W h kg}^{-1} \tag{3.3}$$

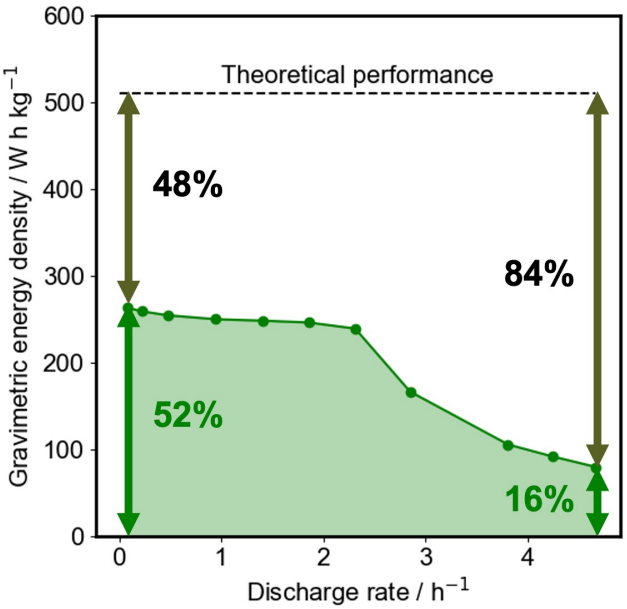


Figure 3.4: Gravimetric energy density of the practical and theoretical LGM50 cell compared. At low discharge rates, the LGM50 cell achieves only 52% of the theoretical gravimetric energy density for its chemistry. At elevated discharge rates, gravimetric energy density falls to less than 20% of the theoretical value.

Using this theoretical gravimetric energy density, several observations can be made about the LGM50 cell, as shown in Figure 3.4. Firstly, at low discharge rates, the LGM50 cell achieves only 52% of the theoretical gravimetric energy density for its chemistry. This number indicates that it is theoretically possible, but not necessarily practical, to double the low discharge rate gravimetric energy density of the LGM50 cell without changing the chemistry. Secondly, gravimetric energy density falls to less than 20% of the theoretical value at a discharge rate of 4C, indicating that there is potential to improve gravimetric energy density at elevated discharge rates by five times.

3.3 Understanding the losses

The previous section identified that it is theoretically possible to improve the gravimetric energy density of the LGM50 cell by two to five times. However, we cannot yet conclude how much of this improvement could realistically be captured. To evaluate the feasibility of making these improvements, we will now break down the losses to understand them in more detail.

The LGM50 gravimetric energy density measured at a given discharge rate depends on

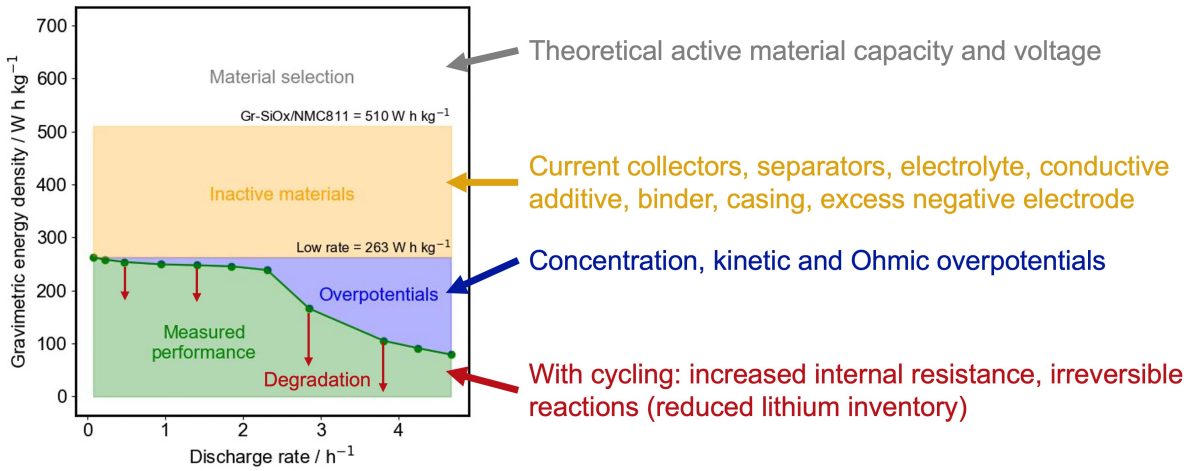


Figure 3.5: The LGM50 gravimetric energy density measured at a given discharge rate depends on active material selection, inactive materials and overpotentials. The theoretical gravimetric energy density of an active material pairing is determined by the gravimetric capacities of the active materials and the difference in their potentials. At low discharge rates, overpotentials will be minimised and the difference between the theoretical and measured performance will primarily be due to inactive materials. Overpotentials will increase with discharge rate and reduce the measured gravimetric energy density.

active material selection, inactive materials and overpotentials (Figure 3.5). The theoretical gravimetric energy density of an active material pairing is determined by the gravimetric capacities of the active materials and the difference in their potentials. At low discharge rates, overpotentials will be minimised and the difference between the theoretical and measured performance will primarily be due to inactive materials. Overpotentials will increase with discharge rate and reduce the measured gravimetric energy density.

3.3.1 Inactive materials

We will first consider the losses that are observed at low discharge rates. At low discharge rates, overpotentials are minimised and we can therefore assume full lithiation and delithiation of the active materials. If this assumption holds, then the theoretical capacity and potential of the active materials present in the cell will be measured. The gap between measured and theoretical gravimetric energy density in this case therefore results from the cell mass, and more specifically, the inactive materials.

Using the parametrisation data for the LGM50 cell (summarised in Table 3.1), we can break down the loss due to inactive materials further. Figure 3.6 shows the thickness, density and

Table 3.1: Summary of parametrisation data for LGM50 cell [51]. It was assumed that both electrode slurries had a mass-basis composition of 95% active material, 2.5% binder and 2.5% conductive additive. The separator was also measured to have a thickness of 12 µm and porosity of 47%.

Parameter	Positive electrode	Negative electrode
Geometry		
Length / cm	79.0	80.5
Width / cm	6.50	6.50
Current collector thickness / µm	16.3	11.7
Slurry thickness / µm	75.6	85.2
Active material loading / $g\,m^{-2}$	246.9	148.5
Average particle diameter / µm	10.4	11.7
Electrolyte volume fraction (porosity) / %	33.5	25.0
Materials		
Active material composition	NMC811	Graphite-SiO_x
Active material density / $g\,cm^{-3}$	4.95	2.26
Binder density / $g\,cm^{-3}$	2.00	2.00
Conductive additive density / $g\,cm^{-3}$	2.00	2.00
Current collector material	Aluminium	Copper
Current collector density / $g\,cm^{-3}$	2.70	8.96
Electrolyte density / $g\,cm^{-3}$	1.20	1.20

porosity of each of the LGM50 cell components. Using these values, we can calculate a volume loading ($m^3\,m^{-2}$, or simply m) and mass loading ($g\,m^{-2}$) for the solid and electrolyte within each component in the jelly roll. The result of these calculations shows that the LGM50 jelly roll has a thickness of 374 µm and total (solid and electrolyte) mass loading of $1050\,g\,m^{-2}$.

The area of the LGM50 jelly roll has also been measured ($518\,cm^2$), so we can calculate the mass of each component in the final cell, including the casing. The excess volume inside the cell (not filled by the jelly roll) was calculated by comparing the measured jelly roll volume

COMPONENT	Stack order	Thickness	Solid density*	Porosity	Solid thickness / um	Electrolyte thickness / um	Solid mass loading / g m-2	Electrolyte mass loading / g m-2
Negative electrode	1	85.2	2.28	24.9%	64.0	21.2	146.1	27.2
Negative current collector	2	11.7	8.96	0.0%	11.7	0.0	104.8	0.0
Negative electrode	3	85.2	2.28	24.9%	64.0	21.2	146.1	27.2
Separator	4	12.0	0.90	47.0%	6.4	5.6	5.7	7.2
Positive electrode	5	75.6	4.61	33.5%	50.3	25.3	231.8	32.4
Positive current collector	6	16.3	2.70	0.0%	16.3	0.0	44.0	0.0
Positive electrode	7	75.6	4.61	33.5%	50.3	25.3	231.8	32.4
Separator	8	12.0	0.90	47.0%	6.4	5.6	5.7	7.2
TOTAL		373.6	-	-			916.0	133.6

Figure 3.6: Mass and volume loadings of individual components in LGM50 jelly roll.

with the internal volume of a 21700 format cell (see Methods section for full details).

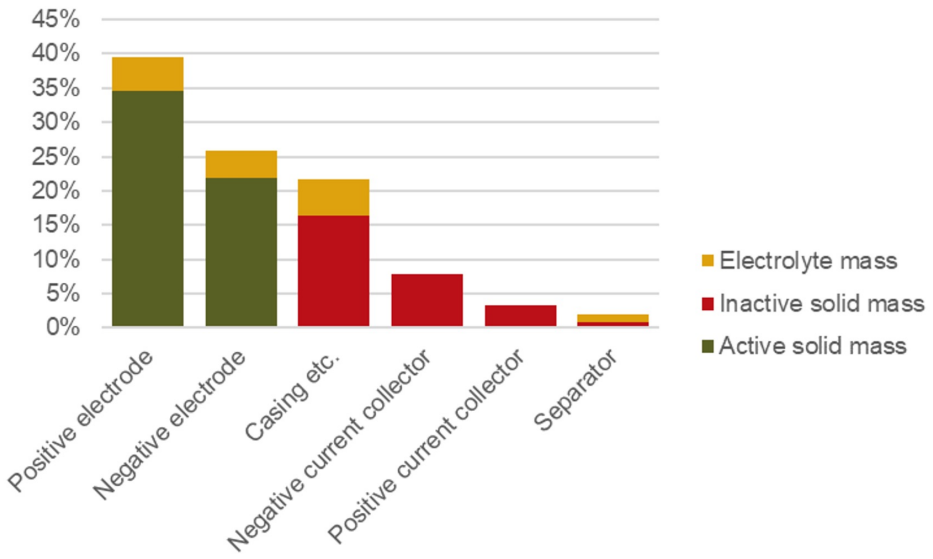
The result of these calculations is displayed as a Pareto, sorted by descending solid mass loading, in Figure 3.7. Most of the cell mass (57%) is related to active material. The cell casing accounts for 16% of cell mass and is the largest source of inactive mass. This finding is expected given the industry trend towards larger cell formats [52, 53], such as the Tesla 4680 and BYD blade, that minimise the casing mass per kW h. The calculations also show that there is an excess volume inside the casing that is not filled by the jelly roll. The jelly roll is typically wrapped in polymer and there will also be insulating gaskets at the top and bottom of the jelly roll. Additionally, this volume will be filled with current collector tabs, safety devices, and gas from the manufacturing environment. If it is assumed, for simplicity, that this excess volume has an average density equivalent to the electrolyte, then the excess mass would represent 5% of cell mass.

In terms of the jelly roll, the copper negative current collector accounts for 8% of cell mass. By comparison, the thicker but less dense aluminium positive current collector only accounts for 3% of cell mass. The next biggest contributor to inactive mass is electrolyte in the positive and negative electrodes. Finally the separator mass is evenly split between solid and electrolyte, which together account for 2% of cell mass. The mass of binder and conductive additive is included in the solid mass for each electrode, but will be minimal due to their low mass percentages.

In summary, most of the inactive mass in the LGM50 cell is associated with the casing. Beyond the casing, the remaining inactive mass is primarily associated with the metal current collectors and electrolyte within the electrodes. These findings suggest that research aiming to improve gravimetric cell energy should focus on the manufacture of freestanding (no separate current collector) and low porosity electrodes, with the caveat that low porosity electrodes must maintain equivalent or reduced overpotentials.

3.3.2 Overpotentials

As discharge rate is increased, the assumption of a high extent of lithiation or delithiation does not hold as overpotentials are no longer negligible (Figure 3.5). Three key overpotentials can



	Solid mass	Electrolyte mass
Positive electrode	35%	5%
Negative electrode	22%	4%
Casing etc.	16%	5%
Negative current collector	8%	0%
Positive current collector	3%	0%
Separator	1%	1%
Grand Total	**85%**	**15%**

Figure 3.7: A Pareto of solid and electrolyte mass by component for the LGM50 cell. As expected, most of the cell mass (57%) is related to active material. The cell casing accounts for 16% of cell mass and is the largest source of inactive mass. In terms of the jelly roll, the copper negative current collector accounts for 8% of cell mass. By comparison, the thicker but less dense aluminium positive current collector only accounts for 3% of cell mass. The next biggest contributor to inactive mass is electrolyte in the positive and negative electrodes. Finally the separator mass is evenly split between solid and electrolyte, which together account for 2% of cell mass. There is an excess volume inside the casing that is not filled by the jelly roll. The jelly roll is typically wrapped in polymer and there will also be insulating gaskets at the top and bottom of the jelly roll. Additionally, this volume will be filled with current collector tabs, safety devices, and gas from the manufacturing environment. If it is assumed, for simplicity, that this excess volume has an average density equivalent to the electrolyte, then the excess mass would represent 5% of cell mass (shown as "Casing etc. Electrolyte Mass").

be identified in a lithium-ion battery: Ohmic, concentration, and kinetic [54]. Figure 3.8 is a schematic of the overpotentials that exist in a battery during charging.

Firstly, there is an Ohmic overpotential associated with electronic conduction in the electrodes and current collectors. Materials with high electrical conductivity should be selected and conduction path lengths should be minimised to reduce this Ohmic overpotential. For particle-based electrodes, the electrical conductivity of the bulk electrode is lower than for the individual materials due to contact resistances between particles and at the interface between slurry and current collector [55]. There is also an Ohmic overpotential associated with ion transport in the electrolyte. Electrolytes with high lithium ion conductivity [56, 57, 58] should be used to minimise electrolyte Ohmic overpotential. Secondly, there is a concentration overpotential related to concentration gradients in the cell. Diffusion of lithium ions inside the active material creates a solid concentration overpotential. Similarly, diffusion and migration of both lithium ions and negative counter ions in the electrolyte creates an electrolyte concentration overpotential. Tortuosity increases path length of the electrolyte domain within the electrodes and should be minimised to reduce electrolyte concentration overpotential. The solid concentration overpotential can be reduced by selecting materials with higher lithium diffusivity or, in the case of a constant gravimetric current, increased gravimetric surface area. Finally, there is a kinetic overpotential associated with the charge-transfer reaction at the electrode-electrolyte interface. A high interfacial surface area can reduce areal current density and lower kinetic overpotential.

Each of these overpotentials will reduce the extent of lithiation or delithiation at end of charge or discharge. Compared to the inactive material losses, it is much harder to quantitatively break down the losses due to overpotentials and is beyond the scope of this chapter. It is well established in the literature that electrolyte overpotentials limit gravimetric energy density as discharge rate is increased [59, 60]. A high tortuosity electrode microstructure will increase the path length for ion transport in the electrolyte and increase the electrolyte overpotential. Research into electrodes with lower electrolyte overpotential should focus on reducing electrode tortuosity. Alternatively, electrolyte compositions with increased lithium ion conductivity could be used.

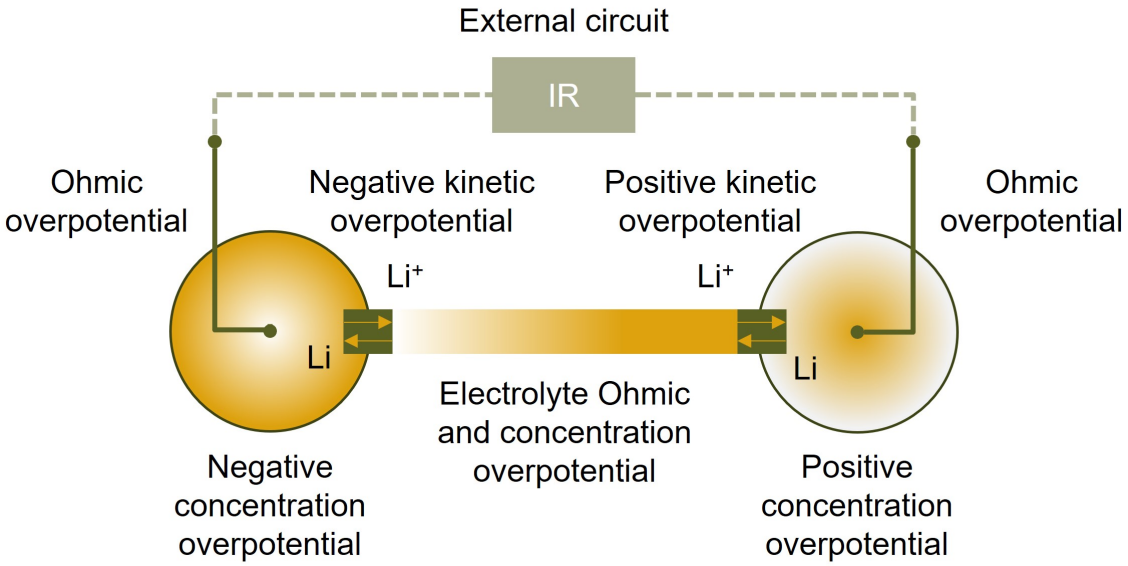


Figure 3.8: A schematic of the overpotentials that exist in a battery during charging. Lithium concentrations gradients will build up in the active materials and generate concentration overpotentials. Similarly, concentration gradients in the electrolyte will lead to electrolyte overpotentials. Kinetic overpotentials are related to the charge-transfer reactions occurring at the interfaces between active material and electrolyte. Finally, Ohmic overpotential results from conduction of ions and electrons.

3.4 Conclusions

This chapter has conducted a quantitative analysis of a commercial lithium-ion cell to reveal the key sources of loss. State-of-the-art commercial cells have gravimetric energy density of 250-300 $\mathrm{W\,h\,kg^{-1}}$ measured at a discharge rate of 0.1C. The LGM50 cell was selected as a representative commercial cell for more detailed quantitative analysis. The gravimetric energy density of the LGM50 cell is measured as 263 $\mathrm{W\,h\,kg^{-1}}$ at a discharge rate of 0.1C and falls as low as 70 $\mathrm{W\,h\,kg^{-1}}$ at a discharge rate of 4C.

Calculations show that the theoretical gravimetric energy density of the LGM50 cell chemistry is 510 $\mathrm{W\,h\,kg^{-1}}$. The LGM50 cell therefore only achieves 52% of its theoretical performance at low discharge rates, and less than 20% at high discharge rates. The difference between measured and theoretical performance can be attributed to two categories: inactive material and overpotentials. Besides the cell casing, the current collectors alone account for 11% of cell mass. An additional 9% of cell mass is accounted for by electrolyte filling the void volume of the electrodes. Alongside the inactive materials, overpotentials, in particular electrolyte overpotentials, severely hinder gravimetric energy density at elevated discharge rates.

It is important to acknowledge the limitations of the analysis performed in this chapter. Firstly, the existing cell chemistry is used to calculate the theoretical performance. This approach is useful to focus on improvements for an existing chemistry, however could miss opportunities associated with other chemistries. Secondly, conclusions are drawn based on the analysis of a single commercial cell. The LGM50 cell is sufficient to demonstrate this method of analysis but may not be representative of the latest commercial cells. Subject to availability of data, future work should repeat this analysis for a selection of the latest commercial cells to ensure representative and up-to-date conclusions can be drawn.

In summary, this chapter quantitatively reveals that the LGM50 cell only achieves 52% of its theoretical gravimetric energy density at a discharge rate of 0.1C, and less than 20% at a discharge rate of 4C. This finding highlights that there is potentially substantial opportunity to improve cell performance using existing cell chemistries. The key sources of loss are related to inactive materials and electrolyte overpotential. Research should therefore focus on methods of decreasing the inactive material content of cells and reducing overpotentials at elevated charge and discharge rates. Any improvements realised in these two areas will be chemistry-agnostic and therefore widely applicable.

3.5 Methods

Data for the LGM50 cell was retrieved from the parametrisation reported by Chen *et al.* [51] and is summarised in Table 3.1. LGM50 performance data was retrieved from the publicly available section of the Batemo website [3] and is summarised in Table 3.2.

Calculation of component mass and volume loadings in cell jelly roll

The thickness, solid density, and porosity of each component was obtained from the parametrisation data reported by Chen *et al.* [51]. The solid density of the positive and negative electrodes was calculated by assuming a composite of active material, binder and conductive additive in mass ratio of 95:2.5:2.5.

The volume and mass loadings of solid and electrolyte for each component were calculated

Table 3.2: Summary of Batemo performance data for LGM50 cell [3]

Parameter	Value
Geometry	
Mass / g	67.9
Dimensions / mm	21.15 × 70.4
External volume / cm^3	24.7
Electrochemical performance	
Capacity (nominal) / A h	4.80
Capacity (C/10) / A h	4.80
Current (continuous) / A	9.30
Current (peak) / A	21.0
Energy (C/10) / W h	17.8
Power (continuous) / W	32.4
Power (peak) / W	73.8
Energy density (gravimetric) / W h kg^{-1}	263
Energy density (volumetric) / W h L^{-1}	722
Power density (gravimetric) / W kg^{-1}	1090
Power density (volumetric) / W L^{-1}	2980

as follows:

$$\text{Solid volume loading} = \text{Thickness} \times (1 - \text{Porosity}) \tag{3.4}$$

$$\text{Electrolyte volume loading} = \text{Thickness} \times \text{Porosity} \tag{3.5}$$

$$\text{Solid mass loading} = \text{Solid volume loading} \times \text{Solid density} \tag{3.6}$$

$$\text{Electrolyte mass loading} = \text{Electrolyte volume loading} \times \text{Electrolyte density} \tag{3.7}$$

In calculating the electrolyte volume loading, it was assumed that 100% of void volume in each component is filled with electrolyte. Electrolyte was assumed to be 1M LiPF6 in EC:DMC

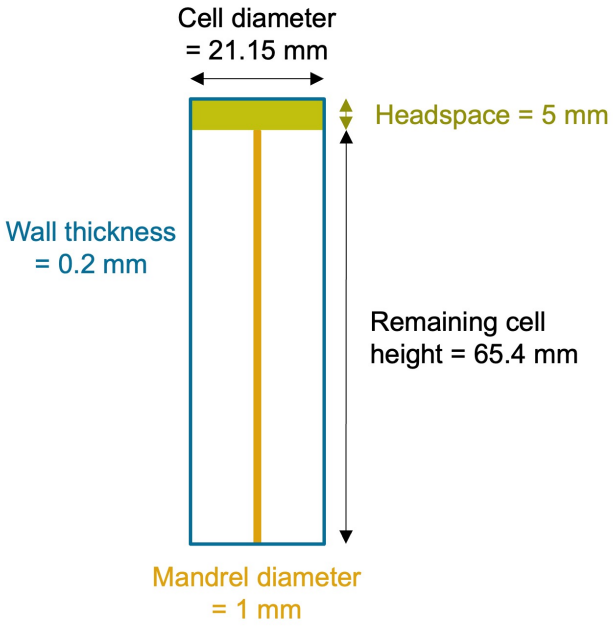


Figure 3.9: Dimensions of LGM50 21700 cell casing [3]

(1:1 vol.%) 99.9% with a density of 1.28 g cm^{-3} [61].

Calculation of cell energy density

The mass loading and volume loading of the jelly roll was used to calculate the cell energy density, and the volume and mass of each component in the final cell.

Following disassembly, the dimensions of the jelly roll were measured by Chen *et al.* as approximately 80 cm length and 6.5 cm width [51]. These figures equate to a jelly roll area of 518 cm^2. Combined with the jelly roll thickness from Figure 3.6 of 374 µm, the jelly roll volume can be calculated as 19.4 cm^3.

For comparison, the internal volume of a 21700 format cell is calculated as 22.2 cm^3 using the dimensions indicated in Figure 3.9. This calculated volume is greater than the volume of the jelly roll, indicating a packing efficiency of 87.3 %. The remaining internal cell volume will be filled with current collector tabs, safety devices, excess electrolyte, insulating materials, tape, and gas from the manufacturing environment. For the sake of simplicity in these calculations, the excess internal volume (2.80 cm^3) is assumed to have an average density equivalent to the electrolyte, equating to an excess mass in the cell of 3.6 g.

The cell energy and mass were calculated using equations 3.8 to 3.13. The mass and volume

of the solid and electrolyte of individual jelly roll components were also calculated to give a mass breakdown for the full cell (as shown in Figure 3.7).

First the stack mass, excess mass, and the cell energy are calculated:

$$\text{Stack mass} = \text{Wet stack mass loading} \times \text{Stack area} \tag{3.8}$$

$$\text{Excess mass} = (1 - \text{Packing efficiency}) \times \text{Casing internal volume} \times \text{Electrolyte density} \tag{3.9}$$

$$\text{Cell capacity} = \text{Positive areal capacity} \times \text{Stack area} \tag{3.10}$$

Note, it is the areal capacity of the positive electrode that is used as NP ratio is typically greater than 1 (the capacity of the positive electrode is lower than the negative electrode by design).

Then the cell mass is calculated:

$$\text{Cell mass} = \text{Stack mass} + \text{Casing mass} + \text{Excess mass} \tag{3.11}$$

Finally, gravimetric cell capacity and energy density is calculated:

$$\text{Gravimetric cell capacity} = \frac{\text{Cell capacity}}{\text{Cell mass}} \tag{3.12}$$

$$\text{Gravimetric cell energy density} = \text{Gravimetric cell capacity} \times \text{Average discharge voltage} \tag{3.13}$$

Chapter 4

Proof of concept: Patterned pyrolytic graphite sheet electrodes

Chapter 3 performed a quantitative analysis of a commercial cell to show that research and development efforts to improve gravimetric energy density for a given cell chemistry should focus on reducing inactive cell mass and overpotentials at elevated discharge rates. This chapter documents experimental work to manufacture and characterise a low inactive mass, low overpotential electrode using pyrolytic graphite sheet.

4.1 Battery electrodes today

Today, all mass market lithium-ion battery electrodes are manufactured by casting a slurry containing powdered active material on to a metal current collector foil [33]. There are typically four key steps to this process: mixing of the slurry, casting of the slurry on to a metal current collector, drying of the cast electrode slurry, and finally calendaring to achieve the desired electrode thickness and porosity (Figure 4.1). This process has enabled the mass manufacture of battery electrodes for decades; however, as revealed in Chapter 3, it produces electrodes with significant inactive material content and high overpotentials at elevated discharge rates.

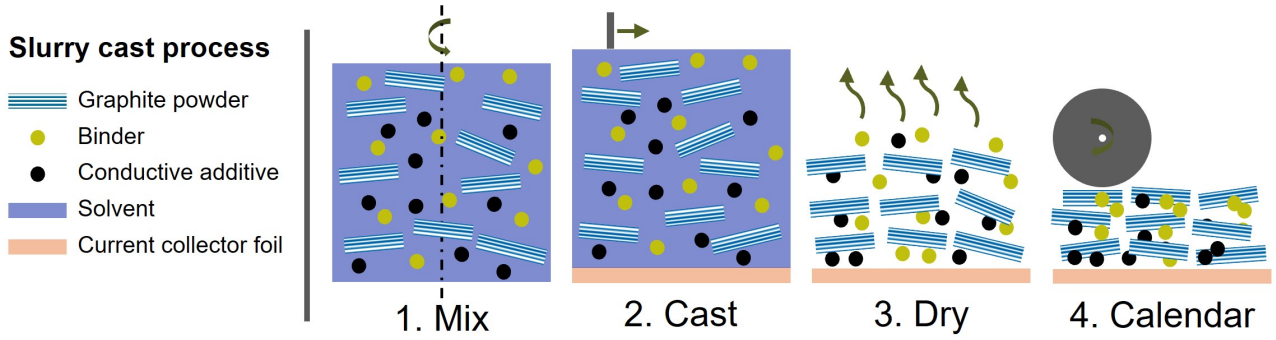


Figure 4.1: Today, all mass market lithium-ion battery electrodes are manufactured by casting a slurry containing powdered active material on to a metal current collector foil. There are typically four key steps to this process: mixing of the slurry, casting of the slurry on to a metal current collector, drying of the cast electrode slurry, and finally calendaring to achieve the desired electrode thickness and porosity.

4.1.1 Low overpotential electrodes

Electrodes designed for reduced overpotentials are widely reported in the literature. When a powder-based slurry is cast onto a metal foil in the conventional manufacturing process, the uncontrolled arrangement of particles creates a tortuous pore network for lithium ions to navigate during charge and discharge [33]. Tortuous pore networks lead to high electrolyte overpotentials and prevent full lithiation or delithiation of the active material before the cell cut-off voltage is reached. This problem is exacerbated for elevated discharge or charge rates [62, 63] and for thick electrodes where the lithium ions must travel a longer distance [64, 65, 66].

A range of methods are reported in the literature to reduce the overpotentials of battery electrodes and are widely reviewed [66, 65, 33, 67]. Most reports focus on reducing electrolyte overpotential by introducing electrolyte channels. Electrolyte channels can reduce the tortuosity of the electrolyte domain within electrodes and therefore limit the lithium concentration gradients that form during charge and discharge. There are three key approaches to creating an electrode with electrolyte channels: templating, additive manufacturing, and subtractive manufacturing.

Templating

In its simplest form, templating involves the addition of particles to the electrode slurry that are later removed by dissolution or pyrolysis. This approach is demonstrated in the literature using salt particles [68, 69], nylon micro-rods [70], hydrocarbon droplets [70] and solvents [71, 72]. Electrode porosity, pore size, and pore shape can be controlled with this approach, but a random porosity distribution is produced by default [65]. To instead form through-plane channels, superparamagnetic iron oxide nanoparticles can be added to the template particles and a magnetic field applied [70]. Use of a magnetic field offers more control over electrode architecture but requires additional manufacturing steps and is slow [65].

Wood templating has also been demonstrated in which wood is infiltrated with active material and then calcined [73]. Calcination in air will remove the wood leaving electrolyte channels. Alternatively, calcination in argon will retain the calcined wood as a current collector. Through-plane channels can be produced using wood templating, however the size and shape of these channels is determined by the wood microstructure and therefore difficult to control [65].

Finally, ice templating, in which the electrode slurry is frozen and then freeze-dried, is also demonstrated for control of electrode porosity [74, 75, 76]. The final porosity is controlled by changing the amount of water and a faster cooling rate leads to smaller pores. Directional freezing can be used to form through-plane channels in the electrode, but adds additional manufacturing complexity. A downside of this technique is that it produces electrodes with high porosity that can hinder both mechanical stability and volumetric capacity [65].

Additive manufacturing

Besides templating, additive manufacturing techniques including co-extrusion, direct ink writing and spray printing have been used to produce low overpotential electrodes [65, 66]. Co-extrusion of an active material and a template material that is later removed can be used to produce a porous architecture [77, 78, 79]. The volumetric fraction of template material will determine the final porosity and pore size will depend on the number of extrusion steps performed. Direct ink writing and spray printing both have three steps: ink preparation, printing and drying. For direct ink writing, a specified porous electrode geometry is formed by con-

trolling the location of active material deposition during printing [80, 71, 81]. Conversely, for spray printing, the porous electrode geometry is formed by controlling the drying temperature and ink formulation [82, 83, 84, 85]. Both direct ink writing and spray printing can be used to manufacture electrodes with layers or gradients. Spray printing offers higher throughput than direct ink writing, but less control over electrode architecture.

Subtractive manufacturing

Laser ablation has been used to create electrolyte channels in a range of slurry cast electrodes [86, 87, 88, 89]. Digital control of the laser permits the manufacture of complex electrode microstructures with high precision. Potential limitations of laser ablation are heating of the active material and a tapered geometry for high aspect ratio channels [66, 65]. Ultrashort pulse durations (ideally femtosecond) are preferred to avoid thermal effects [88]. As with any subtractive manufacturing technique, waste material is generated which could be an issue for precious and expensive materials, particularly if not recovered.

Overall, these approaches to forming a low overpotential electrode are still all focused on a slurry cast architecture. As a result, the porosity that is created using these approaches is in addition to the porosity that is already present in the dried slurry. High porosity electrodes will hinder cell level volumetric and gravimetric energy density. There are reports of controlling active material orientation without templating using a magnetic field [90], in which case no additional porosity is introduced. Additionally, spray printing can be used to manufacture graded electrode microstructures with lower porosity [91]. For all of these techniques, further work is needed to demonstrate suitability for mass manufacture [66, 65].

4.1.2 Low inactive material content electrodes

Chapter 3 highlighted that most of the inactive material content in slurry cast electrodes is accounted for by the current collectors. Free-standing electrodes [92, 93] eliminate the inactive mass of a separate metal current collector and could also circumvent issues with electrode-current collector de-lamination [94, 95], particularly for thick electrodes. However, although removal of the separate current collector should lead to higher energy density, it is not guar-

anteed without careful design. For instance, if the freestanding electrode has increased binder content or high porosity that is filled with electrolyte, the freestanding electrode may in fact lead to lower energy density at cell level.

Free-standing electrodes must ensure sufficient electrical and thermal conductivity, as well as mechanical robustness for cell manufacture. Some examples of free-standing carbon electrodes include lignin-, PAN-, and pitch-based carbon fibre mats [96, 97, 98]. These electrodes do not require a separate current collector, but the disordered carbons used tend to have lower initial coulombic efficiency and a higher lithiation voltage compared to graphite. Carbon fibre mats also tend to have high porosity which can lead to excessive electrolyte mass and low energy density at cell level.

Beyond carbon fibre mats, mechanical [99] and chemical [100, 92, 101] methods of removing the current collector from a slurry-cast electrode have been reported but mainly for characterisation rather than mass electrode manufacture. The resulting electrodes have low electrical conductivity and poor mechanical robustness, limiting their use in larger cell formats.

Overall, whilst freestanding electrodes are reported, further work is required to demonstrate mechanical robustness, sufficient electrical and thermal conductivity, and high energy density at commercial cell level.

4.2 Graphite feedstocks

This chapter aims to manufacture and characterise a low inactive mass and low overpotential graphite electrode. Chapter 3 showed firstly that the metal current collector is the key source of inactive mass in the LGM50 cell, and secondly that high tortuosity electrode microstructures lead to significant electrolyte overpotentials. The task is therefore to design a free-standing and low tortuosity battery electrode.

Free-standing graphite battery electrodes in the literature are limited by poor mechanical robustness, high surface area, high porosity, or high average lithiation potential [92, 93, 96, 97, 98]. To consider options for addressing these challenges, research was conducted into the different graphite feedstocks that are commercially available. Besides the graphite flakes that are conventionally slurry-cast to form battery electrodes, graphite is available in many different

forms. The graphite family refers to carbon materials with sp^2 hybridisation of the carbon atoms and a layered structure [102]. This family of materials includes graphite, turbostratic carbon, carbon fibres, carbon nanotubes, graphite oxide, exfoliated graphite, flexible graphite, graphene, activated carbon, and carbon black. Of these materials, carbon fibres, carbon nanotubes, graphene, and flexible graphite are reported as free-standing sheets.

Carbon fibres are used for lightweight structures due to their low density, high strength, and high modulus [102]. The main phase of carbon fibres is turbostratic carbon, which is noncrystalline carbon with carbon layers that do not exhibit the AB stacking sequence that is characteristic of graphite. Although carbon fibres can be weaved into free-standing mats [96, 97, 98], these mats are limited in their utility for battery electrodes due to high porosity. The turbostratic carbon phase also results in lower initial coulombic efficiency and a higher lithiation voltage compared to graphite. Free-standing carbon nanotube and graphene oxide sheets are reported as battery electrodes [103, 104]. Although these electrodes have high electrical conductivity and good mechanical properties, in each case the high surface area of the nanomaterials leads to prohibitively low initial coulombic efficiency as excessive solid electrolyte interphase forms.

There are two main forms of flexible graphite: particle-based flexible graphite sheet and pyrolytic graphite sheet [102]. Particle-based flexible graphite sheet is formed by compacting exfoliated graphite without binder. The resulting sheet has reasonable electrical conductivity ($1.25 \times 10^5\,\mathrm{S\,m^{-1}}$), thermal conductivity ($140\,\mathrm{W\,m\,K^{-1}}$), density (normally $1.12\,\mathrm{g\,cm^{-3}}$, up to $1.53\,\mathrm{g\,cm^{-3}}$, and tensile strength (5 MPa) [105]. Conversely pyrolytic graphite sheet is formed through graphitisation of a polymer sheet. Pyrolytic graphite sheet is available with higher density (up to $2.13\,\mathrm{g\,cm^{-3}}$), electrical conductivity (up to $2 \times 10^6\,\mathrm{S\,m^{-1}}$), thermal conductivity (up to $1950\,\mathrm{W\,m\,K^{-1}}$), and tensile strength (up to 40 MPa) than particle-based flexible graphite sheet [106]. Due to these attributes, pyrolytic graphite sheet was selected as a promising material for fabrication of a free-standing battery electrode and is discussed in detail in the following section.

4.3 Pyrolytic graphite sheet

Pyrolytic graphite sheet is a flexible, free-standing, and dense sheet that consists of only aligned stacks of graphene sheets (Figure 4.2). It is manufactured by Panasonic from polymer sheet precursors in two heat treatment steps [107]. The polymer sheet is first carbonised at 500-1000 °C and then graphitised at 2500-3200 °C. The resulting graphite sheet is finally calendared to a desired thickness and associated density (0.85-2.13 $\mathrm{g\,cm^{-3}}$), thermal conductivity (700-1950 $\mathrm{W\,m^{-1}\,K^{-1}}$) and electrical conductivity (1-2 $\times$ 10^6 $\mathrm{S\,m^{-1}}$) [106]. Pyrolytic graphite sheet also has reasonable tensile strength (20-40 MPa), a good heat resistance temperature (400 °C), and 180° bending around a 5 mm radius is demonstrated for 10,000 cycles [106]. For comparison, the thermal conductivity, electrical conductivity, and tensile strength of copper are 385 $\mathrm{W\,m^{-1}\,K^{-1}}$ [38], 60 $\times$ 10^6 $\mathrm{S\,m^{-1}}$ [38], and 250-300 MPa [108] respectively.

SEM images (Figure 4.2) show that the final pyrolytic graphite sheet has a smooth surface and is composed of stacks of graphene sheets. Some spacing is visible between the stacks of graphene sheets and responsible for the lower density (0.85-2.13 $\mathrm{g\,cm^{-3}}$) compared to the theoretical density of graphite (2.26 $\mathrm{g\,cm^{-3}}$). The density of pyrolytic graphite sheet is largely controlled by the final calendaring step during manufacture. A previous study used XRD to show that the graphite domains of pyrolytic graphite sheet have an interplanar spacing of 0.336 nm, mosaic angle spread of 8.2° and an in-plane lattice parameter of 0.246 nm [110]. Raman spectroscopy also revealed an $\mathrm{I}^G/\mathrm{I}^{G'}$ ratio of 3.1, typical of multi-layered graphite, and no D band within experimental error, indicating high crystallinity and minimal defect concentration [110].

Pyrolytic graphite sheet was identified as a promising candidate for manufacture of a battery electrode with low inactive material content for several reasons. Firstly, the similar density of pyrolytic graphite sheet compared to the theoretical density of graphite indicates that it has low porosity. Low porosity will limit the inactive mass and volume of electrolyte when used as a battery electrode. Secondly, pyrolytic graphite sheet contains only graphite and therefore has no inactive mass or volume associated with binder or conductive additive. Thirdly, pyrolytic graphite sheet is freestanding and has high electrical and thermal conductivity. These properties could enable use of pyrolytic graphite sheet directly as a battery electrode without a need

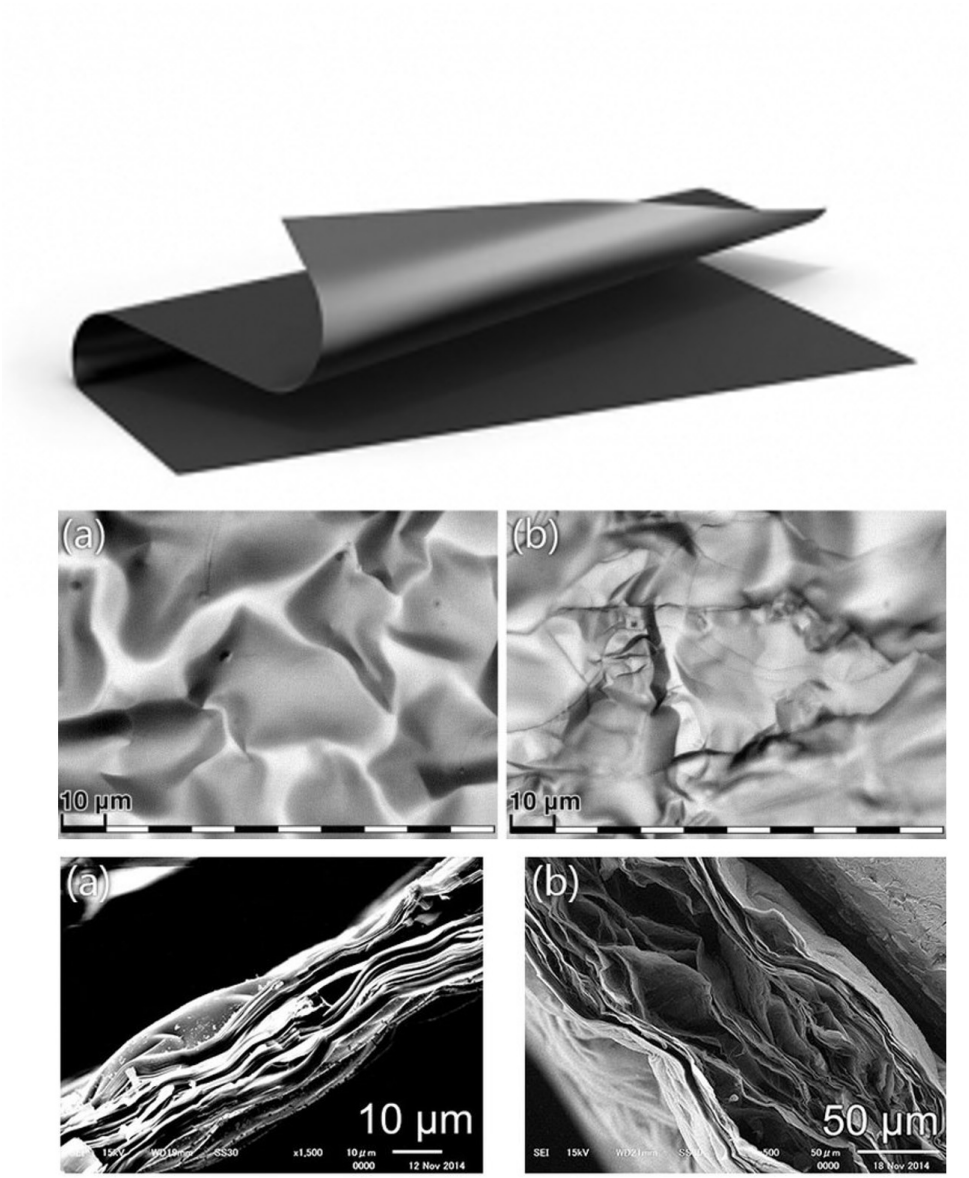


Figure 4.2: (A) Optical image of pyrolytic graphite sheet showing flexibility [106]. (B) SEM images of pyrolytic graphite sheet surface and cross-section [109].

for a separate metal current collector. Fourthly, the high crystallinity and minimal defect concentration of graphite are consistent with a low average discharge potential compared to Li/Li^+. Finally, pyrolytic graphite is available commercially and widely used as a thermal interface material for heat management in electronic devices such as phones and cameras [20, 107]. A supply chain for pyrolytic graphite sheet therefore already exists which could greatly reduce the risk and timeline for commercialisation of pyrolytic graphite sheet electrodes.

Pyrolytic graphite sheet cannot however be used directly as a battery electrode. Initial electrochemical testing with the as-manufactured pyrolytic graphite sheet in a lithium half cell measured negligible reversible capacity (less than 10 mA h g^{-1} at 0.1C, Figure 4.6). The as-manufactured pyrolytic graphite sheet is impermeable to electrolyte and has negligible through thickness lithium ion diffusivity ($10^{-15}\,m^2\,s^{-1}$, compared to $10^{-10}\,m^2\,s^{-1}$ parallel to the graphene plane) [111]. Together, these properties limit through-electrode transport of lithium and create high concentration and kinetic overpotentials.

Quantitatively, if we assume that the interface between active material and electrolyte is planar for the double-side pyrolytic graphite sheet electrode then there will be $2\,cm^2$ of active material-electrolyte interface per square cm of stack. By comparison, if the equivalent areal capacity slurry cast LGM50 negative electrode is composed of 11.72 µm diameter graphite discs (density $2.3\,g\,cm^{-3}$, theoretical capacity $372\,mA\,h\,g^{-1}$), then there will be $45\,cm^2$ of interface per square cm of stack (see Methods section for full calculation). In other words, the areal lithium flux at the interface between active material and electrolyte would need to be more than 20 times higher for pyrolytic graphite sheet. This far higher areal lithium flux would be expected to create prohibitively high concentration, kinetic and possibly electrolyte overpotentials.

There could however be an opportunity to exploit the layered, anisotropic microstructure of pyrolytic graphite sheet to produce a low overpotential electrode. The rest of this chapter will investigate the introduction of through-plane channels into pyrolytic graphite sheet.

4.4 Creating through-plane channels in pyrolytic graphite sheet

The introduction of through-plane channels into pyrolytic graphite sheet could increase lithiation capacity. Firstly, through-plane channels could provide a low tortuosity path for lithium to be transported in the electrolyte through the electrode. Diffusivity of lithium in the electrolyte (approximately $10^{-9}\,m^2\,s^{-1}$ [112]) is orders of magnitude greater than the out-of-plane diffusivity of lithium in graphite (approximately $10^{-15}\,m^2\,s^{-1}$ [111]). This low tortuosity path, compared to the tortuous path in slurry cast electrodes, could also ensure that electrolyte overpotentials are minimised at elevated current densities. Secondly, through-plane channels could increase the gravimetric surface area of the graphite in contact with the electrolyte. Higher gravimetric surface area will minimise areal current density and reduce kinetic and concentration overpotential. By exposing the edges of the layered graphite domains to electrolyte inside the through-plane channels, diffusion in the graphite domain will primarily be in-plane. The in-plane diffusivity of lithium in graphite ($10^{-10}\,m^2\,s^{-1}$ [111]) is five orders of magnitude higher than out-of-plane. Higher diffusivity will help to minimise concentration overpotential in the graphite. In summary, through-plane channels in pyrolytic graphite sheet could enable a low overpotential, low inactive mass electrode to be formed.

To test this hypothesis, experiments were planned to manufacture and characterise pyrolytic graphite sheet electrodes with through-plane channels. Laser cutting or drilling offers a precise, digital method of patterning substrates [88]. There are numerous reports in the literature of laser drilling slurry cast electrodes [86, 87, 88, 89] but not pyrolytic graphite sheet. A number of trials were therefore conducted to determine the suitability of laser cutting and drilling for patterning of pyrolytic graphite sheet (see Appendix for details).

Overall, the laser trials successfully demonstrated use of a laser to introduce through-plane channels into pyrolytic graphite sheet. Laser cutting, rather than drilling, was identified as the most suitable method of reliably producing arrays of channels with controlled channel diameter. Different channel diameters were cut and arrays of 100 µm diameter channels were shown to be most reliably manufactured (Figure 4.3).

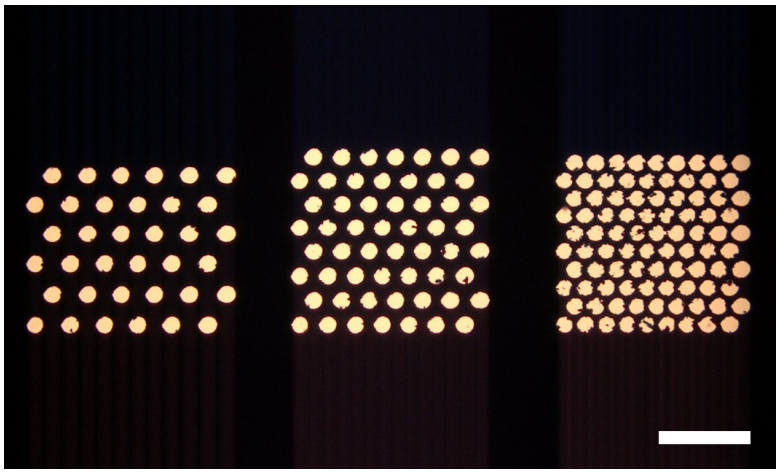


Figure 4.3: Optical micrographs from manufacturing trials showed that hexagonal arrays of 100 µm diameter channels could be reliably manufactured with 200 µm, 160 µm and 120 µm channel pitch. Scale bar, 500 µm.

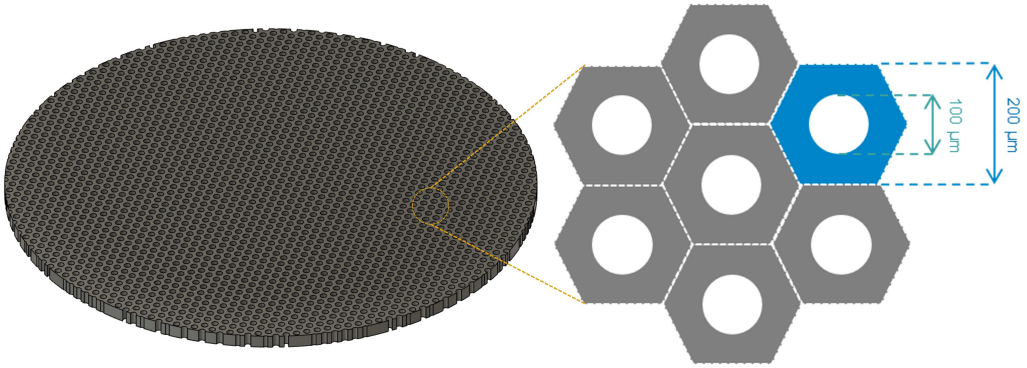


Figure 4.4: CAD model of sheet electrode patterned with hexagonal array of cylindrical channels. A single unit cell (blue) of hexagonal array is highlighted with 100 µm channel diameter and 200 µm channel pitch.

4.5 Electrode manufacture

Having shown that arrays of 100 µm diameter channels could be reliably laser cut in pyrolytic graphite sheet, the next step was to manufacture a series of electrodes for characterisation. The purpose of electrode manufacture and characterisation was to test our hypothesis that the introduction of through-plane channels into pyrolytic graphite sheet could improve lithiation capacity and enable its use as a battery electrode.

Three different electrode designs with hexagonal arrays of channels (Figure 4.4) were manufactured using a laser micromachining system. Each design used the same channel diameter (100 µm) but a different channel pitch (200 µm, 160 µm, or 120 µm) (Figure 4.5A). The respective porosities of these designs due to channels were 23%, 35%, and 63%. The channel diameter

was fixed at 100 µm to ensure adequate electrode wetting and reliable manufacture. Channel pitch was varied to investigate its impact on electrochemical performance. Control electrodes without electrolyte channels were also cut from both pyrolytic graphite sheet and a commercial slurry cast graphite negative electrode sheet (31% porosity).

The optical micrographs in Figure 4.5A show that the electrolyte channels were successfully cut with a narrow diameter distribution centred at 98 and 96 µm, respectively, for the 200 and 160 µm pitch arrays. The channels were less cleanly cut for the 120 µm pitch array, as reflected in the broader distribution of channel diameters centred at 90 µm.

The 160 µm pitch electrode was investigated in more detail using SEM and Raman. The SEM micrograph (Figure 4.5B) shows that the electrolyte channels are not perfectly smooth. A rough interface between active material and electrolyte could be beneficial as it will increase the surface area for the charge transfer reaction and reduce kinetic overpotentials. On the other hand, high surface area could lead to excessive formation of solid electrolyte interphase and low initial coulombic efficiency. The Raman map in Figure 4.5C indicates that the relative intensity of the G band, which is a measure of the degree of graphitisation, was lower near the cut surface. This reduction in the degree of graphitisation at the cut surface could be indicative of a heat-affected zone from laser drilling in ambient conditions.

4.6 Electrode characterisation

To test the electrochemical performance of the manufactured electrodes, coin cells were assembled using lithium metal as the counter electrode and the graphite electrode under investigation as the working electrode. Three coin cells were assembled for each electrode type (Table 4.2), so 15 coin cells were assembled in total. Full assembly details are provided in the Methods section.

Following assembly, each coin cell was rested for 10 hours to allow time for the electrodes to wet with electrolyte. At the end of the rest period, the open-circuit voltage of the cells was approximately 2.7 V which is consistent with the potential of fully delithiated graphite compared to Li^+/Li. The rested cells were then subjected to discharge-charge testing, following the protocol in Table 4.3 of the Methods section, to measure the lithiation capacity of the

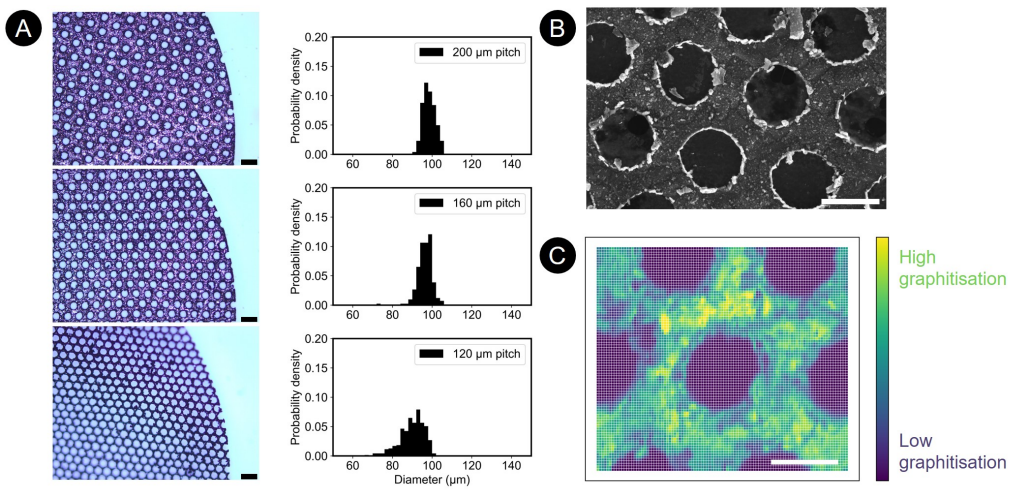


Figure 4.5: (A) Optical micrographs and corresponding channel diameter histograms of pyrolytic graphite sheet electrodes with hexagonal arrays of 100 µm channels spaced at 200, 160 and 120 µm pitch. Scale bars, 200 µm. (B) Scanning electron micrograph of pyrolytic graphite sheet electrode with hexagonal array of 100 µm channels spaced at 160 µm pitch. Scale bar, 100 µm. (C) Raman map for pyrolytic graphite sheet electrode with hexagonal array of 100 µm channels spaced at 160 µm pitch with colour bar showing maximum relative intensity between 1500 and 1600 cm^{-1}. Scale bar, 100 µm.

graphite at different discharge-charge rates.

The discharge-charge rates used for testing were determined based on the mass of graphite in each electrode, with 1C being equivalent to 372 mA per gram of graphite. Three cycles were performed at each discharge-charge rate and the cells were rested for 1 hour each time the rate was changed. In each discharge-charge cycle, the cells were discharged (which is equivalent to graphite lithiation in a negative electrode half cell) at a constant discharge rate of 0.1C until a lower cut-off voltage of 5 mV was reached. Upon reaching this lower cut-off voltage an equal and opposite current was applied to charge the cells (the graphite was delithiated) until an upper cut-off voltage of 1.5 V was reached. The lithiation or delithiation capacity within each discharge or charge step was calculated by taking the the product of the constant current and elapsed time. All capacities are quoted as capacity per unit mass of graphite.

4.6.1 Discharge-charge rate ramp

Figure 4.6A shows that the as-received pyrolytic graphite sheet achieved a reversible lithiation capacity of less than 10 mA h g^{-1} at 0.1C. This low lithiation capacity was anticipated given that pyrolytic graphite sheet is both impermeable to electrolyte and has low through-plane lithium

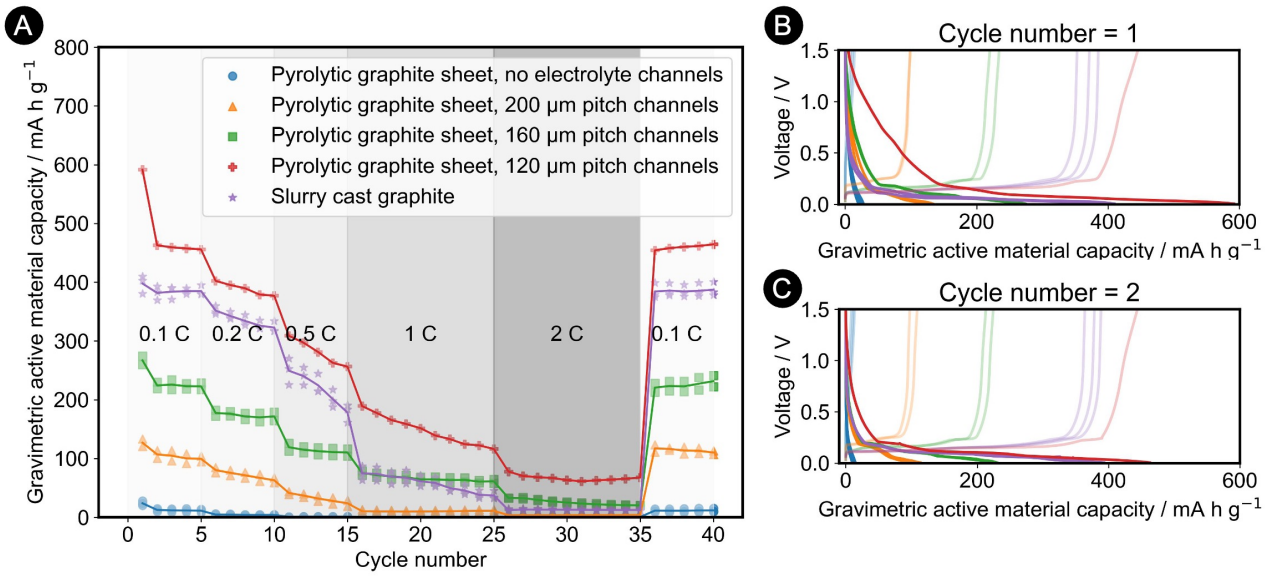


Figure 4.6: (A) Galvanostatic cycling between 5 mV and 1.5 V at indicated charge rates between 0.1C and 2C. Lithiation capacity is normalised to active material mass. Multiple repeats are shown with cells that showed unstable cycling removed for clarity (full data is shown in Figure 4.11). Line indicates mean capacity for each electrode type. Lithiation and delithiation (faded) voltage (vs. Li^+/Li) profiles for cycles 1 and 2 are shown in (B) and (C) with colours matched to (A).

ion diffusivity. By introducing electrolyte channels in a hexagonal array with a 200 µm pitch, the reversible lithiation capacity of the pyrolytic graphite sheet was shown to increase 10-fold to 100 mA h g^{-1} at a cycling rate of 0.1C. The electrodes with a narrower array pitch (160 µm) had a higher reversible lithiation capacity of 225 mA h g^{-1} at 0.1C, and the electrodes with the narrowest array pitch (120 µm) had a reversible lithiation capacity of more than 450 mA h g^{-1} at 0.1C. For comparison, the control slurry cast electrode had a reversible lithiation capacity of 385 mA h g^{-1} at 0.1C.

These results are consistent with our hypothesis that the introduction of through-plane channels into pyrolytic graphite sheet will minimise overpotentials and increase lithiation capacity. Furthermore, the lithiation capacity of the pyrolytic graphite sheet electrodes increased as the pitch was decreased. This finding is consistent with concentration and kinetic overpotentials being minimised as gravimetric surface area is increased.

A similar trend in lithiation capacities was observed at increased discharge-charge rates, with the 120 µm pitch electrode design consistently achieving the highest lithiation capacity. Interestingly, at 1C and 2C, the lithiation capacity of the pyrolytic graphite sheet with 160

µm pitch channels was higher than the slurry cast electrode (Figure 4.6A), whereas at lower discharge rates the slurry cast electrode capacity was higher. This result could be an indication that the slurry cast electrode is more strongly limited by electrolyte overpotentials at elevated current densities. This finding would be consistent with the more tortuous microstructure of the slurry cast electrode compared to the electrodes with through-plane channels.

The staged intercalation of lithium into graphite [113, 114] was visible as a series of plateaus in the voltage-capacity profiles (Figure 4.6B/C). All electrodes showed irreversible capacity in the first cycle due to solid electrolyte interphase formation. The irreversible first cycle capacity increased as the pitch was decreased for the pyrolytic graphite sheet electrodes, which correlated well with the calculated gravimetric surface area for each design (Figure 4.12). After the first cycle, irreversible capacity was negligible for all electrode types (Figure 4.13).

It is also worth noting that the narrowest array pitch (120 µm) electrodes exceed the theoretical lithiation capacity of graphite (372 mA h g^{-1}) at 0.1C. Higher values are often observed and usually attributed to defects in the graphite lattice that create additional sites for reversible lithium ion storage [114]. Laser drilling was conducted in the presence of oxygen for this study and Raman data (Figure 4.5C) shows a reduction in the degree of graphitisation close to the cut electrode surface, consistent with the introduction of defects.

Overall, these results demonstrate that with appropriate patterning the lithiation capacity of pyrolytic graphite sheet can be increased by more then forty times to 450 mA h g^{-1}. This high lithiation capacity of pyrolytic graphite sheet with through-plane channels highlights it as a promising active material for battery electrodes.

4.6.2 Extended cycling at 1C

The cells were also charged and discharged for 100 cycles at 1C to evaluate the performance over a larger number of cycles (Figure 4.7). After 100 cycles, the reversible capacity of the pyrolytic graphite sheet with 120 µm pitch electrolyte channels was more than 200 mA h g^{-1}, far higher than that of the slurry cast control electrode (less than 10 mA h g^{-1}). Interestingly, all of the pyrolytic graphite sheet electrodes showed a decline in reversible capacity during the first 20 cycles, followed by an increase. One possible hypothesis is that this decline and then

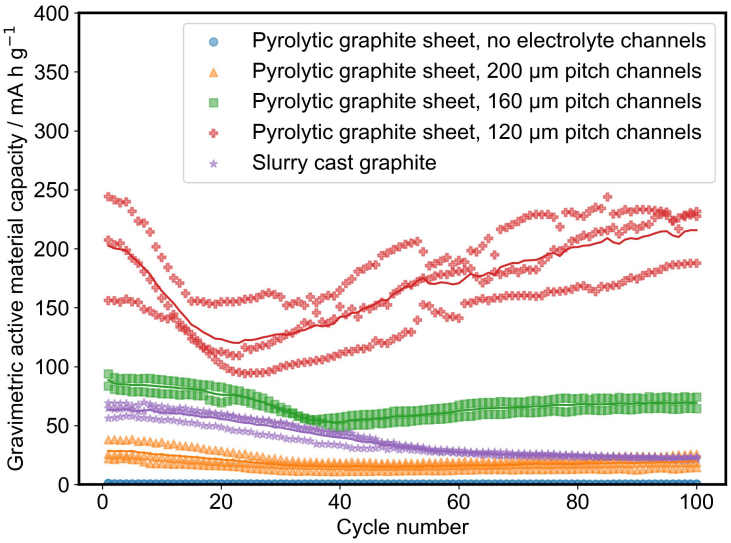


Figure 4.7: The cells were cycled for 100 cycles at 1C (constant current discharge-charge protocol). Lithiation capacity is normalised to mass of active material. Multiple repeats are shown and line indicates mean capacity for each electrode type.

increase in reversible capacity is due to the formation of lithium ion concentration gradients in the electrode with a constant current discharge-charge protocol. Without a constant voltage charge step, the graphite is not necessarily fully emptied of lithium before the next discharge step (graphite lithiation in half-cell configuration) commences. This shape has been observed previously for low tortuosity electrodes [90]. Further consideration of possible hypotheses and investigation is required to determine the cause of this behaviour. Manufacture of the 120 µm channel pitch electrodes was less consistent than for the larger pitch designs (Figure 4.5A) and could be the cause of increased variability in electrochemical performance between repeats (Figure 4.7).

In summary, the pyrolytic graphite sheet electrodes show improved capacity retention compared to the slurry cast electrode over 100 cycles at 1C. Due to the use of a constant current discharge-charge protocol, it difficult to distinguish whether the loss in capacity is the result of accumulated overpotentials or degradation. Further testing with a constant current - constant voltage protocol is recommended. Regardless, the results for the pyrolytic graphite sheet electrodes are promising compared to the slurry cast electrode.

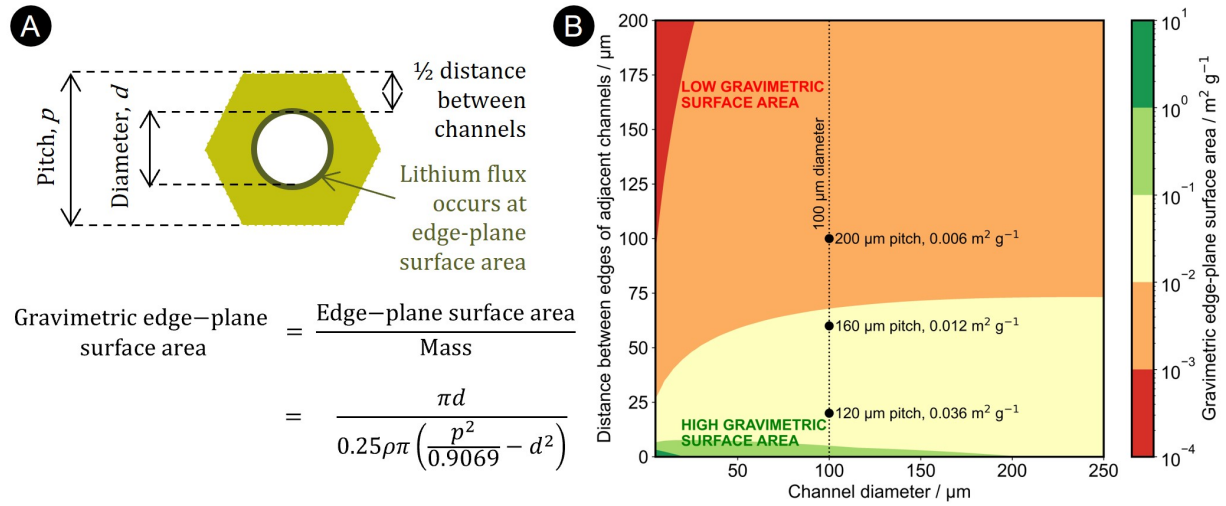


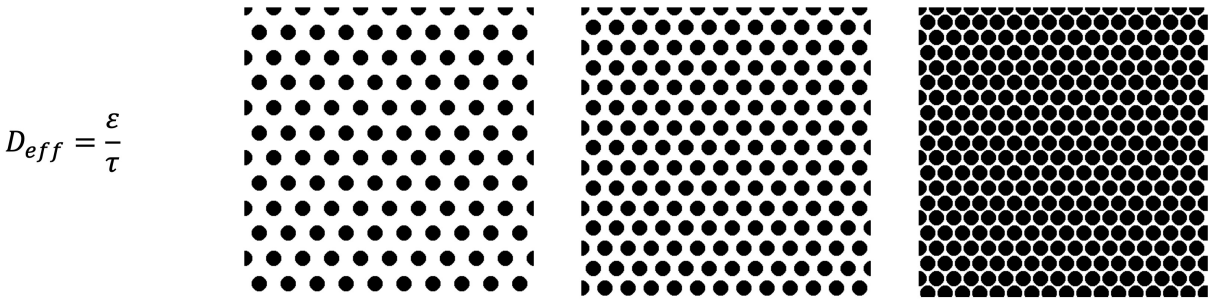
Figure 4.8: (A) The unit cell of a hexagonal array of cylindrical channels is defined by channel diameter and pitch. Gravimetric edge-plane surface area can be calculated from these two parameters if material density, ρ is known. (B) Gravimetric edge-plane surface area is plotted as a function of channel diameter and distance between edges of adjacent channels. The target region for high gravimetric edge-plane surface area is in the bottom left corner, representative of small, closely packed channels.

4.7 Gravimetric surface area

For the three manufactured electrode designs, as channel pitch was reduced from 200 µm to 120 µm, gravimetric capacity increased by 4.5 times from 100 mA h g^{-1} to 450 mA h g^{-1} at 0.1C. This increase in gravimetric capacity can in part be explained by considering gravimetric surface area.

A hexagonal arrays of channels can be defined using a unit cell with two parameters: channel diameter and pitch (Figure 4.8A). The combination of these two parameters determines the gravimetric surface area of the final electrode (Figure 4.8B). The edge-plane surface area is the surface area of the inside of the channels and ignores the basal-plane surface area on the top and bottom of the electrode. For a fixed channel diameter, channel pitch is inversely related to gravimetric surface area; a smaller pitch increases gravimetric edge-plane surface area (Figure 4.8B). As channel pitch was reduced from 200 µm to 120 µm, gravimetric edge-plane surface area increased by a factor of 6 from 0.006 m^2 g^{-1} to 0.036 m^2 g^{-1} for the manufactured electrodes.

The gravimetric surface area of the electrode-electrolyte interface plays a critical role in the performance of a lithium ion battery. In general, a larger gravimetric surface area (m^2



Diameter	100 µm	100 µm	100 µm
Pitch	200 µm	160 µm	120 µm
Porosity, $(1-\varepsilon)$	23%	36%	63%
Tortuosity factor, τ	1.3	1.4	1.8
Effective transport, D_{eff}	0.62	0.45	0.21

Figure 4.9: The effective conductivity for the three channel designs manufactured in this chapter was estimated as 1.5 to 5 times lower than for the sheet without channels. This analysis was performed using TauFactor, an "open-source application for calculating tortuosity factors" [115].

g^{-1}) allows the current per unit surface area (A m^{-2}), or equivalent flux of lithium ions, to be reduced when a cell is discharged or charged at a fixed gravimetric current density (mA g^{-1}). A reduced lithium ion flux is beneficial for electrode capacity in two ways. Firstly, the kinetic overpotential is reduced, allowing higher lithium ion concentrations at the electrode-electrolyte interface to be reached before cut-off. Secondly, at lower areal current densities, a shallower lithium concentration gradient develops inside the active material. Together, these factors allow more lithium to enter the active material before the cut-off voltage is reached, resulting in a higher lithiation capacity.

In summary, channel diameter must be paired with a suitable channel pitch to maintain high gravimetric surface area within the electrode. However, increasing the gravimetric surface area of the electrode can also have drawbacks. A larger surface area can lead to a higher irreversible capacity during the first cycle, as more of the electrode is exposed to the electrolyte and SEI formation is increased. SEI formation can decrease the coulombic efficiency of the battery and reduce its capacity over time. Additionally, as channel pitch is reduced for a fixed channel diameter, the electrode porosity will increase. High electrode porosity will increase the mass and volume of electrolyte and reduce gravimetric energy density.

4.8 Effective conductivity

Introducing electrolyte channels will reduce the effective electrical and thermal conductivity of pyrolytic graphite sheet. Channels will decrease cross-sectional area and increase conduction path length. Cross-sectional area decreases with porosity, for instance 63% porosity corresponds to a 63% reduction in cross-sectional area. At the same time, the path length for conduction increases as electrons must navigate around the channels. In the worst case, where electrons travel around the circumference of channels, the conduction path length increases by approximately 1.5 times (from d to $0.5\pi d$ for each channel, where d is the channel diameter). Combined with the reduced cross-sectional area, overall, the electrical resistance will increase, and the rate of heat transfer will decrease, by up to five times for materials with higher porosity (e.g. 63%) and 1.5 to 2 times for those with lower porosity (e.g. 10%). These rough calculations were validated using TauFactor, an "open-source application for calculating tortuosity factors" [115]. The effective conductivity for the three channel designs manufactured in this chapter was estimated as 1.5 to 5 times lower than for the sheet without channels, consistent with the rough calculations (Figure 4.9).

4.9 Conclusions

This chapter investigates the manufacture of a low inactive mass, lower overpotential battery electrode using pyrolytic graphite sheet. Pyrolytic graphite sheet was identified as a promising material for manufacture of a low inactive mass battery electrode as it is freestanding, dense and contains no binder or conductive additive. As-manufactured pyrolytic graphite sheet is however both impermeable to electrolyte and has low through-plane lithium diffusivity. Together these properties severely limit its lithiation capacity to less than $10\,\mathrm{mA\,h\,g^{-1}}$. The introduction of through-plane channels was therefore investigated in an attempt to increase lithiation capacity.

Initial trials showed that laser cutting was a suitable method for reliably introducing arrays of 100 µm diameter through-plane channels into pyrolytic graphite sheet. Next, a series of electrodes were manufactured with hexagonal arrays of 100 µm diameter channels. Discharge-charge cycling was conducted and revealed a 40-fold increase in the lithiation capacity of py-

rolytic graphite sheet to 450 mA h g^{-1} following introduction of 120 µm pitch channels. The pyrolytic graphite sheet electrodes also showed good capacity retention after 100 discharge-charge cycles at 1C. Overall, these results demonstrate a dramatic improvement in lithiation capacity of pyrolytic graphite sheet following the introduction of through-plane channels. With careful design pyrolytic graphite sheet could be used as a low inactive mass, low overpotential battery electrode.

Three different designs with pitch of 200 µm, 160 µm or 120 µm were manufactured. Discharge-charge cycling showed that lithiation capacity of pyrolytic graphite sheet strongly depends on the pitch of through-plane channels. As pitch is reduced for a fixed channel diameter, gravimetric surface area increases and areal current density is reduced. A lower areal current density minimises concentration and kinetic overpotentials and results in a higher lithiation capacity. However, although high porosity designs maximise the capacity normalised to mass of active material, they are not necessarily suitable for a practical cell. As electrode porosity is increased, the mass and volume of electrolyte will increase and gravimetric cell energy density will reduce. The next chapter will compare different methods of normalisation and introduce a methodology for estimating the gravimetric energy density of a commercial cell from laboratory electrode characterisation data.

Besides optimising electrode design for high gravimetric energy density at commercial cell level, several other criteria must be met for commercialisation [39]. Testing with more representative cycling protocols and larger cell formats is required to fully evaluate the potential of pyrolytic graphite sheet electrodes. Similarly, laser drilling was used in this study to prototype the electrodes, and may be applicable to large scale production, but alternative methods of forming an active material sheet with channels could be more suitable. Mechanical robustness, residues from channel creation, and channel clogging are all important considerations for mass manufacture [116]. Investigation will also be required into the electrolyte wetting of this novel electrode design, and methods of connecting or creating tabs. Pyrolytic graphite sheet has a similar manufacturing route to the powdered synthetic graphite used in today's batteries, but requires only a single patterning step for transformation into a battery electrode. Compared to the many complex steps of the slurry casting method for powders, there may be potential for

significant energy and cost savings, not least by avoiding the use of solvents, but further work is required before a detailed assessment can be made. Finally, the electrical and thermal conductivity of pyrolytic graphite sheet is orders of magnitude higher than slurry cast electrodes, even after accounting for electrolyte channels. Testing in full cell configuration with a practical cell format (e.g. 21700) could reveal additional performance benefits related to reduced Ohmic resistance and more uniform thermal dissipation.

In summary, this chapter demonstrates that, following the introduction of electrolyte channels, the gravimetric active material capacity of pyrolytic graphite sheet increases by a factor of 40 to 450 $\mathrm{mA\,h\,g^{-1}}$. This increase could enable the use of pyrolytic graphite sheet to manufacture a low inactive mass, low overpotential electrode. More generally, patterning of a monolithic active material sheet is demonstrated as a potential alternative to slurry casting for battery electrode manufacture. This alternative method has the potential to improve battery sustainability and performance by eliminating inactive materials and solvents, and creating a regular and low-tortuosity electrode microstructure. By avoiding the conventional particle-based battery electrode architecture, there could be additional benefits related to manufacturing, energy intensity, cost, thicker electrodes, fast charging, safety, degradation, thermal management and lifetime. While the method was demonstrated specifically for negative graphite lithium-ion electrodes in this study, it has the potential to be adapted for use in the production of both negative and positive electrodes across various battery chemistries [117].

4.10 Methods

Starting materials

Pyrolytic graphite sheet (EYGS091203, 25 µm thickness, Panasonic) and a commercial graphite negative electrode sheet on copper foil (bc-cf-241-ss-005, 41 µm thickness, MTI) were both used as received.

Table 4.1: Specification of the Oxford Lasers A series micromachining system used for electrode manufacture.

Parameter	Value
Average laser power / W	12
Wavelength / nm	355
Pulse repetition rate / kHz	50
Cut speed / mm s^{-1}	20
Laser type	Diode-pumped solid-state

Table 4.2: Five different electrode types were manufactured.

Electrode type	Description
PGS000	Pyrolytic graphite sheet (8 mm diameter), no electrolyte channels
PGS200	Pyrolytic graphite sheet (8 mm diameter), hexagonal array of electrolyte channels (100 µm diameter, 200 µm pitch)
PGS160	Pyrolytic graphite sheet (8 mm diameter), hexagonal array of electrolyte channels (100 µm diameter, 160 µm pitch)
PGS120	Pyrolytic graphite sheet (8 mm diameter), hexagonal array of electrolyte channels (100 µm diameter, 120 µm pitch)
SCG000	Slurry cast graphite sheet on copper foil (8 mm diameter), no electrolyte channels

Laser cutting of electrodes and electrolyte channels

A compact laser micromachining system (A series, Oxford Lasers) was used for cutting of electrodes from the starting material sheets and introduction of electrolyte channels. A G-Code script was developed to allow fast manufacture of electrodes with different channel diameter, channel pitch, and electrode diameter values. Specifications for the laser micromachining system used for electrode manufacture are presented in Table 4.1. Five different electrode types were manufactured, as detailed in Table 4.2.

Electrode characterisation

All samples were washed in ethanol and dried at 80 °C for 1 hour prior to analysis. Optical micrographs were collected on a Leica DM2500 microscope. The scanning electron microscopy samples were mounted using carbon tape and analysed using a JSM-6010LA scanning electron microscope with a 20 kV accelerating voltage. Raman spectroscopy was performed using a Renishaw inVia Raman microscope with a 50 mW 532 nm laser. The field of view was divided

into a grid of 4 µm x 4 µm squares and a streamline measurement was taken for each grid square at 100% laser power with a 1 s exposure time. The map was constructed by plotting the maximum relative intensity between 1500 and 1600 cm^{-1} for each square.

Coin cell assembly

Prior to assembly, all cell components and electrodes were washed in ethanol and dried under dynamic vacuum at 80 °C for 12 hours before transfer to an argon glove box (M-Braun) with O_2 less than 0.5 ppm and H_2O less than 0.5 ppm. Three cells were prepared for each of the five electrode types in Table 4.2. The electrodes were assembled into coin cells with a 0.12 mm thickness lithium metal counter electrode (LI00-FL-000105, Goodfellow) and a 16 mm diameter Whatman GF/A glass fibre separator (WHA1820-021, Merck, 0.26 mm thickness, 1.6 µm pore size). The as-purchased lithium foil was punched into 10 mm diameter circles for use as an electrode. Two 75 µL quantities of lithium hexafluorophosphate solution in ethylene carbonate and dimethyl carbonate (746711-100ML, Merck) were added as electrolyte before and after the separator. As this volume of electrolyte represents an excess compared to the pore space in the electrodes (an 8 mm diameter, 25 µm thickness disc has a total volume of 1.3 µL), it was kept constant across electrode designs. The full cell stack with component details is shown in Figure 4.10. Two 0.5 mm thick spacers were used in each cell. A hydraulic crimper (MSK-110, MTI) was used to seal the coin cells at a pressure of 7 bar before removal from glove box. All cells were rested for 10 hours prior to electrochemical characterisation to facilitate electrode wetting.

Electrochemical characterisation

To determine the rate capacity and capacity retention of the cells, galvanostatic electrochemical cycling was conducted between 5.0 mV and 1.5 V at different charge rates (5 cycles were performed at 0.1C, 0.2C and 0.5C, followed by 10 cycles at 1C and 2C, and 5 cycles at 0.1C). The protocol is detailed in Table 4.3. A further 100 cycles were performed at 1C to assess the capacity retention of the cells at a higher charge rate. Both charging and discharging were performed using a constant current procedure. The C rate was calculated based on a

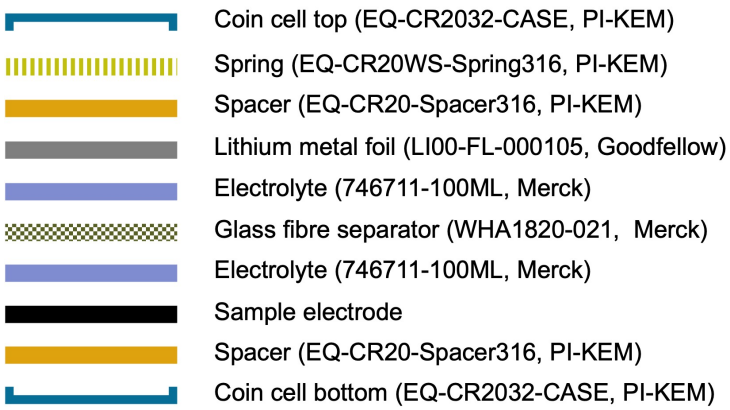


Figure 4.10: Components of coin cell stack in order of assembly with product codes and suppliers.

theoretical capacity of 372 mA h per gram of graphite. All measurements were performed at room temperature (25 °C). Prior to each change in cycling rate, the cells were rested for 1 hour at open circuit voltage (OCV) to allow for electrode equilibration.

Calculating porosity of a hexagonal array of circular channels

For a unit cell consisting of a solid hexagon with a circular channel at its centre, its porosity can be calculated as follows:

$$\text{Porosity} = \frac{\text{Channel area}}{\text{Hexagon area}} \tag{4.1}$$

$$\text{Channel area} = \frac{\pi d^2}{4} \tag{4.2}$$

$$\text{Hexagon area} = 6\tan(30^\circ)(\frac{p^2}{4}) = \frac{1}{0.9069}\frac{\pi p^2}{4} \tag{4.3}$$

where d = channel diameter, and p = channel pitch

The packing density for circles in a hexagonal array is 0.9069. Using this number, the above equations can be combined into a single equation for porosity of a hexagonal unit cell with a circular channel at its centre:

Table 4.3: A half cell constant current protocol adapted from literature [118]

Step	Description	Repetitions
Discharge (CC) Charge (CC)	0.1C until $U < 0.005\,\mathrm{V}$ 0.1C until $U > 1.5\,\mathrm{V}$	5
Rest	Rest for 1 hour at OCV	1
Discharge (CC) Charge (CC)	0.2C until $U < 0.005\,\mathrm{V}$ 0.2C until $U > 1.5\,\mathrm{V}$	5
Rest	Rest for 1 hour at OCV	1
Discharge (CC) Charge (CC)	0.5C until $U < 0.005\,\mathrm{V}$ 0.5C until $U > 1.5\,\mathrm{V}$	5
Rest	Rest for 1 hour at OCV	1
Discharge (CC) Charge (CC)	1C until $U < 0.005\,\mathrm{V}$ 1C until $U > 1.5\,\mathrm{V}$	10
Rest	Rest for 1 hour at OCV	1
Discharge (CC) Charge (CC)	2C until $U < 0.005\,\mathrm{V}$ 2C until $U > 1.5\,\mathrm{V}$	10
Rest	Rest for 1 hour at OCV	1
Discharge (CC) Charge (CC)	0.1C until $U < 0.005\,\mathrm{V}$ 0.1C until $U > 1.5\,\mathrm{V}$	5

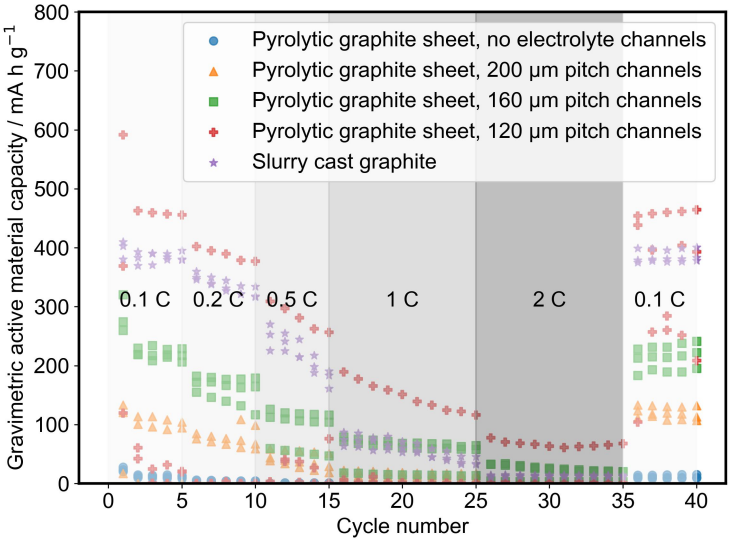


Figure 4.11: Raw data for galvanostatic charge and discharge, normalised to dry electrode mass. Lithiation capacity is shown. Storage of lithium at surface sites, in addition to intercalation of the graphite, can allow an electrode to exceed the theoretical 372 mA h g^{-1} capacity for lithium intercalation into graphite to form LiC_6 [114].

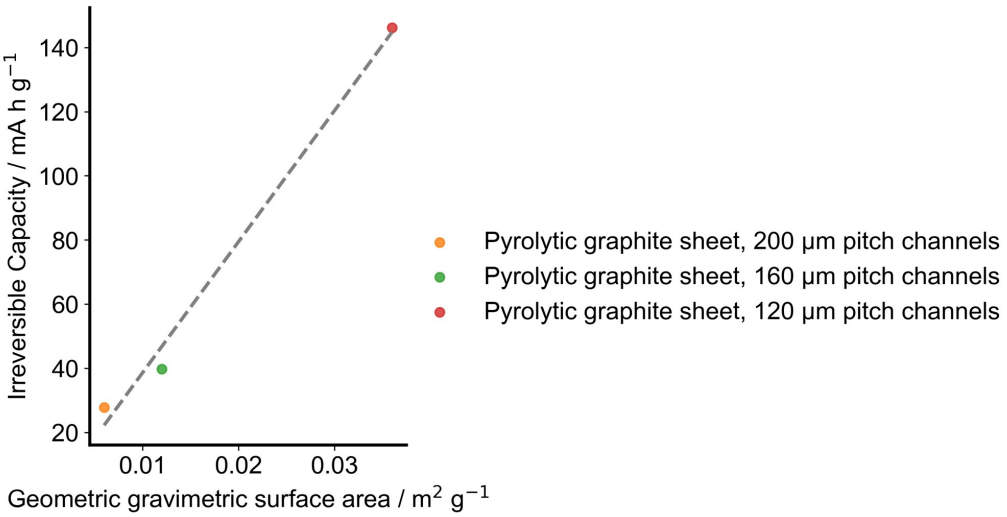


Figure 4.12: Irreversible capacity during first cycle of galvanostatic charge discharge cycling plotted as a function of geometric surface area. The mean irreversible capacity is plotted for each electrode type.

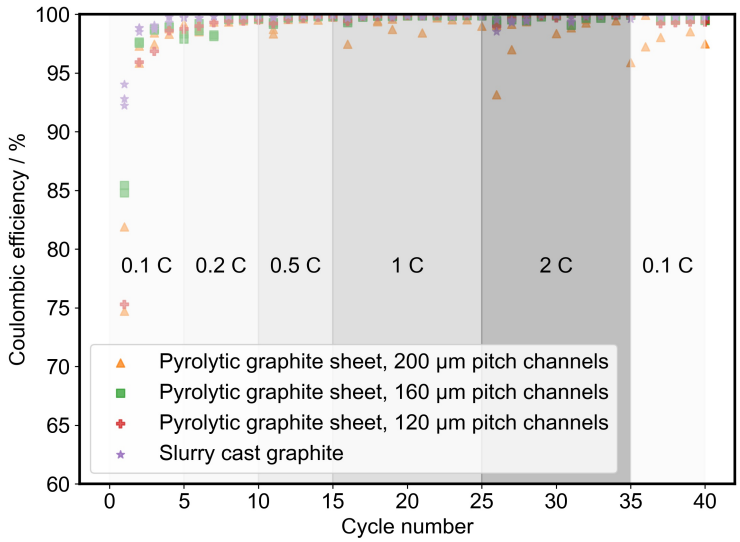


Figure 4.13: Couloumbic efficiency during galvanostatic charge discharge cycling. All electrodes have a coulombic efficiency of greater than 97% after the first cycle. Multiple repeats are shown with cells that showed unstable cycling removed for clarity. One of the 200 µm pitch channel electrodes shows some instability, likely due to imperfect manual cell assembly.

$$\text{Porosity} = 0.9069\frac{d^2}{p^2} \tag{4.4}$$

Calculating gravimetric surface area

For a hexagonal unit cell (pitch, p and thickness, t) with a circular channel at centre (diameter, d) and material density, ρ:

$$\text{Edge-plane surface area} = \pi dt \tag{4.5}$$

$$\text{Basal-plane surface area} = 0.25\pi(\frac{p^2}{0.9069} - d^2) \tag{4.6}$$

$$\text{Volume} = 0.25\pi(\frac{p^2}{0.9069} - d^2)t \tag{4.7}$$

$$\text{Volumetic edge-plane surface area} = \frac{4d}{\frac{p^2}{0.9069} - d^2} = \frac{4}{d(\frac{1}{\text{porosity}} - 1)} \tag{4.8}$$

$$\text{Volumetric basal-plane surface area} = \frac{1}{t} \tag{4.9}$$

These volumetric surface areas can be converted into gravimetric surface areas by dividing by material density, ρ.

Gravimetric surface area of spheres and cylinders

For a sphere with diameter, d and density, ρ:

$$\text{Surface area} = \pi d^2 \tag{4.10}$$

$$\text{Volume} = \frac{\pi d^3}{6} \tag{4.11}$$

$$\text{Volumetric surface area} = \frac{6}{d} \tag{4.12}$$

$$\text{Gravimetric surface area} = \frac{6}{d\rho} \tag{4.13}$$

The gravimetric surface area of a spherical graphite particle with diameter of 11.72 µm is $0.23\,\mathrm{m^2\,g^{-1}}$. There are two things to note. Firstly, for a porous electrode, the surface area of the electrode-electrolyte interface will be lower than the sum of the individual particles as not all particle surface is exposed to electrolyte. Secondly, the surface area of the graphite particle will be a mixture of edge-plane and basal-plane surface. Given the anisotropic nature of lithium diffusion within graphite, the concentration overpotential will be most affected by the edge-plane surface area.

Particularly in the case of graphite, it may be more appropriate to assume non-spherical particle geometry. Discs with a certain diameter and thickness can be assumed. The equations for a disc with diameter, d, thickness, t, and density, ρ, are as follows:

$$\text{Edge-plane surface area} = \pi d t \tag{4.14}$$

$$\text{Basal-plane surface area} = 2 \times \frac{\pi d^2}{4} \tag{4.15}$$

$$\text{Volume} = \frac{\pi d^2}{4} t \tag{4.16}$$

$$\text{Volumetric edge-plane surface area} = \frac{4}{d} \tag{4.17}$$

$$\text{Gravimetric edge-plane surface area} = \frac{4}{d\rho} \tag{4.18}$$

It is interesting to note that the gravimetric edge-plane surface area of a disc is independent of the disc thickness, and simply inversely proportional to the disc diameter. The gravimet-

ric edge-plane surface area of a disc-shaped graphite particle with diameter of 11.72 µm is $0.15\,\mathrm{m^2\,g^{-1}}$.

Chapter 5

Estimating commercial cell performance from laboratory results

Emerging battery chemistries, novel processing techniques and new cell designs are often presented with great excitement in battery literature and mass media. However, the metrics that are used to assess battery performance in the lab can be misleading, especially when comparing to data for commercial cells. Misleading metrics are detrimental to the translation of academic research into better commercial cells [29, 48]. This chapter introduces a methodology and tool for estimating the gravimetric energy density of a commercial cell from laboratory results.

5.1 Normalising to active material mass

The previous chapter demonstrated that, with careful patterning, pyrolytic graphite sheet can achieve high lithiation capacity that could enable its use as a battery electrode. It is however important to reiterate that all lithiation capacities were normalised to active material mass. Normalising to active material mass is convention in the academic literature, and is useful for evaluating the capacity of novel active materials, but is insufficient for drawing any conclusions about potential commercial cell performance [29, 48, 119, 120].

Firstly, normalising to active material mass ignores the binder, conductive additive and current collector. These inactive materials contribute mass and volume, but not capacity, to conventional battery electrodes. As a result, practical electrodes are thicker and heavier

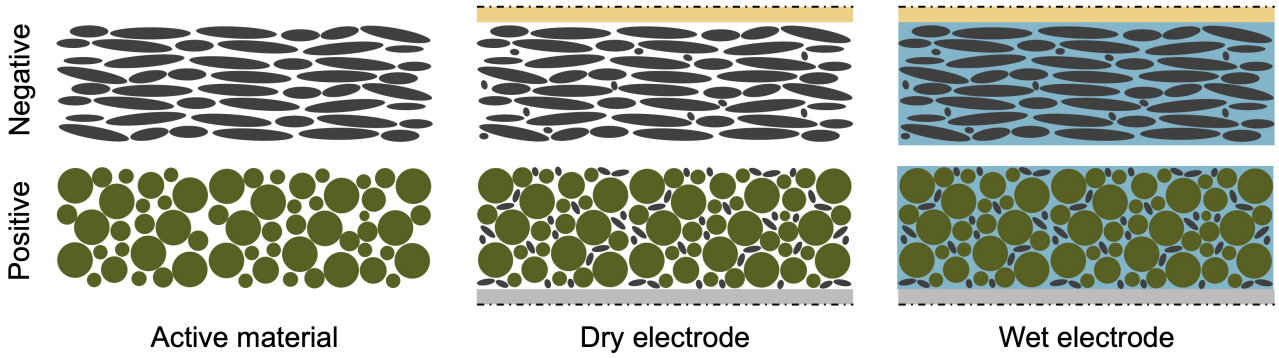


Figure 5.1: Capacity is conventionally normalised to the mass of active material in a single electrode. Normalising to dry electrode mass accounts for the mass of binder, conductive additive and current collector in addition to the active material. Wet electrode mass additionally considers the mass of electrolyte required to fill the void space in the electrode.

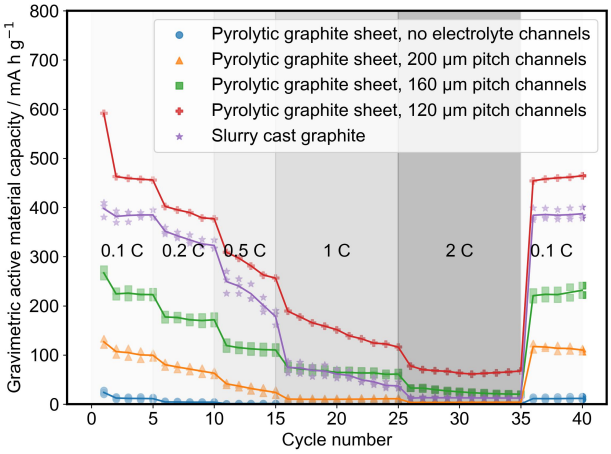
than if they contained active material alone, which adversely affects gravimetric cell energy density. Secondly, the porosity of the electrodes is ignored. Electrodes with high porosity have a significant void volume that will be filled with electrolyte when assembled into a cell. The mass of this electrolyte will be ignored if capacity is normalised to active material mass.

Normalising to dry electrode mass

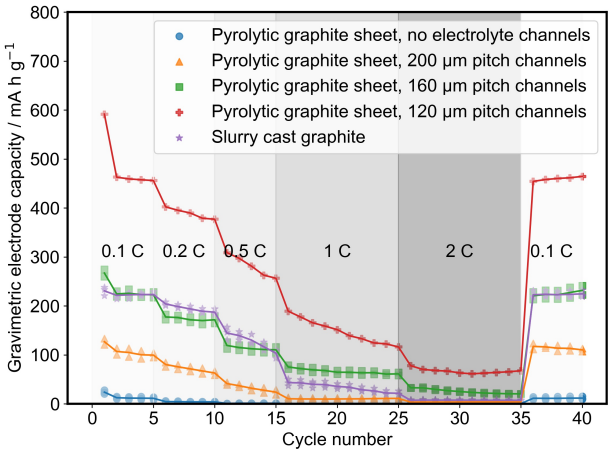
Rather than ignoring these inactive materials, capacity could instead be normalised to dry electrode mass. The dry electrode mass includes any mass of binder, conductive additive and current collector, in addition to the active material mass (Figure 5.1), and was measured prior to cell assembly. For single-sided electrodes with a metal current collector, half of the current collector mass was subtracted as commercial cell electrodes will typically be double-sided. Figure 5.2 shows that the slurry cast electrode is penalised for containing inactive mass when normalising to dry electrode mass. Conversely, the capacities of the pyrolytic graphite sheet electrodes remain unchanged compared to the normalisation using active material mass as they contain no binder, conductive additive, or separate current collector.

Normalising to wet electrode mass

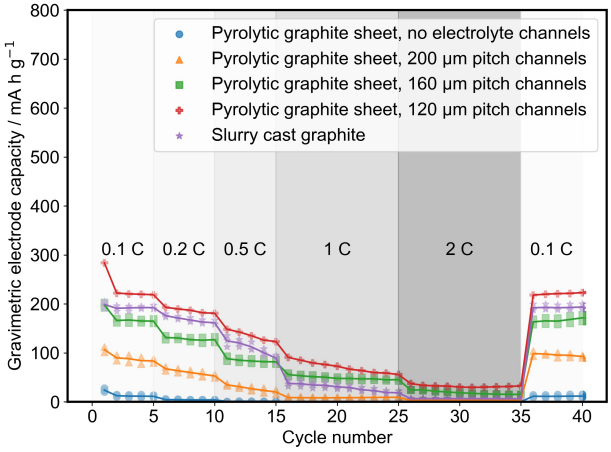
Normalising to dry electrode mass is an improvement, but still ignores electrode porosity. Electrodes with high porosity have a significant void volume that will be filled with electrolyte when assembled into a cell. The mass of this electrolyte will be ignored if capacity is normalised to



(a) Active material mass



(b) Dry electrode mass



(c) Wet electrode mass

Figure 5.2: Galvanostatic cycling between 5 mV and 1.5 V at indicated discharge-charge rates between 0.1C and 2C. Lithiation capacity is normalised to (a) active material mass, (b) dry electrode mass or (c) wet electrode mass. Dry electrode mass includes active material, binder, conductive additive, and current collector where applicable. Wet electrode mass includes electrolyte mass, assuming complete wetting of the electrode porosity, in addition to the dry electrode mass. Line indicates mean capacity for each electrode type.

active material mass or dry electrode mass. Instead, the mass of electrolyte could be accounted for by normalising to wet electrode mass.

Wet electrode mass can be calculated using the thickness and porosity of the electrodes and assuming that all of the void volume is filled with electrolyte (see Methods section for details). Alternatively, it could be possible to measure wet electrode mass experimentally. As shown in Figure 5.2, when normalising to wet electrode mass all of the electrodes are now penalised for including electrolyte. Most significantly, the capacity of the 120 µm pitch electrode, which had a porosity of 63%, falls by a factor of two when normalised to wet instead of dry electrode mass.

Although wet electrode mass is an improvement for normalisation as it accounts for the inactive mass of binder, conductive additive, current collector and electrolyte, it still ignores electrode volume. As the inactive material content or porosity of an electrode is increased, the electrode must be thicker to achieve a given areal capacity. A thicker electrode will reduce the jelly roll area that fits inside a given cell volume and therefore limit gravimetric cell energy density.

In summary, capacity normalised to active material mass is a poor metric for commercial cell design as it ignores the mass and volume of the inactive components required to make a practical cell. Capacity could instead be normalised to dry or wet electrode mass, however these metrics still ignore the impact of inactive electrode volume on gravimetric cell energy density. These metrics also only consider a single electrode in isolation rather than a full cell. The next section will introduce a methodology for normalisation that considers a full, practical cell.

5.2 Estimating gravimetric energy density of a commercial cell

To more accurately evaluate the impact of electrode design on commercial cell performance, we can develop a model to estimate the gravimetric energy density of a practical, commercial cell from laboratory results. By considering how a given electrode design would be integrated into a commercial cell, the impact of both inactive mass and inactive volume is included.

5.2.1 Existing material-to-cell models

There are existing models, used both in industry and academia, to estimate the impact of electrode design on the performance of a commercial cell. Although many of these models are proprietary and developed independently by each company or research group, some open-source models are reported in the literature.

The Battery Performance and Cost (BatPaC) model developed at Argonne is used to estimate the performance and manufacturing cost of commercial lithium-ion batteries [121]. This spreadsheet-based tool designs a cell based on user-provided, pack-level power and energy storage requirements. The BatPaC model has also been adapted for different applications such as solid-state cells [122], an open-source database [123], and life-cycle assessment [124]. Although the scope and level of customisation of the model are attractive to advanced users, they hinder its utility as a simple tool to predict the commercial cell performance of electrodes manufactured in the lab. An additional limitation of the BatPaC model is that it assumes rectangular stiff pouches, therefore limiting its applicability to cylindrical cells such as the LGM50. The "Ragone Calculator" [119], developed by Fraunhofer, offers a simpler translation of material to cell performance. However, a cell utilisation factor is used in place of the actual cell parameters, hindering a direct comparison against manufacturer data sheets. Overall, these models are each useful for different applications, but do not provide a publicly available, simple tool to translate material properties into cell data sheet metrics. This chapter aims to address this gap by developing a straightforward model (requiring only four key inputs) to estimate commercial cell performance from laboratory results.

5.2.2 Model inputs

Laboratories will typically incorporate active material into a battery electrode and measure its capacity in a coin cell against a lithium metal counter electrode. For this model, it is assumed that the gravimetric active material capacity, areal electrode capacity, electrode thickness (without current collector) and average discharge potential have been measured. The electrode is considered to be a composite of active material, binder and conductive additive on a solid current collector. The default parameter values in the model are summarised in Table 5.1.

Table 5.1: The measured and assumed inputs for the normalisation model. It is assumed that the gravimetric active material capacity, areal electrode capacity, electrode thickness (without current collector) and average discharge potential have been measured. The electrode is considered to be a composite of active material, binder and conductive additive on a solid current collector.

Parameter	Negative electrode	Positive electrode
Measured		
Gravimetric active material capacity / $\mathrm{mA\,h\,g^{-1}}$	386	221
Areal electrode capacity / $\mathrm{A\,h\,m^{-2}}$	53.6	48.7*
Electrode composite thickness / µm	85.2	76.0*
Electrode porosity / %	24.9*	33.5
Average discharge potential / V	0.10	3.73
Assumed		
Binder mass percentage in composite / %	2.50	2.50
Conductive additive mass percentage in composite / %	2.50	2.50
Current collector thickness / µm	11.7	16.3
Material densities		
Active material density / $\mathrm{g\,cm^{-3}}$	2.30	4.95
Binder density / $\mathrm{g\,cm^{-3}}$	2.00	2.00
Conductive additive density / $\mathrm{g\,cm^{-3}}$	2.00	2.00
Current collector density / $\mathrm{g\,cm^{-3}}$	8.96	2.70

Parameter	Cell
Assumed	
NP ratio	1.10
Separator thickness / µm	12.0
Seprator porosity / %	47.0
Packing efficiency / %	87.3
Casing internal volume / $\mathrm{cm^3}$	22.2
Casing mass / g	11.4
Material densities	
Separator solid density / $\mathrm{g\,cm^{-3}}$	0.90
Electrolyte density / $\mathrm{g\,cm^{-3}}$	1.28

**Parameter calculated by model.*

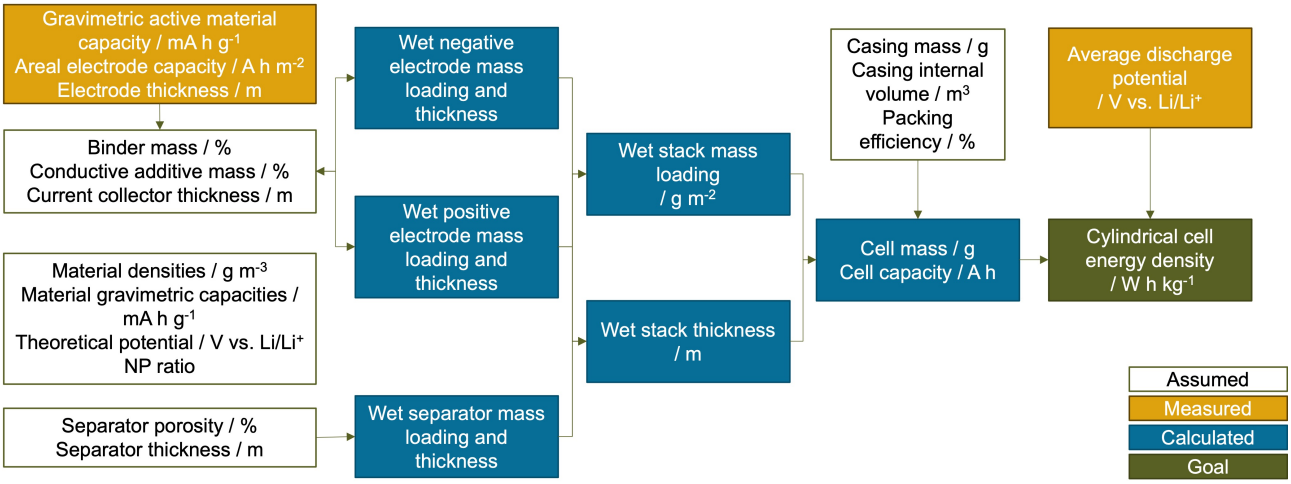


Figure 5.3: Calculation of cylindrical cell energy density from laboratory measurements. It is assumed that the gravimetric active material capacity, areal electrode capacity, electrode thickness (without current collector) and average discharge potential have been measured. Default values are assumed for the remaining parameters. First a wet mass loading and thickness is calculated for each component, and then the stack. The capacity and mass of a cell with that stack is then calculated to ultimately estimate gravimetric cell energy density.

5.2.3 Model calculation

To estimate the gravimetric energy density of a practical cell, the thickness and mass loading of a cell stack that incorporates the electrode of interest must first be calculated (Figure 5.3). A cell stack is made up of two double-sided electrodes (negative and positive) and two separators. Each electrode typically contains a metal current collector and the capacity of the two electrodes is matched to a specified ratio (NP ratio).

If a full cell has been characterised then the gravimetric active material capacity, areal electrode capacity and electrode thickness for both the negative and positive electrodes can be used directly in the model. Alternatively, if a single electrode has been characterised in half cell configuration then the properties of a suitable counter electrode must be calculated. First the areal capacity of the counter electrode is calculated using an assumed NP ratio of 1.1. The thickness of the counter electrode is then calculated by assuming values for gravimetric active material capacity, counter electrode porosity and the mass percentage of binder and conductive additive in the counter electrode.

For each electrode, the wet mass loading is calculated by assuming that all porosity is filled with electrolyte. First, the mass loading of active material is calculated using the gravimet-

ric active material capacity and areal electrode capacity. The mass percentage of binder and conductive additive in the composite is then used to calculate the composite mass loading. The composite volume loading is calculated using the material densities and compared to the measured composite thickness to calculate porosity. Alternatively, in the case that an electrode porosity rather than thickness is specified, the electrode thickness is calculated using the composite volume loading and porosity. Finally, the wet mass loading is calculated by summing up the active material, binder, conductive additive, electrolyte and current collector mass loadings.

Using the stack thickness, the stack area that fits inside a specified internal volume of a cell casing is calculated. A packing efficiency is assumed when performing this calculation. Any volume not filled by the stack is assumed, for simplicity, to have an average density equivalent to the electrolyte and the corresponding mass is reported as "Excess mass". The casing mass, stack mass loading and stack areal capacity are finally used to calculate the cell mass and capacity, and ultimately the gravimetric energy density. Full calculation details are provided in the Methods section.

The model was validated using the LGM50 parametrisation data [51]. For the inputs reported in Table 5.1, the model calculates a gravimetric cell energy density of $264\,\mathrm{W\,h\,kg^{-1}}$. This value shows good agreement with the gravimetric energy density measured by Batemo [3] and the thicknesses of the calculated counter electrode components are consistent with the parametrisation data [51] used in Chapter 3.

5.2.4 Model deployment

Working in collaboration with the TLDR research group [125], the model is deployed as a web app to help other researchers contextualise their research (Figure 5.4). The user provides four inputs for each electrode to the web app: gravimetric active material capacity, areal electrode capacity, electrode thickness (without current collector) and average discharge potential. From these inputs, the gravimetric energy density of a 18650 or 21700 cell is calculated using the parameter set in Table 5.1. A future version of the web app could support alternative chemistries and cell designs by allowing the user to edit this parameter set. A standardised comparison of novel electrode designs using cell-level metrics could also be facilitated by supporting user



Figure 5.4: The model is deployed as a web app to help other researchers contextualise their research. The user provides four inputs for each electrode: gravimetric active material capacity, areal electrode capacity, electrode thickness (without current collector) and average discharge potential. From these inputs, the gravimetric energy density of a 18650 or 21700 cell is calculated using the parameter set in Table 5.1.

submission to a database at time of publication.

5.3 Using the model

The manufactured pyrolytic graphite sheet electrodes

The model can be used to estimate the gravimetric cell energy density of a commercial cell that uses the pyrolytic graphite sheet electrodes reported in Chapter 4. Three pyrolytic graphite sheet electrode designs were manufactured, all with hexagonal arrays of 100 µm diameter channels, but differing pitches as indicated in the electrode labels (PGS200 = 200 µm pitch, PGS160 = 160 µm pitch, PGS120 = 120 µm pitch). First, the model was run for the exact electrode designs that were manufactured and tested. Each manufactured electrode had a thickness of 25 µm and the thickness of the counter electrode was therefore adjusted by the model to match the areal capacity of the pyrolytic graphite sheet electrode (Figure 5.5).

It is clear in Figure 5.5 that the areal capacities of the pyrolytic graphite sheet electrodes reported in Chapter 4 were between 7 and 14 times lower than the LGM50 negative electrode

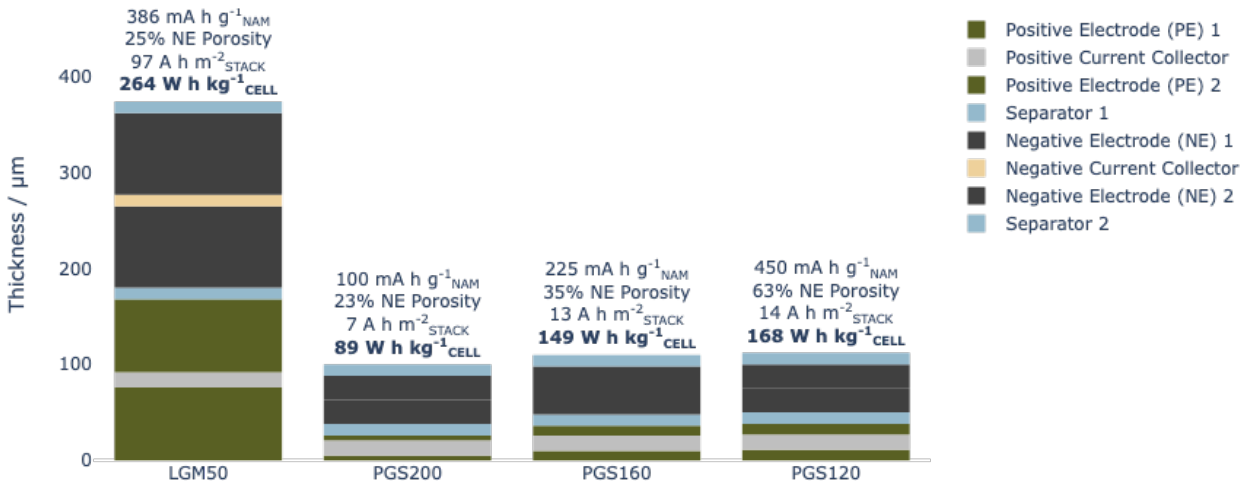


Figure 5.5: Full cell stacks based on 25 µm thickness pyrolytic graphite sheet electrodes. The areal capacities of the pyrolytic graphite sheet electrodes reported in Chapter 4 were between 7 and 14 times lower than the LGM50 negative electrode at a discharge rate of 0.1C. As a result of these lower areal capacities, the model reduces the thickness of the counter electrode to ensure that the electrodes stay balanced. As areal electrode capacity is reduced, a lower proportion of the cell mass and volume is made up of active materials and the cell gravimetric energy density decreases to 89 W h kg^{-1}.

at a discharge rate of 0.1C. As a result of these lower areal capacities, the model reduces the thickness of the counter electrode to ensure that the electrodes stay balanced. For the pyrolytic graphite sheet electrode with 200 µm pitch channels, the thickness of the counter electrode is reduced to the extent that the 16 µm positive current collector is thicker than the positive electrode composite (10 µm). As areal electrode capacity is reduced, a lower proportion of the cell mass and volume is made up of active materials and the cell gravimetric energy density decreases to 89 $W\,h\,kg^{-1}$.

Figure 5.5 also highlights that gravimetric active material capacity is not a good indicator of gravimetric cell energy density. The PGS120 cell (450 $mA\,h\,g^{-1}$) has a higher gravimetric negative active material capacity than the LGM50 cell (386 $mA\,h\,g^{-1}$) but much lower gravimetric cell energy density (168 $W\,h\,kg^{-1}$ compared to 264 $W\,h\,kg^{-1}$). The PGS120 electrode has low areal capacity and high porosity compared to the LGM50 electrode, leading to a high inactive material content in the stack.

Figure 5.6 shows the mass and volume breakdown of the different cells. The solid mass of the casing is the largest inactive mass for all the cell designs. The negative current collector mass is the next largest inactive mass in the LGM50 cell, but reduced to zero for the pyrolytic graphite sheet electrodes as no separate metal current collector is used. Compared to the LGM50 cell, the positive current collector represents a much larger proportion of cell mass for the pyrolytic graphite sheet cells due to the low areal capacity. As porosity of the negative electrodes increases, the mass and volume of electrolyte also increases. The electrolyte in the negative electrode is the third largest source of inactive mass in the PGS120 cell, after the casing and positive current collector.

In summary, the pyrolytic graphite sheet electrodes in Chapter 4 all had a thickness of 25 µm. This thickness of pyrolytic graphite sheet was chosen as it is available commercially and sufficient for investigating the introduction of electrolyte channels. However, as shown in Figure 5.5, thin electrodes lead to low areal capacity and poor gravimetric energy density. To achieve higher gravimetric energy density, the areal capacity of the electrodes must be increased.

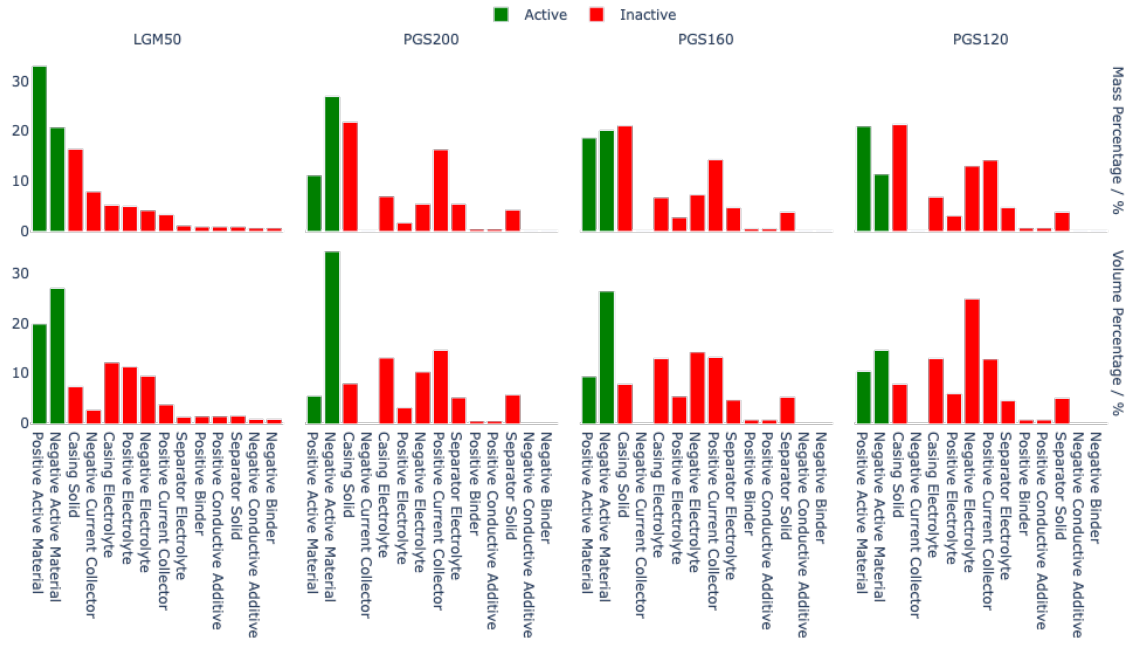


Figure 5.6: Mass and volume breakdown for LGM50 cell using 25 µm thickness pyrolytic graphite sheet electrodes. The solid mass of the casing is the largest inactive mass for all the cell designs. The negative current collector mass is the next largest inactive mass in the LGM50 cell, but reduced to zero for the pyrolytic graphite sheet electrodes as no separate metal current collector is used. Compared to the LGM50 cell, the positive current collector represents a much larger proportion of cell mass for the pyrolytic graphite sheet cells.

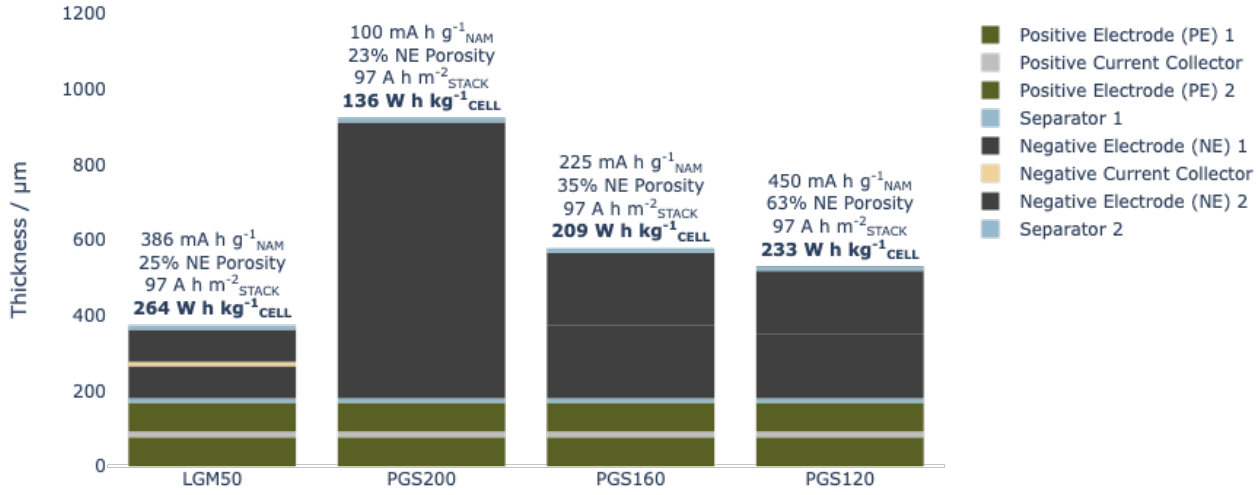


Figure 5.7: Model results with areal capacity of the pyrolytic graphite sheet cells matched to the LGM50 cell. The PGS200 electrode has similar porosity to the LGM50 electrode but much lower gravimetric active material capacity ($100\,\mathrm{mA\,h\,g^{-1}}$ compared to $386\,\mathrm{mA\,h\,g^{-1}}$). As a result of this lower gravimetric active material capacity, the PGS200 electrode is almost 4 times thicker and the thickness of the full stack is over double that of the LGM50 cell. A thicker stack with equivalent areal capacity results in lower gravimetric cell energy density.

Thicker pyrolytic graphite sheet electrodes to match LGM50 areal capacity

Rather than taking the exact electrodes manufactured in Chapter 4, thicker electrodes with the same areal capacity as the LGM50 electrodes can be considered. For a conventional slurry cast electrode, it would be difficult to do this analysis as the gravimetric active material capacity is a strong function of electrode thickness. This dependency is largely due to the high tortuosity of the electrolyte domain within the electrodes and poor electronic conductivity through the electrode thickness [59]. Conversely, due to the low tortuosity of the pyrolytic graphite sheet electrodes with electrolyte channels, the gravimetric active material capacity is expected to be minimally affected by thickness in the range of typical areal capacities and discharge rates. Without a separate current collector, electron conduction will also primarily be in-plane for the pyrolytic graphite sheet, again minimising the effect of thickness on gravimetric active material capacity.

Figure 5.7 shows the thickness of the pyrolytic graphite sheet electrodes required to match the areal capacity of the LGM50 cell. The PGS200 electrode has similar porosity to the

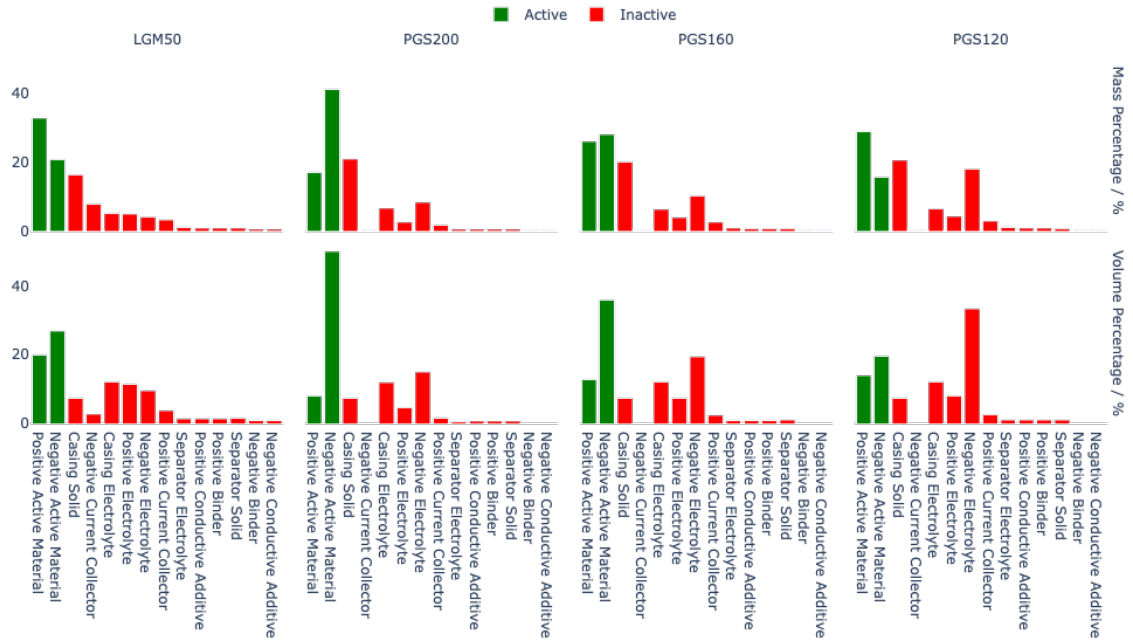


Figure 5.8: Mass and volume breakdown for LGM50 cell using pyrolytic graphite sheet electrodes with matched areal capacity. The negative electrolyte accounts for 18% of PGS120 cell mass and 33% of cell volume.

LGM50 electrode but much lower gravimetric active material capacity ($100\,\mathrm{mA\,h\,g^{-1}}$ compared to $386\,\mathrm{mA\,h\,g^{-1}}$). As a result of this lower gravimetric active material capacity, the pyrolytic graphite sheet electrode is almost 4 times thicker and the thickness of the full stack is over double that of the LGM50 cell. A thicker stack with equivalent areal capacity results in lower gravimetric cell energy density.

The other pyrolytic graphite sheet electrodes have higher gravimetric active material capacity but also higher porosity. As porosity increases, the electrodes must be thicker to achieve a given areal capacity. This point is illustrated by the PGS120 negative electrodes which are more than twice the thickness of the LGM50 negative electrodes despite having a higher gravimetric active material capacity. A thicker stack reduces the stack area that fits inside the internal volume of the cell casing and limits gravimetric cell energy density.

It is important to note that, despite a high negative electrode porosity of 63%, the PGS120 cell has a gravimetric energy density of $233\,\mathrm{W\,h\,kg^{-1}}$. Although below the gravimetric energy density of the LGM50 cell, the negative electrolyte accounts for 18% of PGS120 cell mass and 33% of PGS120 cell volume (Figure 5.8). If a pyrolytic graphite sheet electrode could be

designed to achieve the same gravimetric active material capacity at a lower porosity, then pyrolytic graphite sheet electrodes could enable the LGM50 gravimetric cell energy density to be surpassed.

5.4 Conclusions

Gravimetric active material capacity or areal electrode capacity are conventionally reported for novel electrode designs, however these metrics are insufficient for evaluating the potential benefits to commercial cell performance. Capacity could instead be normalised to dry or wet electrode mass to account for the mass of inactive materials, however these metrics still ignore the impact of inactive volume.

This chapter introduces a model for estimating the gravimetric energy density of a commercial cell from laboratory metrics. Four key inputs to the model are required to specify an electrode: gravimetric active material capacity, areal electrode capacity, electrode thickness, and average discharge potential. In the case that only one electrode is specified, the model pairs the electrode of interest with a balanced counter electrode to calculate the mass loading and thickness of practical cell stack. This cell stack is then fitted into a commercial cell casing to evaluate gravimetric cell energy density.

Following validation with LGM50 cell data, the model was used to evaluate the potential benefits of using pyrolytic graphite sheet electrodes in a commercial cell. Results show that although the electrodes manufactured in Chapter 4 have comparable gravimetric active material capacity to slurry cast electrodes, the gravimetric energy density of a commercial cell using these electrodes would be significantly lower at a discharge rate of 0.1C due to low areal capacity and high porosity.

The model was re-run for the pyrolytic graphite sheet electrodes, but with the thickness in each case increased to match the areal capacity of the LGM50 slurry cast negative electrode. The results showed that the pyrolytic graphite sheet electrodes must be significantly thicker than the slurry cast electrodes due to either lower gravimetric active material capacity or higher porosity. The pyrolytic graphite sheet electrode with 120 µm pitch channels has an estimated gravimetric cell energy density of $233\,\mathrm{W\,h\,kg^{-1}}$ at a discharge rate of 0.1C.

It is important to note that the results presented in this chapter use the LGM50 cell as a reference. The parameter set presented in Table 5.1 was used for all analysis of pyrolytic graphite sheet electrodes. These parameters assume that all components except the specified electrode have the same properties as an LGM50 cell. For instance, the separator thickness and mass of casing are the same as an LGM50 cell. Additionally, the counter electrode is assumed to have the same composition and gravimetric active material capacity as the positive LGM50 electrode. By challenging and changing these parameter values, it may be possible to optimise the gravimetric energy density of a cell that uses pyrolytic graphite sheet electrodes, particularly as different discharge rates are considered.

Overall, the results in this chapter highlight the importance of using the right metrics when designing a battery electrode. Gravimetric active material capacity is a poor indicator of gravimetric energy density in a practical cell format. Although the best-performing pyrolytic graphite sheet cell has a gravimetric energy density at a discharge rate of 0.1C which is below the LGM50 benchmark ($233\,\mathrm{W\,h\,kg^{-1}}$ compared to $263\,\mathrm{W\,h\,kg^{-1}}$), it achieves this performance despite a negative electrode porosity of 63%. Alternative electrode designs could enable similar gravimetric active material capacity at lower porosity, and therefore higher gravimetric cell energy density. The next chapter will investigate the design of a practical pyrolytic graphite sheet electrode.

5.5 Methods

Normalising to wet electrode mass

Wet electrode mass can be calculated using the thickness and porosity of the electrodes and assuming that all of the void volume is filled with electrolyte.

$$\text{Electrolyte volume} = \text{Porosity} \times \text{Slurry thickness} \times \text{Area} \tag{5.1}$$

$$\text{Electrolyte mass} = \text{Electrolyte density} \times \text{Electrolyte volume} \tag{5.2}$$

$$\text{Wet electrode mass} = \text{Dry electrode mass} + \text{Electrolyte mass} \tag{5.3}$$

In the case that porosity is not known, it can be calculated using the electrode composition (mass percentages of components in the electrode composite). First, the mass loadings and volume loadings of the individual components (e.g. active material, binder, conductive additive) are calculated:

$$\text{Component mass loading} = \text{Dry slurry mass loading} \times \text{Component mass percentage} \tag{5.4}$$

$$\text{Component volume loading} = \frac{\text{Component mass loading}}{\text{Component density}} \tag{5.5}$$

Porosity is then calculated by summing the component volume loadings and dividing by the measured electrode thickness:

$$\text{Porosity} = \frac{\text{Total volume loading of components}}{\text{Measured electrode thickness}} \tag{5.6}$$

Model calculation

Mass loadings

First, with the capacity and area of the single-sided electrode of interest known, the areal double-sided electrode capacity is calculated:

$$\text{Areal capacity} = 2 \times \frac{\text{Capacity}}{\text{Area}} \tag{5.7}$$

In the case that only one electrode has been characterised, the electrode of interest must now be paired with a suitable counter electrode. Crucially, the areal capacity of the negative and positive electrodes must be balanced according to a specified ratio. For instance, the electrodes are balanced in the LGM50 cell with an NP ratio of 1.1, such that the negative electrode areal capacity exceeds the positive electrode areal capacity by 10% [51].

The areal capacity of the counter electrode is calculated:

$$\text{Negative areal capacity} = \text{NP ratio} \times \text{Positive areal capacity} \tag{5.8}$$

To calculate the mass and thickness of the counter electrode, a gravimetric active material capacity, electrode porosity and electrode composition are assumed.

The mass loading of active material is calculated:

$$\text{Active material mass loading} = \frac{\text{Areal capacity}}{\text{Gravimetric active material capacity}} \tag{5.9}$$

The mass loading of the composite is calculated by dividing the active material mass loading by the mass percentage of active material in the slurry:

$$\text{Slurry mass loading} = \frac{\text{Active material mass loading}}{\text{Active material mass percentage in slurry}} \tag{5.10}$$

The mass loadings of the inactive components are similarly calculated as the product of their mass percentage in the slurry and the slurry mass loading.

A thickness and density of a current collector are assumed, allowing the mass loading of the current collector to be calculated:

$$\text{Current collector mass loading} = \text{Thickness} \times \text{Density} \tag{5.11}$$

Similarly for the separator:

$$\text{Separator mass loading} = \text{Thickness} \times \text{Solid density} \times (1 - \text{Porosity}) \tag{5.12}$$

The dry stack mass loading is calculated by summing up the mass loadings of the negative slurry, negative current collector, positive slurry, positive current collector, and 2 separators.

Solid volume loadings

The solid volume loading of each stack component is calculated by dividing the component mass loading by the component density:

$$\text{Volume loading} = \frac{\text{Mass loading}}{\text{Density}} \tag{5.13}$$

By comparing the solid volume loading and thickness of components, the porosity of each component is calculated:

$$\text{Porosity} = \frac{\text{Thickness} - \text{Solid volume loading}}{\text{Thickness}} \tag{5.14}$$

Alternatively, a porosity can be assumed and the thickness calculated by rearranging equation 5.14.

The thickness of the stack is calculated by summing up the thickness of the negative slurry, negative current collector, positive slurry, positive current collector, and 2 separators.

Electrolyte loadings

Making the assumption that all porosity is filled with electrolyte, the volume and mass loading of electrolyte inside each component can be calculated:

$$\text{Electrolyte volume loading} = \text{Porosity} \times \text{Thickness} \tag{5.15}$$

$$\text{Electrolyte mass loading} = \text{Electrolyte volume loading} \times \text{Density} \tag{5.16}$$

The wet stack mass loading is calculated by summing up the solid and electrolyte loadings of the negative slurry, negative current collector, positive slurry, positive current collector, and 2 separators.

Calculate gravimetric cell energy density

For a specified stack thickness, mass loading, and areal capacity, gravimetric energy density for a given cell format can be calculated.

First the stack (or jelly roll in the case of a cylindrical cell format) area that fits within the case internal volume is calculated:

$$\text{Stack area} = \frac{\text{Packing efficiency} \times \text{Case internal volume}}{\text{Stack thickness}} \tag{5.17}$$

where the packing efficiency accounts for a difference between the stack volume and case internal volume. By assuming that any internal cell volume that is not filled with the stack is filled with electrolyte, an excess mass can be calculated:

$$\text{Excess mass} = (1 - \text{Packing efficiency}) \times \text{Casing internal volume} \times \text{Electrolyte density} \tag{5.18}$$

Cell energy is calculated:

$$\text{Cell energy} = \text{Positive areal capacity} \times \text{Stack area} \tag{5.19}$$

Note, it is the areal capacity of the positive electrode that is used as NP ratios are typically greater than 1 (the capacity of the positive electrode is lower than the negative electrode by design).

Stack mass is calculated:

$$\text{Stack mass} = \text{Wet stack mass loading} \times \text{Stack area} \tag{5.20}$$

Cell mass is calculated:

$$\text{Cell mass} = \text{Stack mass} + \text{Casing mass} + \text{Excess mass} \tag{5.21}$$

Finally, gravimetric cell capacity and energy density is calculated:

$$\text{Gravimetric cell capacity} = \frac{\text{Cell capacity}}{\text{Cell mass}} \tag{5.22}$$

$$\text{Gravimetric cell energy density} = \text{Gravimetric cell capacity} \times \text{Average discharge voltage} \tag{5.23}$$

In the case of half cell measurements, the average discharge voltage is calculated by subtracting the average negative discharge potential from the average positive discharge potential.

Chapter 6

Design of a low inactive mass, low overpotential battery electrode

Previous chapters have shown that, following the introduction of electrolyte channels, the lithiation capacity of pyrolytic graphite sheet increases such that it could be used as an active material in a lithium-ion battery. However, although the manufactured electrodes were sufficient for measuring gravimetric active material capacity, they would perform poorly in a commercial cell due to low areal capacity and high porosity (Chapter 5). This chapter will investigate the design of a practical pyrolytic graphite sheet electrode through simulation.

First, the normalisation model developed in Chapter 5 will be used to explore the impact of pyrolytic graphite sheet porosity and gravimetric active material capacity on gravimetric cell energy density. Second, a physics-based model will be developed to estimate the gravimetric active material capacity of pyrolytic graphite sheet with a hexagonal array of electrolyte channels. Finally, the normalisation and physics-based models will be combined to optimise the design of a practical pyrolytic graphite sheet electrode.

6.1 Assuming complete lithiation

To begin, we will calculate the gravimetric energy density of an LGM50 cell for which the slurry cast negative electrode has been removed and replaced with non-porous pyrolytic graphite sheet of equivalent areal capacity (Figure 6.1). Chapter 4 showed that porosity of the pyrolytic

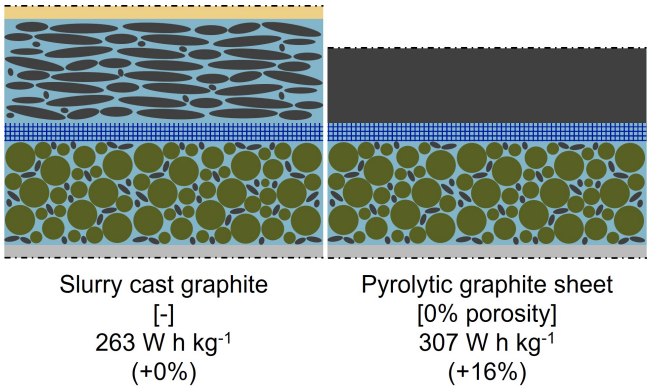


Figure 6.1: Schematic showing the effect on stack thickness and gravimetric energy density (quoted in $\mathrm{W\,h\,kg^{-1}}$) of replacing the negative electrode of a LGM50 cell with non-porous pyrolytic graphite sheet. The new theoretical stack delivers the same areal capacity, but is both thinner (343 µm) and lighter ($886\,\mathrm{g\,m^{-2}}$). These changes translate into a gravimetric cell energy density of $307\,\mathrm{W\,h\,kg^{-1}}$, which is a 16% improvement compared to the original LGM50 cell.

graphite sheet must be increased to enable its use as a battery electrode, but, to calculate the maximum theoretical improvement, we will first consider the as-manufactured, non-porous pyrolytic graphite sheet. This maximum theoretical improvement will be a useful reference as different electrode designs are considered in this chapter.

6.1.1 A non-porous pyrolytic graphite sheet electrode

The LGM50 slurry cast negative electrode must be replaced with a pyrolytic graphite sheet electrode of equivalent areal capacity. Parametrisation data [51] shows us that the areal capacity of the LGM50 stack was $9.74\,\mathrm{mA\,h\,cm^{-2}}$ and the electrodes were balanced with a NP ratio of 1.1. The areal capacity of the existing double-sided negative electrode is therefore $10.7\,\mathrm{mA\,h\,cm^{-2}}$. To evaluate the use of pyrolytic graphite sheet as the negative electrode in the LGM50 stack, we must determine the thickness of pyrolytic graphite sheet required to provide the same $10.7\,\mathrm{mA\,h\,cm^{-2}}$ of areal capacity.

The areal capacity of the pyrolytic graphite sheet depends on its theoretical capacity, density and thickness. If we assume a theoretical gravimetric capacity of $372\,\mathrm{mA\,h\,g^{-1}}$ and a density of $1.9\,\mathrm{g\,cm^{-3}}$ then the volumetric capacity of pyrolytic graphite sheet is calculated as $707\,\mathrm{mA\,h\,cm^{-3}}$. The thickness of a pyrolytic graphite sheet electrode with areal capacity of $10.7\,\mathrm{mA\,h\,cm^{-2}}$ can then be calculated as 152 µm.

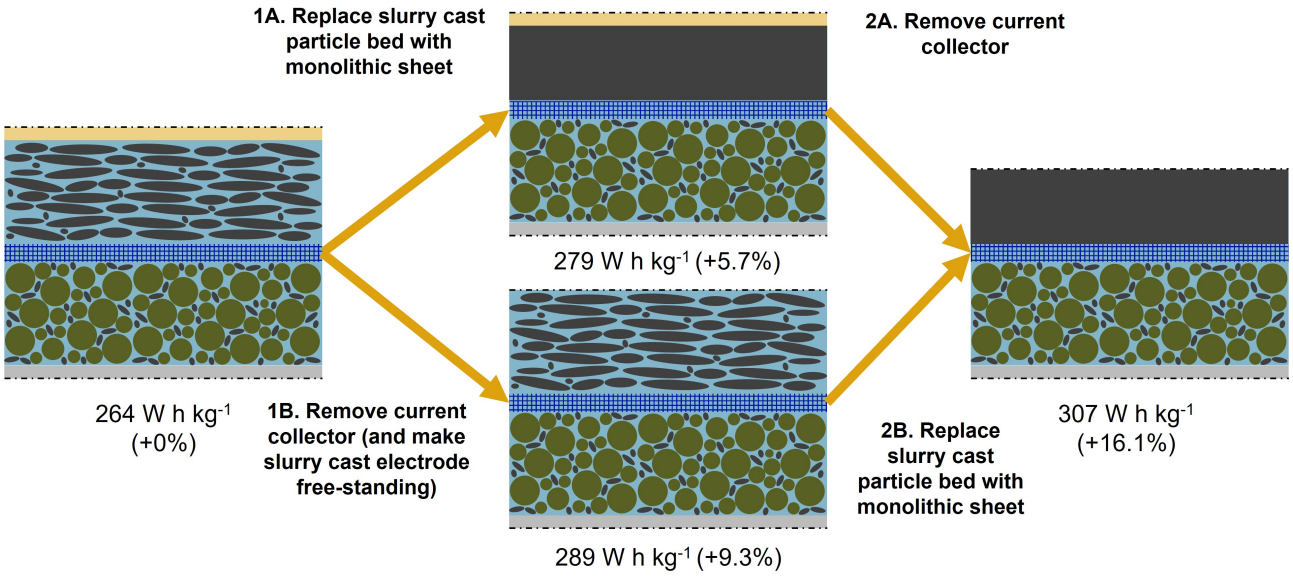


Figure 6.2: Schematic showing the effect on gravimetric energy density of replacing the negative electrode of a LGM50 cell with pyrolytic graphite sheet in 2 steps. Considering these two steps individually shows that most (roughly 60%) of the theoretical improvement to gravimetric energy density of using pyrolytic graphite sheet is derived from the removal of the conventional copper current collector. The remaining benefit is derived from replacing the slurry cast particle bed with a monolithic graphite sheet.

Figure 6.1 shows a schematic of the original LGM50 stack alongside the new theoretical stack with non-porous pyrolytic graphite sheet as the negative electrode. Pyrolytic graphite sheet is both freestanding and has high electrical and thermal conductivity, which should allow the conventional copper current collector to be eliminated. The new theoretical stack delivers the same areal capacity, but is both thinner (343 µm) and lighter (886 g cm^{-2}). These changes translate into a gravimetric cell energy of 307 W h kg^{-1}, which is a 16% improvement compared to the original LGM50 cell.

Figure 6.2 shows the replacement of the LGM50 electrode in 2 steps: removal of the negative current collector and replacement of the slurry cast electrode with pyrolytic graphite sheet. Considering these two steps individually shows that most (roughly 60%) of the theoretical improvement to gravimetric energy density of using pyrolytic graphite sheet is derived from the removal of the conventional copper current collector. The remaining benefit is derived from replacing the slurry cast particle bed with a monolithic graphite sheet.

It is however important to remember that this value is a maximum theoretical improvement. We made a key assumption in the calculation that the theoretical gravimetric active material

capacity of the pyrolytic graphite sheet ($372\,\mathrm{mA\,h\,g^{-1}}$) will be achieved. Unfortunately, as shown in Chapter 4, this assumption is invalid given the low porosity of pyrolytic graphite sheet which results in high overpotentials.

Why does the as-received pyrolytic graphite sheet have high overpotentials?

Although the layered, anisotropic structure of pyrolytic graphite sheet (Figure 4.2) enables high in-plane thermal and electronic conductivity, it also greatly restricts the surface area of the interface between active material and electrolyte. Firstly, pyrolytic graphite sheet is impermeable to electrolyte. With electrolyte only able to access the top surface there will be no electrolyte domain within the electrode as for a conventional particle based electrode. Secondly, intercalation of graphite largely occurs at edge sites, but with the graphite sheets aligned parallel to the top surface, only a low number of edge sites will be exposed to electrolyte. Together, these factors severely restrict the surface area over which lithium ions are able to enter graphite from the electrolyte.

Restricting the surface area of the interface between active material and electrolyte leads to significant overpotentials. Batteries are typically discharged at a fixed gravimetric current density. Under these conditions, if the surface area of this interface is reduced for a fixed electrode mass then the areal current density will increase. Firstly, kinetic overpotentials will increase with areal current density (as described by the Butler-Volmer equation). Secondly, the current at the active material-electrolyte interface is carried by lithium ions, so the areal lithium ion flux will also increase at a specified gravimetric current density. This increased flux will lead to steeper concentration gradients in the active material and electrolyte, and a higher concentration overpotential. Lastly, the increased areal current density could also lead to local depletion or accumulation of lithium ions in the electrolyte and an increased electrolyte overpotential.

6.1.2 A porous pyrolytic graphite sheet electrode

Chapter 4 showed that increasing the porosity of pyrolytic graphite sheet reduces overpotentials and increases its gravimetric active material capacity. There is however a trade-off when

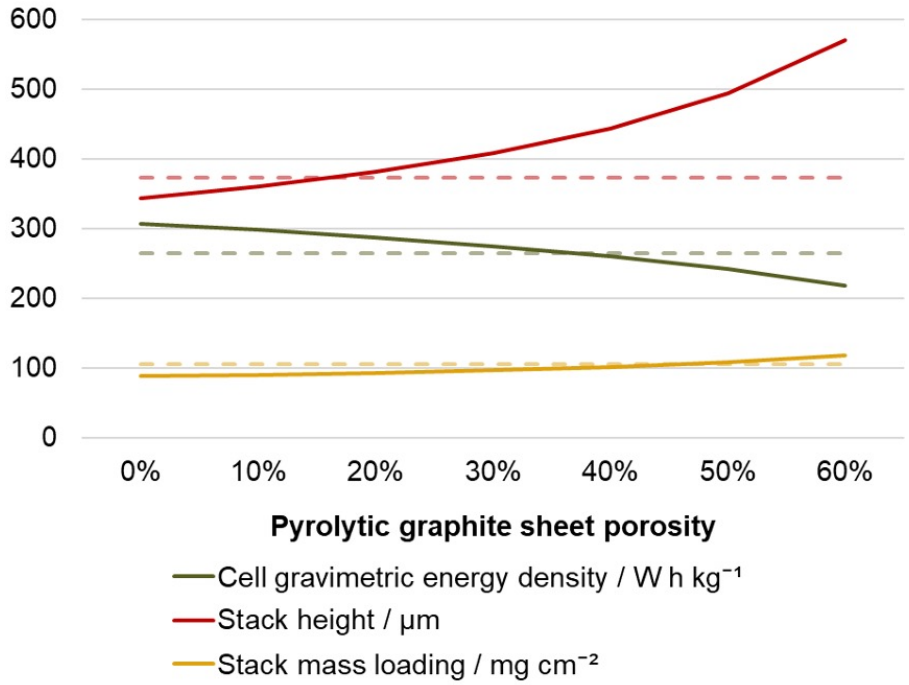


Figure 6.3: Gravimetric energy density as function of pyrolytic graphite sheet (PGS) porosity. This analysis assumes a gravimetric active material capacity of 372 mA h g^{-1} and areal capacity of 9.74 mA h cm^{-2}. As porosity is increased, a stack with equivalent areal capacity will be both thicker and heavier, reducing gravimetric cell energy density. The dashed lines represent the commercial LGM50 stack with slurry cast electrodes.

increasing porosity between overpotentials and inactive material content. To better understand this trade-off, we can repeat the calculations from the previous section, again assuming negligible overpotentials, but this time consider a pyrolytic graphite sheet with increased porosity. As porosity of the pyrolytic graphite sheet is increased, its theoretical areal capacity will decrease and a thicker pyrolytic graphite sheet will be required to keep the electrodes balanced. The additional volume will be filled with electrolyte which adds inactive mass to the stack. In summary, as porosity is increased, a stack with equivalent areal capacity will be both thicker and heavier, reducing gravimetric cell energy density (Figure 6.3).

Figure 6.4 shows the impact on gravimetric cell energy density as the pyrolytic graphite sheet porosity is increased. As expected, even if gravimetric active material capacity remains constant, gravimetric cell energy density decreases as pyrolytic graphite sheet porosity is increased. At a porosity of 38%, the gravimetric cell energy density is estimated as 264 W h kg^{-1}, equivalent to the original LGM50 cell. At lower values of porosity, the stack is thinner and there is less electrolyte in the negative electrode, leading to increased gravimetric energy den-

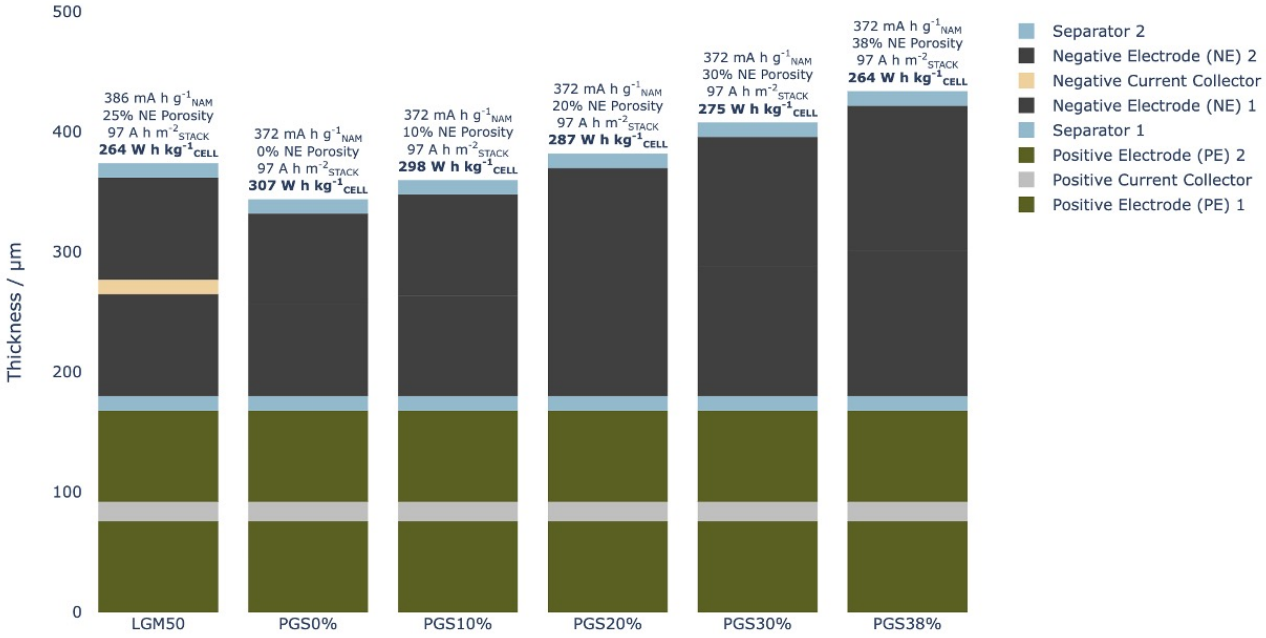


Figure 6.4: Gravimetric energy density as function of pyrolytic graphite sheet porosity. If gravimetric active material capacity remains constant, gravimetric cell energy density decreases as pyrolytic graphite sheet porosity is increased. At a porosity of 38%, the gravimetric cell energy density is estimated as $264\,\mathrm{W\,h\,kg^{-1}}$, equivalent to the original LGM50 cell. At lower values of porosity, the stack is thinner and there is less electrolyte in the negative electrode, leading to increased gravimetric energy density. It is promising to see that if an electrode with gravimetric active material capacity of $372\,\mathrm{mA\,h\,g^{-1}}$ and porosity of 20% could be manufactured, a 9% improvement to gravimetric cell energy density (to $287\,\mathrm{W\,h\,kg^{-1}}$) would be expected over the original LGM50 cell.

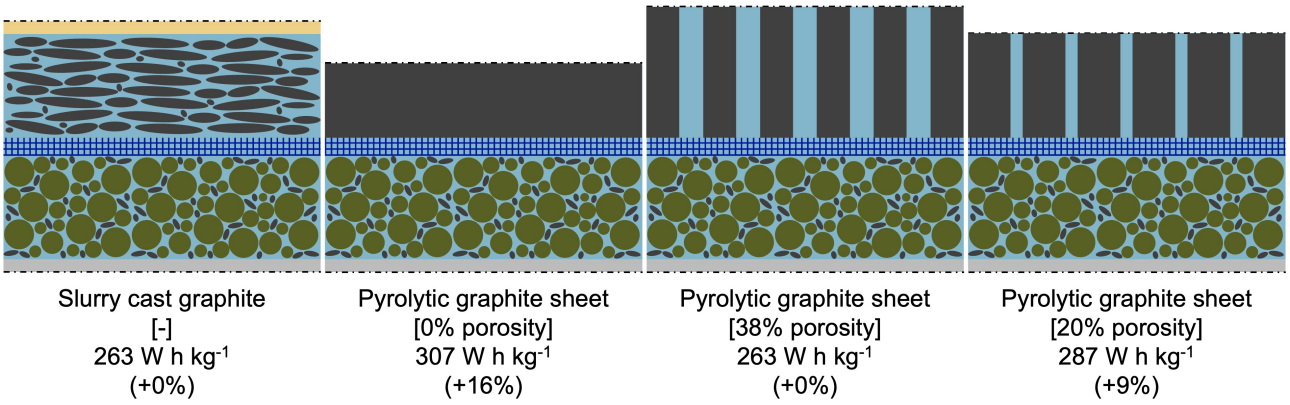


Figure 6.5: A schematic of the different stacks and associated gravimetric energy densities. Replacing the slurry cast graphite electrode with the as-manufactured, non-porous pyrolytic graphite would result in a 16% maximum theoretical improvement in gravimetric cell energy density. However, this maximum improvement assumes a gravimetric active material capacity of 372 mA h g^{-1}. Introducing porosity could reduce overpotentials, but will also increase inactive material content. Calculations show that up to 38% porosity could be introduced into pyrolytic graphite sheet before the benefit to gravimetric energy density is lost. A pyrolytic graphite sheet with 20% porosity would improve theoretical gravimetric energy density by 9%, but again only if a gravimetric active material capacity of 372 mA h g^{-1} is realised.

sity. It is promising to see that if an electrode with gravimetric active material capacity of 372 mA h g^{-1} and porosity of 20% could be manufactured, a 9% improvement to gravimetric cell energy density (to 287 W h kg^{-1}) would be expected over the original LGM50 cell.

In conclusion, as summarised in Figure 6.5, replacing the slurry cast graphite electrode with the as-manufactured, non-porous pyrolytic graphite would result in a 16% maximum theoretical improvement in gravimetric cell energy density. However, this maximum improvement assumes a gravimetric active material capacity of 372 mA h g^{-1}. As shown in Chapter 4, in practice overpotentials will limit gravimetric active material capacity. Introducing porosity could reduce overpotentials, but will also increase inactive material content. Calculations show that up to 38% porosity could be introduced into pyrolytic graphite sheet before the benefit to gravimetric energy density is lost. A pyrolytic graphite sheet with 20% porosity would improve theoretical gravimetric energy density by 9%, but again only if a gravimetric active material capacity of 372 mA h g^{-1} is realised. To obtain a better estimate of theoretical gravimetric energy we need to relax this assumption. The next section will develop a model to estimate the gravimetric active material capacity of pyrolytic graphite sheet patterned with a hexagonal array of circular channels.

6.2 Estimating gravimetric active material capacity

The previous section established that gravimetric energy density is a function of gravimetric active material capacity and porosity. This section will build a model to predict gravimetric active material capacity for pyrolytic graphite sheet of a specified geometry.

Batteries are typically charged and discharged at a constant gravimetric charge or discharge rate. A constant gravimetric discharge rate dictates that for each gram of active material in the electrode, the same amount of charge will enter or exit each second. There is therefore a constant flux of lithium ions at interface between active material and electrolyte, or in modelling terms, a constant flux boundary condition. Fick's second law can be used with this boundary condition to describe the diffusion of lithium ions inside the active material during these constant current steps.

As the channel diameter and pitch is changed, the gravimetric surface area of the active material will change. Under these conditions of a constant gravimetric discharge, a decrease in the gravimetric surface area will result in an increased flux of lithium ions at the active material surface. The diffusion path length inside the active material will also change with channel diameter and pitch. Together these changes to lithium ion flux and diffusion path length will influence the lithium concentration gradient that builds up inside the active material, which in turn will impact the extent of lithiation that can be achieved before a specified cell cut-off voltage is measured.

This model aims to provide an initial assessment of how diffusion in the active material alone is influenced by geometry and could limit lithiation capacity. Whilst it is recognised that in practice the lithiation capacity will also be affected by additional concentration, kinetic, and Ohmic overpotentials, by studying diffusion in the active material in isolation it is possible to understand its geometry dependence and quickly rule out certain designs.

Geometry

The pyrolytic graphite sheet electrodes were modelled by considering a single hexagonal unit cell with specified channel diameter and channel pitch. Ignoring electrolyte overpotential allowed the 3D unit cell to be modelled as a 2D slice (Figure 6.6). Symmetry also allowed only one

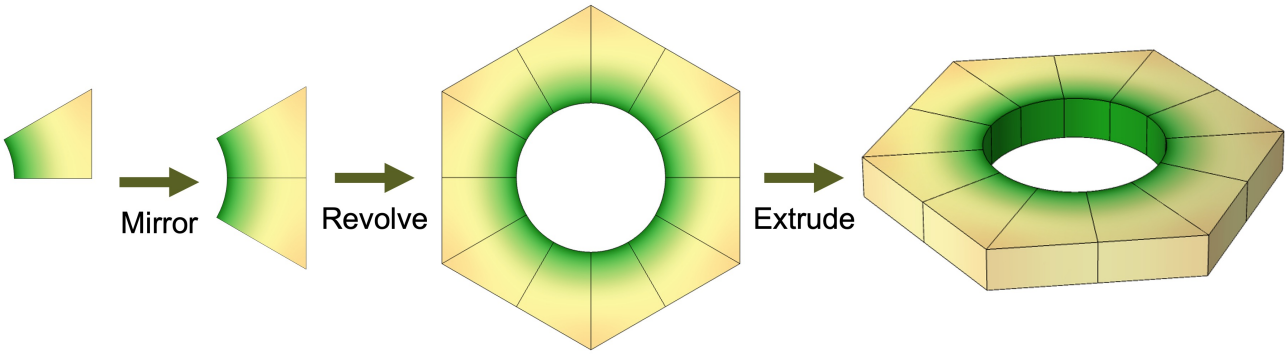


Figure 6.6: The pyrolytic graphite sheet electrodes were modelled by considering a single hexagonal unit cell. Ignoring electrolyte overpotential allowed the 3D unit cell to be modelled as a 2D slice. Symmetry also allowed only one twelfth of the 2D slice to be modelled, further reducing computational expense.

twelfth of the 2D slice to be modelled, further reducing computational expense.

Equations

Diffusion of lithium ions in the active material was modelled using Fick's law. A no-flux boundary condition was set at all boundaries except the channel surface, at which an areal flux was defined. The areal flux was calculated by dividing the gravimetric current density by both the Faraday constant and the gravimetric surface area.

The mass conservation equation for lithium was solved for the active material domain:

$$\frac{\partial c}{\partial t} = D\nabla^2 c \tag{6.1}$$

where c is the concentration of lithium and D is the diffusivity of lithium in the active material [126]. For a planar geometry, this equation can be solved analytically (see Appendix for example). More complex geometries require this equation to be approximated and solved using a numerical method such as the finite element method [127].

The model was run until the lithium concentration at the channel surface reached the specified final surface lithium concentration. The capacity at this cut-off point was calculated by integrating the lithium concentration across the active material domain and multiplying by

Table 6.1: Summary of parameters for gravimetric active material capacity model.

Parameter	Value
Geometry	
Channel diameter, d_h / µm	100
Channel pitch, p_h / µm	160
Active material domain	
Diffusivity, D / $\mathrm{m^2\ s^{-1}}$	5.00×10^{-14}
Initial lithium concentration / $\mathrm{mol\,m^{-3}}$	0
Density, ρ / $\mathrm{g\ cm^{-3}}$	1.90
Theoretical capacity / $\mathrm{mA\ h\ g^{-1}}$	372
Experiment	
Charge rate / $\mathrm{h^{-1}}$	0.10
Calculated	
Gravimetric current density / $\mathrm{mA\,g^{-1}}$	37.2
Final surface lithium concentration / $\mathrm{mol\,m^{-3}}$	26,372

the Faraday constant. This capacity was divided by the active material mass to calculate the gravimetric active material capacity.

Parameters

The default parameters used in the model are listed in Table 6.1. The gravimetric current density is calculated as the product of charge rate and the theoretical capacity. For a specified active material density, ρ, and theoretical capacity, Q_{theo}, the final surface lithium concentration (assuming full lithiation), $c_{\mathrm{s,\,max}}$ can be calculated:

$$c_{\mathrm{s,\,max}} = \frac{Q_{\mathrm{theo}}\rho}{F} \tag{6.2}$$

where F is the Faraday constant.

Results

The model was run for the electrode designs manufactured in Chapter 4. There were three different designs, each containing a hexagonal array of 100 µm diameter channels with a pitch of either 200 µm, 160 µm or 120 µm. For each design, the model was run at three different values of diffusivity: $1 \times 10^{-14}\,\mathrm{m^2\,s^{-1}}$, $5 \times 10^{-14}\,\mathrm{m^2\,s^{-1}}$ and $1 \times 10^{-13}\,\mathrm{m^2\,s^{-1}}$. In each case,

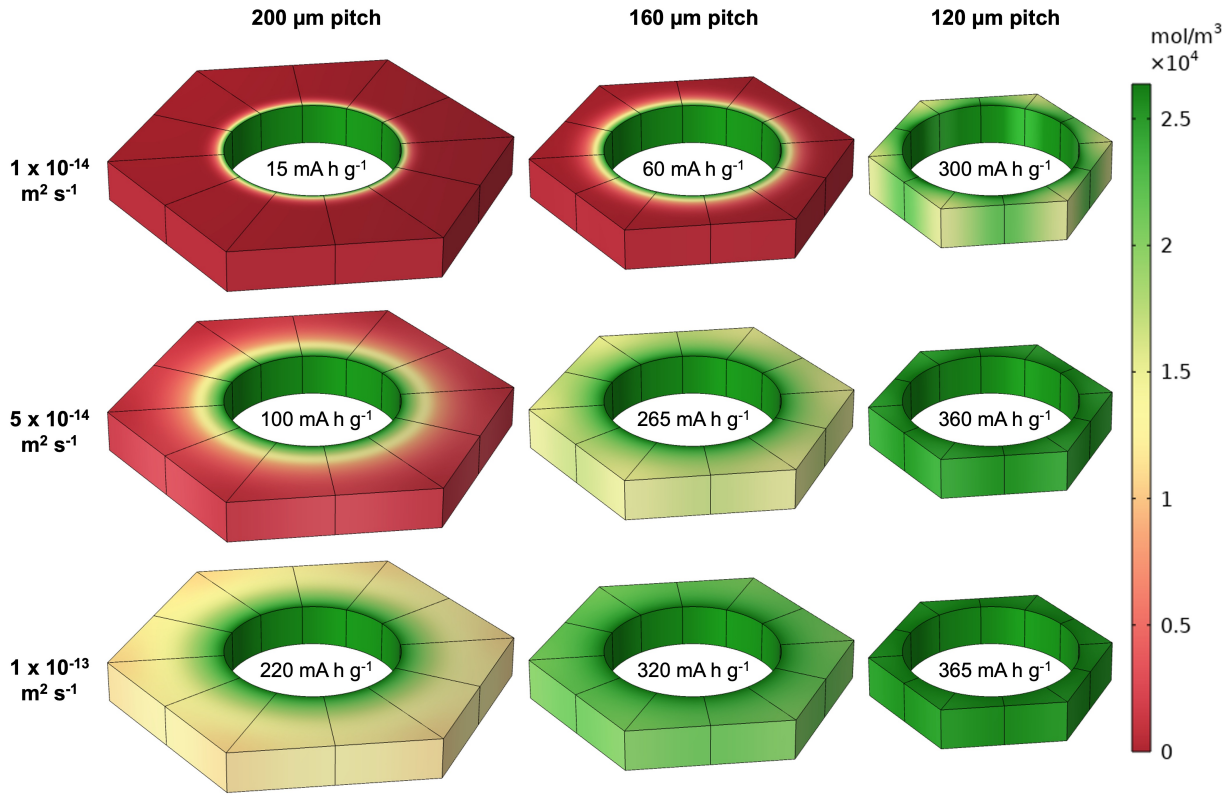


Figure 6.7: Lithium concentration in the hexagonal unit cell when surface concentration reached 100% SOC, plotted for 3 different designs and 3 different values of diffusivity. The gravimetric active material capacity was calculated by integrating the lithium concentration and is shown for each design. For a fixed value of diffusivity, it is observed that as pitch reduces the gravimetric active material capacity increases. Equally, as diffusivity is increased, shallower concentration gradients form inside the active material during lithiation and gravimetric active material capacity increases.

the concentration of lithium at cut-off is plotted in Figure 6.7 alongside the gravimetric active material capacity.

First, for a fixed value of diffusivity, it is observed that as pitch reduces the gravimetric active material capacity increases. This trend is consistent with the experimental data in Chapter 4. As pitch is reduced for a design with fixed channel diameter, the gravimetric surface area of the unit cell increases. For a fixed gravimetric current density, as gravimetric surface area increases, areal current density decreases. As shown in Figure 6.7, shallower lithium concentration gradients therefore form as pitch is reduced. These shallower gradients allow more lithium to enter the active material before the cut-off surface lithium concentration is reached.

Figure 6.7 also shows that the model is sensitive to the diffusivity of lithium in the active material. As diffusivity is increased, shallower concentration gradients form inside the active material during lithiation for a fixed areal current density. These shallower gradients again result in a higher gravimetric active material capacity. For the 160 µm pitch design, the estimated gravimetric active material capacity rises from 60 mA h g^{-1} to 320 mA h g^{-1} as diffusivity is increased from 10^{-14} m^2 s^{-1} to 10^{-13} m^2 s^{-1}.

Parameter sweep

For a wider exploration of the design space, a parameter sweep was run for values of channel diameter between 5 µm and 100 µm, and values of porosity between 5% and 40%. Porosity was specified instead of channel pitch to ensure that only viable cell geometries were produced. The channel pitch in each case was calculated using equation 6.3 (see Methods section for further detail):

$$\text{Channel pitch} = \frac{\text{Channel diameter}}{\sqrt{\text{Porosity}/0.9069}} \tag{6.3}$$

Figure 6.8A shows that the predicted gravimetric active material capacity increases as channel diameter decreases and porosity increases. To exceed a gravimetric active material capacity of 350 mA h g^{-1} at a porosity of less than 30%, channel diameter must be less than 40 µm. As channel diameter is reduced, the same gravimetric active material capacity can be achieved at a lower value of porosity. At a channel diameter of 20 µm, a gravimetric active material capacity of 350 mA h g^{-1} is predicted with 15% porosity.

The model output is re-plotted in Figure 6.8B with channel pitch rather than porosity on the y axis. The lower blank area in this plot represents where porosity is greater than 40% and the upper blank region where porosity is below 5%. This plot more clearly shows the pitch required for a design with a specified channel diameter to exceed a gravimetric active material capacity of 350 mA h g^{-1}. For instance, pitch must be below 70 µm for a design with a channel diameter of 40 µm to exceed 350 mA h g^{-1}. Instead of channel pitch, Figure 6.8C plots the minimum distance between channels on the y axis. The minimum distance between channels gives an indication of the diffusion path length. It is interesting to observe that for a fixed path

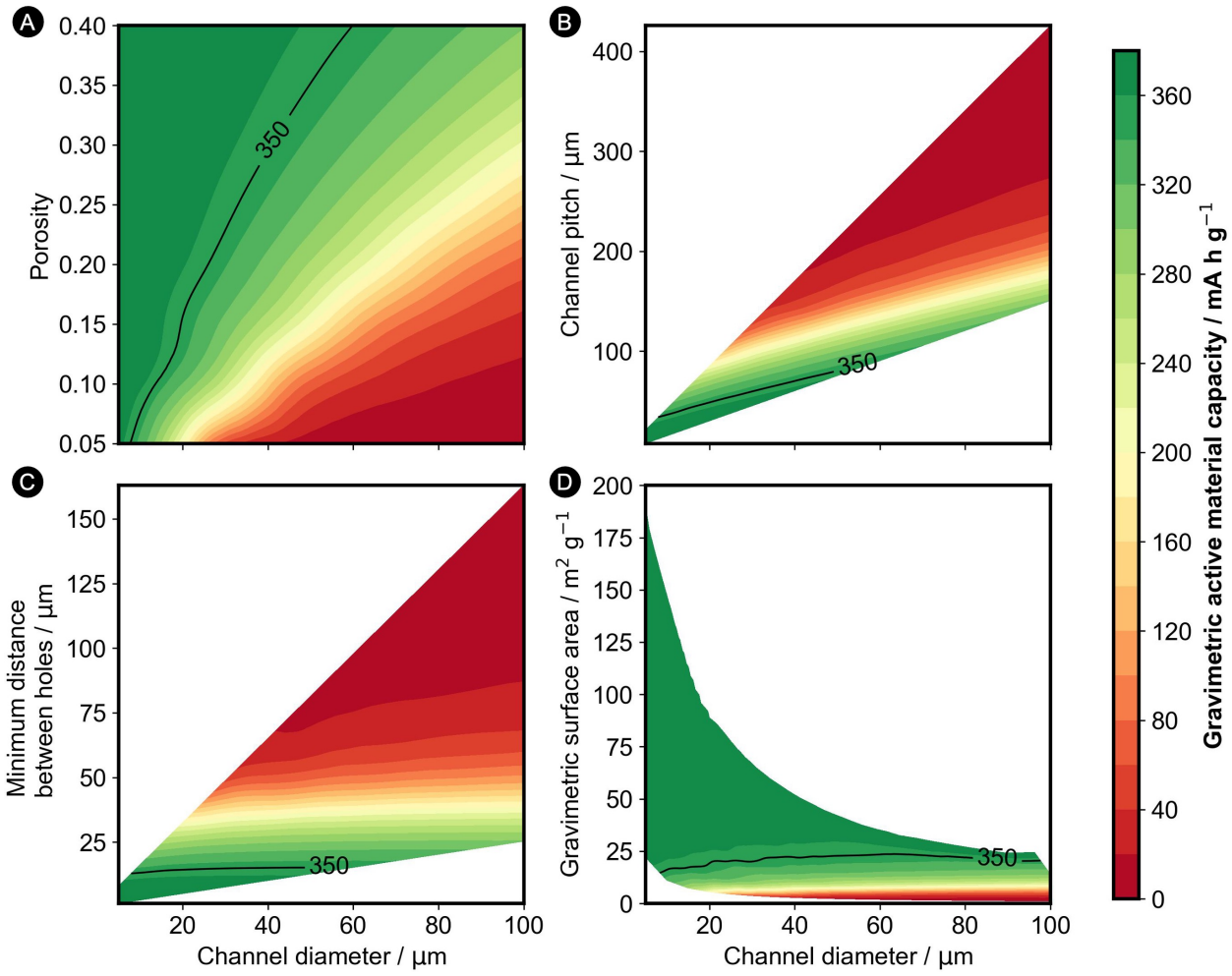


Figure 6.8: The predicted gravimetric active material capacity increases as channel diameter decreases and porosity increases. Increasing porosity for a given channel diameter is equivalent to reducing channel pitch (or the minimum distance between channels), or increasing gravimetric surface area. The contours are not perfectly straight due to error associated with the stop condition in the COMSOL simulation.

length, the gravimetric active material capacity is less dependent on channel diameter when channels are more closely spaced. This relationship is shown by the largely horizontal contours when the minimum distance between channels is below 25 µm. Finally, Figure 6.8D confirms that gravimetric active material capacity increases with gravimetric surface area.

Estimating gravimetric energy density

It is clear from Figure 6.8 that high porosity, small channel diameter designs will maximise gravimetric active material capacity. However, as discussed in Chapter 5, high porosity electrode designs can limit gravimetric energy density at commercial cell level. We can combine the

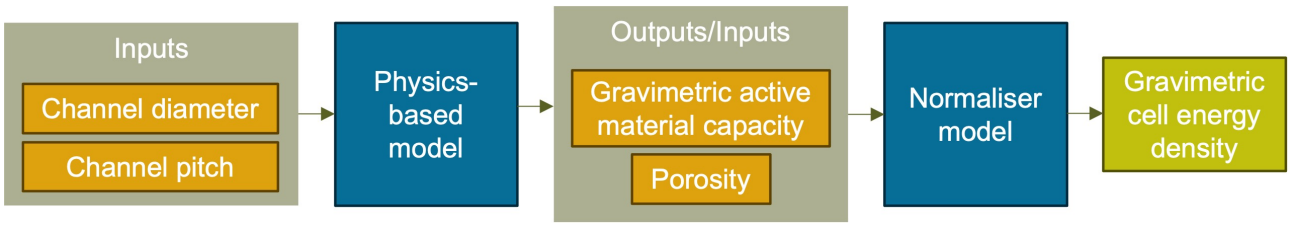


Figure 6.9: There are two key steps required to predict the gravimetric cell energy density of a given pyrolytic graphite sheet electrode design. First, for a specified channel diameter and pitch, a physics-based model is used to estimate the gravimetric active material capacity. This value, alongside the pyrolytic graphite sheet electrode porosity, is then used in the normalisation model to estimate the gravimetric energy density of a commercial cell that incorporates the pyrolytic graphite sheet electrode.

normalisation model developed in that chapter with these results to estimate the gravimetric energy density (Figure 6.9) of a cell with specified geometry.

To use the normalisation model from Chapter 5 a number of assumptions must be made. Firstly, it is assumed that the electrode is made up of pyrolytic graphite sheet with a density of $1.9\,\mathrm{g\,cm^{-3}}$ and there is no binder, conductive additive or separate current collector. It is also assumed that the thickness of pyrolytic graphite sheet electrode is such that its areal capacity is equivalent to an existing LGM50 negative electrode. Finally, the counter electrode and all other cell components are assumed to be the same as used in the LGM50 cell. These assumptions are equivalent to swapping out the negative electrode in an existing LGM50 cell for a pyrolytic graphite sheet electrode with equivalent areal capacity.

By combining the normalisation model and the model for estimating gravimetric active material density, Figure 6.10 shows gravimetric active material capacity and gravimetric energy density plotted as a function of channel diameter and channel pitch. The results suggest that for a given channel diameter, low or high values of porosity are detrimental to gravimetric energy density. At low values of porosity, gravimetric active material capacity is low and limits gravimetric energy density. Conversely, at high values of porosity, gravimetric active material capacity is high but there is also now excessive porosity filled with electrolyte that negatively impacts gravimetric energy density. For instance, at a channel diameter of 30 µm, channel pitch should be 60 µm to maximise gravimetric energy density. A smaller pitch of 50 µm would result in higher gravimetric active material capacity, but lower gravimetric energy density.

Figure 6.11 shows the results of re-running the parameter sweep for values of channel di-

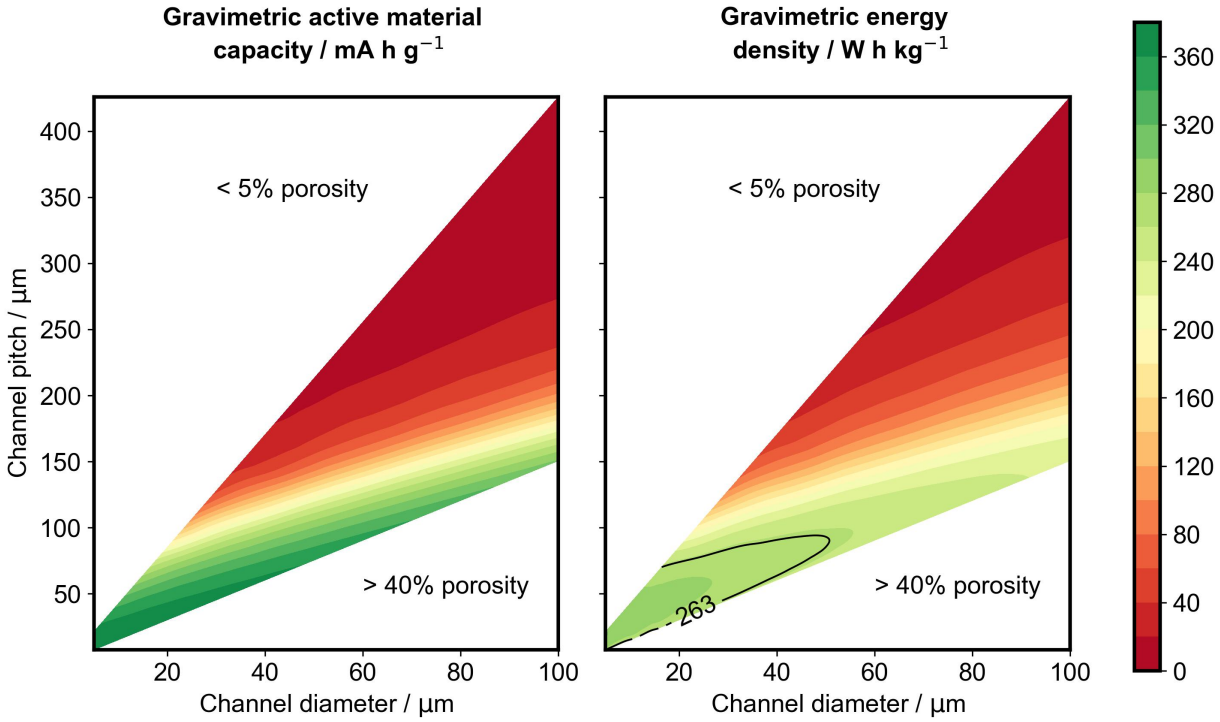


Figure 6.10: A parameter sweep was conducted for values of channel diameter between 5 µm and 100 µm and values of porosity between 5% and 40% to estimate gravimetric active material capacity. The normalisation model was then used to estimate the gravimetric energy density. At low values of porosity, gravimetric active material capacity is low and limits gravimetric energy density. Conversely, at high values of porosity, gravimetric active material capacity is high but there is also now an excess of electrolyte that negatively impacts gravimetric energy density.

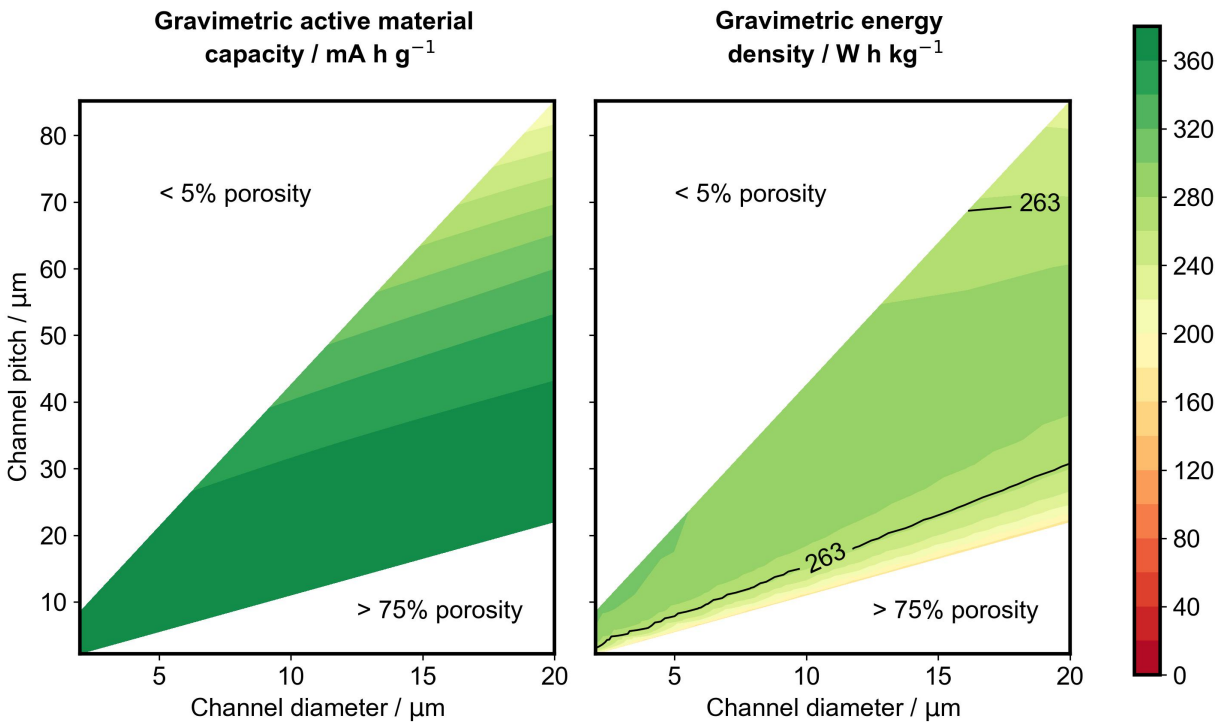


Figure 6.11: A parameter sweep was conducted for values of channel diameter between 2 µm and 20 µm and values of porosity between 5% and 75% to estimate gravimetric active material capacity. The normalisation model was then used to estimate the gravimetric energy density. To maximise gravimetric energy density, porosity should be kept at an intermediate value. Too low porosity will limit gravimetric active material capacity and lead to an excess mass and volume of active material. Too high porosity will lead to an excess mass and volume of electrolyte.

ameter between 2 µm and 20 µm, and values of porosity between 5% and 75%. This figure more clearly shows that to maximise gravimetric energy density, porosity should be kept at an intermediate value. Too low porosity will limit gravimetric active material capacity and lead to an excess mass and volume of active material. Too high porosity will lead to an excess mass and volume of electrolyte. For a channel diameter of 5 µm or below, porosity should be kept below 5%.

In summary, for high gravimetric active material capacity, channel diameter should be minimised and porosity should be maximised. However, to maximise gravimetric energy density at commercial cell level, an intermediate value of porosity should be chosen. Too low porosity will limit gravimetric active material capacity and lead to an excess mass and volume of active material. Too high porosity will lead to an excess mass and volume of electrolyte.

The manufactured and optimised designs of pyrolytic graphite sheet electrode are com-

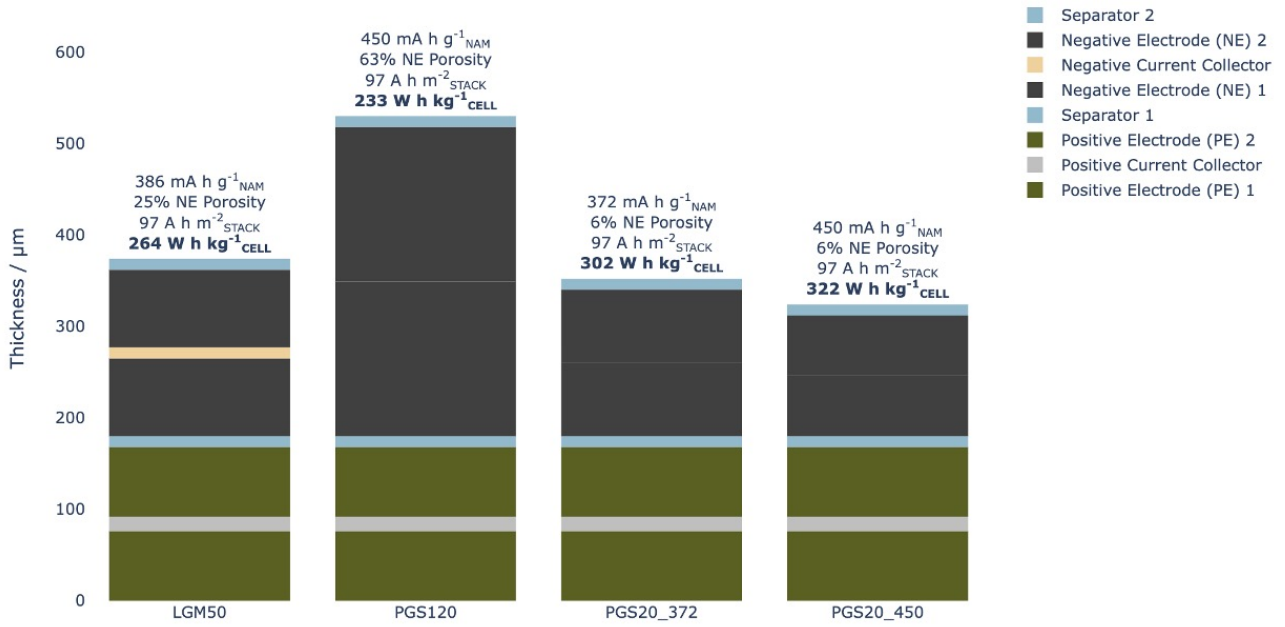


Figure 6.12: A pyrolytic graphite sheet electrode with a hexagonal array of 5 µm diameter, 20 µm pitch channels (6% porosity due to channels) could increase the gravimetric energy density of a LGM50 cell by 15% to 302 W h kg^{-1}. If a gravimetric active material capacity of 450 mA h g^{-1}, as measured in Chapter 4, instead of 372 mA h g^{-1} is assumed then a 22% improvement in gravimetric cell energy density to 322 W h kg^{-1} is predicted. The higher gravimetric active material capacity in this second scenario allows a thinner pyrolytic graphite sheet electrode (132 µm rather than 160 µm) to achieve the same areal capacity. For reference, the PGS120 cell with 100 µm channel diameter, 120 µm channel pitch pyrolytic graphite sheet electrodes from earlier discussions is also shown.

pared in Figure 6.12. A pyrolytic graphite sheet electrode with a hexagonal array of 5 µm diameter, 20 µm pitch channels (6% porosity due to channels) could increase the gravimetric energy density of a LGM50 cell by 15% to 302 $\mathrm{W\,h\,kg^{-1}}$. If a gravimetric active material capacity of 450 $\mathrm{mA\,h\,g^{-1}}$, as measured in Chapter 4, instead of 372 $\mathrm{mA\,h\,g^{-1}}$ is assumed then a 22% improvement in gravimetric cell energy density to 322 $\mathrm{W\,h\,kg^{-1}}$ is predicted. The higher gravimetric active material capacity in this second scenario allows a thinner pyrolytic graphite sheet electrode (132 µm rather than 160 µm) to achieve the same areal capacity. Computer-aided design drawings for the LGM50 stack incorporating the manufactured (100 µm channel diameter, 120 µm channel pitch) and optimised (5 µm channel diameter, 20 µm channel pitch) pyrolytic graphite sheet electrode designs are shown in Figures 6.13 and 6.14.

Limitations

It is important to acknowledge the limitations of the model results presented in this chapter. The primary limitation of these results is that they are not experimentally validated. Whilst the trends are consistent with the experimental data from Chapter 4, more data should be collected under controlled conditions for model validation. Additionally, the model results indicate that a much smaller channel diameter is required. Data should be collected for a range of electrode designs to avoid extrapolation.

There are also a number of assumptions made in the modelling work that may need to be relaxed following collection of validation data. Firstly, for the parameter sweeps, diffusivity of lithium in the graphite was assumed to have a constant value of $5 \times 10^{-14}\,\mathrm{m^2\,s^{-1}}$. As shown in Figure 6.7, the value of diffusivity will influence the concentration overpotential. Diffusivity may also be a function of the lithium concentration inside the active material, in which case a constant assumed value may not be applicable [128].

Secondly, there was also a key assumption made in this analysis of negligible kinetic, electrolyte concentration and Ohmic overpotentials. This assumption was implemented by fixing the surface concentration of lithium at which lithiation was assumed to stop and greatly reduced computational expense. On one hand, this assumption could be considered reasonable for an initial investigation of pyrolytic graphite sheet electrodes. The introduced electrolyte

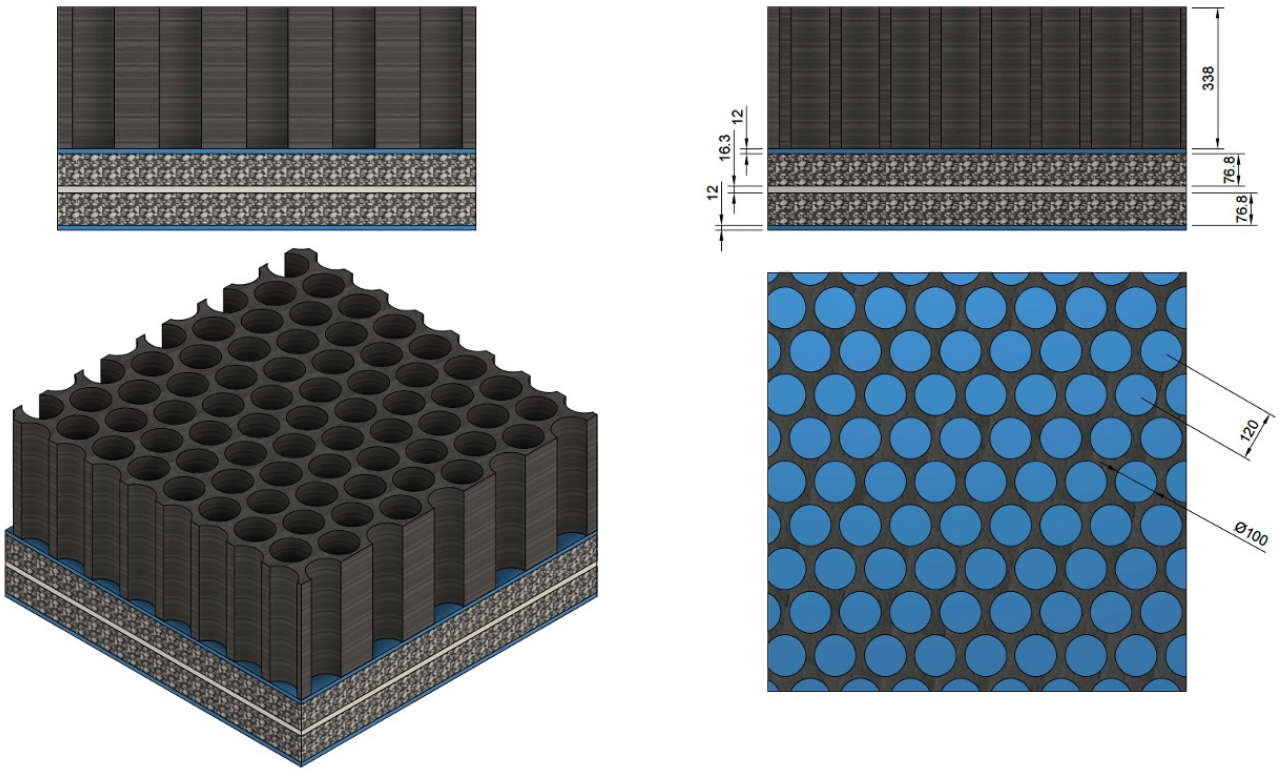


Figure 6.13: Computer-aided design drawings for the LGM50 stack incorporating the manufactured (100 µm channel diameter, 120 µm channel pitch) pyrolytic graphite sheet electrode design. The pyrolytic graphite sheet electrode has a thickness of 338 µm. All dimensions are in µm.

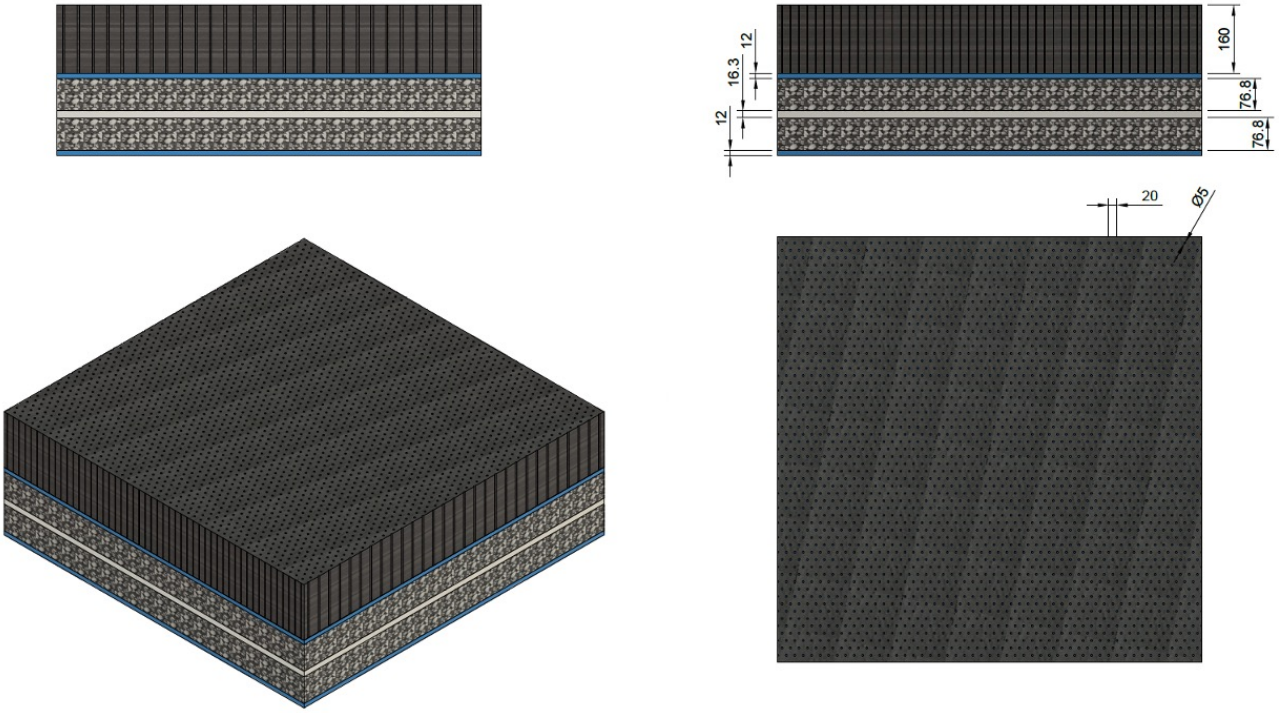


Figure 6.14: Computer-aided design drawings for the LGM50 stack incorporating the optimised (5 µm channel diameter, 20 µm channel pitch) pyrolytic graphite sheet electrode design. The pyrolytic graphite sheet electrode has a thickness of 160 µm. All dimensions are in µm.

channels provide a low tortuosity electrolyte domain inside the pyrolytic graphite sheet electrodes which is expected to reduce electrolyte overpotential. High electrical conductivity of the pyrolytic graphite sheet and the absence of contact resistances both between particles and at the interface with a metal current collector are also expected to reduce Ohmic overpotential. The model was also run at a low charge rate of 0.1C, which will reduce kinetic (and other overpotentials). However, whilst this assumption was useful for studying the influence of diffusion in the active material in isolation and quickly ruling out certain designs, future work could relax this assumption by modelling the charge-transfer reaction and diffusion of ions in the electrolyte. Irreversible reactions are also not modelled. The presented model results show that gravimetric surface area is beneficial for gravimetric active material capacity. However, the amount of lithium consumed in irreversible reactions will also increase with gravimetric surface area. The effect of irreversible reactions should be included when optimising electrode design.

Where the normalisation model has been used to estimate gravimetric energy density, a number of additional assumptions have also been made. Firstly, the parameter set presented in Table 5.1 was used. The model works by calculating the properties of a commercial cell with a specified electrode incorporated. To do so, it is assumed that all components except the specified electrode have the same properties as an LGM50 cell. For instance, the separator thickness and mass of casing are the same as an LGM50 cell. Additionally, in the case that the properties of a counter electrode are calculated rather than specified, the counter electrode is assumed to have the same composition and gravimetric active material capacity as the relevant LGM50 electrode. By challenging and changing these parameter values, it may be possible to further optimise gravimetric energy density.

6.3 Conclusions

This chapter investigates the design of a practical pyrolytic graphite sheet electrode through simulation. First, a non-porous pyrolytic graphite sheet electrode was considered. Replacing the slurry cast negative electrode of an LGM50 cell with non-porous pyrolytic graphite sheet of equivalent areal capacity would increase cell gravimetric energy density by 16% to 307 $\mathrm{W\,h\,kg^{-1}}$.

This value is the maximum theoretical improvement based on the theoretical gravimetric active material capacity of graphite ($372\,\mathrm{mA\,h\,g^{-1}}$).

However, as shown in Chapter 4, gravimetric active material capacity of non-porous pyrolytic graphite sheet is much lower in practice and so porosity must be introduced. A porous pyrolytic graphite sheet was therefore considered instead. The model from Chapter 5 was used to show that gravimetric energy density of an LGM50 cell could be improved if pyrolytic graphite sheet is able to achieve a gravimetric active material capacity of $372\,\mathrm{mA\,h\,g^{-1}}$ at less than 38% porosity. Under these assumptions, a pyrolytic graphite sheet with 20% porosity would improve the gravimetric cell energy density of an LGM50 cell by 9%. Further analysis showed that if gravimetric active material capacity is lower then porosity must also be lower to achieve a specified gravimetric energy density. Equally, a higher porosity can be tolerated if gravimetric active material capacity is higher than the theoretical value, as for the $450\,\mathrm{mA\,h\,g^{-1}}$ measured in Chapter 4.

Having established the relationship between gravimetric active material capacity, porosity and gravimetric energy density, a model was built to explore the impact of electrode design on gravimetric active material capacity. The concentration of lithium inside a hexagonal unit cell was simulated with a constant flux boundary condition at the electrolyte interface. The model results supported the trends observed in Chapter 4. As pitch is reduced for a fixed channel diameter, gravimetric active material capacity increases. This increase is also a function of the diffusivity of lithium in the active material. Channels should have a small diameter and be closely packed to maximise gravimetric active material capacity.

However, Chapter 5 showed that gravimetric active material capacity is a poor metric for design of a commercial cell. Gravimetric energy density of an LGM50 cell with the specified pyrolytic graphite sheet electrodes was therefore estimated using the normalisation model. The results showed that to maximise gravimetric energy density channels should have a small diameter, but it is important that they are not too closely packed. Close packing of channels increases electrode porosity and leads to an excessive mass and volume of electrolyte in the cell stack. Under the assumptions in this chapter, a pyrolytic graphite sheet electrode with a hexagonal array of 5 µm diameter, 20 µm pitch channels could increase the gravimetric energy

density of a LGM50 cell by 15% to 302 $\mathrm{W\,h\,kg^{-1}}$, which potentially represents a significant technological improvement.

Overall this chapter demonstrates a strategy for the design of a practical pyrolytic graphite sheet electrode. Although the model for prediction of gravimetric active material capacity provides useful insights on how certain geometries could be limited by diffusion in the active material alone , it presents a "best case" scenario as only diffusion in the active material is studied. Future work should consider the impact of kinetic, electrolyte concentration and Ohmic overpotentials.

6.4 Methods

Calculating porosity of a hexagonal array of circular channels

For a unit cell consisting of a solid hexagon with a circular channel at its centre, its porosity can be calculated as follows:

$$\text{Porosity} = \frac{\text{Channel area}}{\text{Hexagon area}} \tag{6.4}$$

$$\text{Channel area} = \frac{\pi d^2}{4} \tag{6.5}$$

$$\text{Hexagon area} = 6\tan(30^\circ)(\frac{p^2}{4}) = \frac{1}{0.9069}\frac{\pi p^2}{4} \tag{6.6}$$

where d = channel diameter, and p = channel pitch

The packing density for circles in a hexagonal array is 0.9069. Using this number, the above equations can be combined into a single equation for porosity of a hexagonal unit cell with a circular channel at its centre:

$$\text{Porosity} = 0.9069\frac{d^2}{p^2} \tag{6.7}$$

Normalisation model

Please refer to Chapter 5 for details of the normalisation model.

Physics-based model

The physics-based model was implemented in the commercial software package COMSOL Multiphysics V6.0. Please refer to the main text of this chapter for parameters and implementation details.

Chapter 7

Conclusions and further work

All commercial battery electrodes today are manufactured by slurry-casting active material powder on to a metal current collector foil. This manufacturing process has been proven over decades and is embedded, but the resulting electrodes limit cell performance. This thesis documents a quantitative, first-principles re-design of the battery electrode for improved gravimetric energy density at commercial cell level.

First, an existing commercial lithium-ion battery was quantitatively analysed to establish a baseline and identify the key sources of loss. The LGM50 cell only achieves 52% of its theoretical gravimetric energy density at a discharge rate of 0.1C, and less than 20% at a discharge rate of 4C. This finding highlighted that there is potentially substantial opportunity to improve cell performance using existing cell chemistries. Inactive materials and overpotentials were identified as the key sources of loss, prompting research into the design of a low inactive mass, low overpotential battery electrode.

Next, pyrolytic graphite sheet was identified as a promising material for manufacture of a low inactive mass, low overpotential electrode. However, initial trials revealed very low gravimetric active material capacity of less than $10\,\mathrm{mA\,h\,g^{-1}}$. Laser drilling to form channels was successfully demonstrated and used to manufacture pyrolytic graphite sheet electrodes with arrays of electrolyte channels. Following the introduction of electrolyte channels, the gravimetric active material capacity of pyrolytic graphite sheet was measured to increase by a factor of 40 to $450\,\mathrm{mA\,h\,g^{-1}}$.

Although gravimetric active material capacity is a useful metric for assessing the extent of

lithiation of novel active materials, it is insufficient for designing an improved commercial cell. A model was therefore developed to estimate the gravimetric energy density of a commercial cell from electrode characterisation data. This model revealed that the manufactured pyrolytic graphite sheet electrodes would severely restrict the gravimetric energy density of a commercial cell, despite having high gravimetric active material capacity. The manufactured electrodes performed poorly due to low areal capacity and high electrode porosity, highlighting that their design needed to be optimised for use in a commercial cell. The model was deployed as a web app to help other researchers contextualise their research.

Finally, the design of a practical pyrolytic graphite sheet electrode was investigated. The gravimetric energy density of a commercial cell that incorporates pyrolytic graphite sheet electrodes is a strong function of gravimetric active material capacity and electrode porosity. These two parameters are themselves interdependent and a function of several other parameters. A two-step model was developed to estimate the gravimetric active material capacity and then the gravimetric energy density of a commercial cell for a given electrode design. Using the model, the channel diameter and pitch of a pyrolytic graphite sheet electrode was optimised for improved gravimetric energy density at commercial cell level. Results showed that whilst channel diameter should be minimised, the channels should not be too closely packed to avoid excessive porosity. A pyrolytic graphite sheet electrode with a hexagonal array of 5 µm diameter, 20 µm pitch channels could increase the gravimetric energy density of a LGM50 cell by 15% to 302 $\mathrm{W\,h\,kg^{-1}}$.

7.1 A design methodology for battery electrodes

A key output from this thesis is a design methodology for battery electrodes. Chapters 3 to 6 cover a design cycle, from an initial assessment of baseline performance and improvement opportunities through to proof of concept and optimisation using the right metrics (Figure 7.1). Importantly, this design cycle tackles the challenges faced by many laboratories today that do not have the facilities to manufacture practical, large format cells. For these laboratories, it is crucial that data collected in coin cells can be translated and compared to commercial cell data. The method presented in Chapter 5 currently estimates LGM50 gravimetric energy

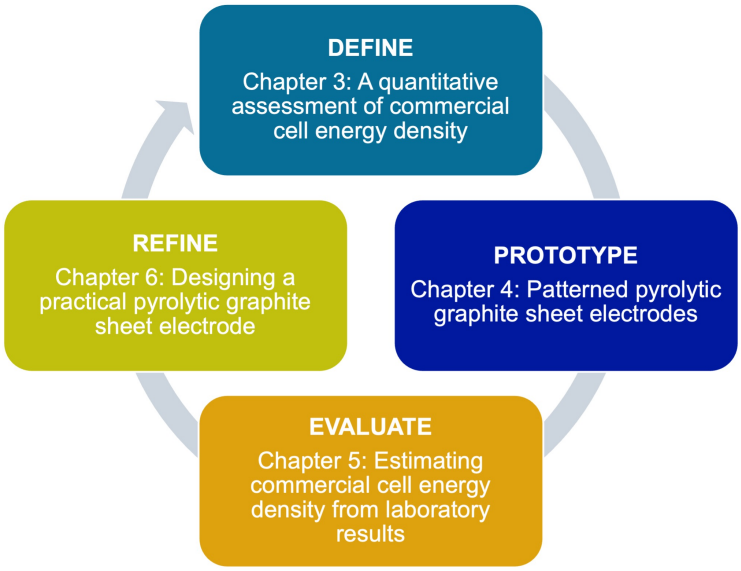


Figure 7.1: Chapter 3 performs a quantitative assessment of a representative commercial lithium-ion cell to prioritise areas for research and development. Guided by these findings, Chapter 4 demonstrates the introduction of electrolyte channels to improve the gravimetric active material capacity of pyrolytic graphite sheet by 40 times. Chapter 5 highlights the limitations of gravimetric active material capacity as a metric for commercial cell design and develops a model to estimate commercial cell energy density. Finally, Chapter 6 investigates the design of a practical pyrolytic graphite sheet electrode.

density from laboratory data, but there is room for expansion to include other metrics and cell chemistries.

High impact research and development depends on the right metrics. The right metrics are an indispensable reference for evaluating ideas and results, and crucial for maintaining alignment with higher-level goals. The high-level goal in this thesis was to design a better battery electrode. However, as discussed in Chapter 3, the definition of "better" strongly depends on the application. Given the pivotal role that electrification of transport has in society's transition away from fossil fuels, gravimetric energy density of a commercial cell was chosen as the key metric for this thesis. It is however acknowledged that gravimetric energy density at a specified discharge rate ignores a number of essential considerations such as suitability for mass manufacture, safety, cost, degradation, recycling, and material availability. Future work should incorporate additional metrics for a more holistic design.

Finally, the LGM50 cell is identified early in this thesis as a representative commercial cell and used throughout for evaluation of different electrode designs. Although this approach is an improvement over considering gravimetric active material capacity in isolation, it will inherently

bias optimisation work. The gravimetric energy density calculated for designs in Chapter 6 assumes in all cases that all components except the negative electrode are the same as the LGM50 cell. Future work should relax this assumption by considering alternative reference cells and component specifications. For instance, the optimal areal capacity and composition of the counter electrode will vary depending on the design of the pyrolytic graphite sheet electrode and, crucially, the intended battery application.

7.2 Structured, monolithic electrodes

Another important output from this thesis is the concept of structured, monolithic electrodes. Patterning of a monolithic active material sheet is demonstrated as a potential alternative to slurry casting for battery electrode manufacture. This alternative method has the potential to improve battery sustainability and performance by eliminating inactive materials and solvents, and creating a regular and low-tortuosity electrode microstructure. By avoiding the conventional particle-based battery electrode architecture, there could be additional benefits related to fast charging, manufacturing, energy intensity, cost, thicker electrodes, safety, degradation, thermal management and lifetime. While the method was demonstrated specifically for negative graphite lithium-ion electrodes in this study, it has the potential to be adapted for use in the production of both negative and positive electrodes across various battery chemistries [117]. In addition to performance, the uniform microstructure of structured monolithic electrodes offers an ideal model system for operando characterisation with techniques such as optical microscopy and galvanostatic intermittent titration that struggle due to the random microstucture of slurry cast electrodes.

The early stage of this research is however recognised and further work is required to develop its technology readiness level. Testing with more representative cycling protocols and larger cell formats is required to fully evaluate the potential of pyrolytic graphite sheet, and more generally, structured monolithic electrodes. Similarly, laser drilling was used in this study to prototype the electrodes, and may be applicable to large scale production, but alternative methods of forming an active material sheet with channels could be more suitable. Pyrolytic graphite sheet has a similar manufacturing route to the powdered synthetic graphite used in

today's batteries, but requires only a single patterning step for transformation into a battery electrode. Compared to the many complex steps of the slurry casting method for powders, there may be potential for significant energy and cost savings, not least by avoiding the use of solvents, but further work is required before a detailed assessment can be made. Finally, the electrical and thermal conductivity of a pyrolytic graphite sheet electrode is orders of magnitude higher than slurry cast electrodes. Testing in full cell configuration with a practical cell format could reveal additional performance benefits related to reduced Ohmic resistance and more uniform thermal dissipation.

7.3 Future work

In summary, future work should focus on building a practical cell with pyrolytic graphite sheet electrodes to demonstrate this technology at a higher technology readiness level.

Firstly, the viability of this technology in terms of energy, cost, and sustainability should be conducted. The "energy consumption of current and future production of lithium-ion and post lithium-ion battery cells" was comprehensively investigated in a recent publication [129]. A similar approach should be taken to assess not only the energy consumption, but also the cost and sustainability, of pyrolytic graphite sheet electrodes. Importantly, this analysis should be conducted alongside other emerging battery technologies, such as solid-state cells and lithium metal electrodes, to understand the relative position of structured monolithic electrodes in the battery landscape.

Secondly, further characterisation data should be collected to validate the existing model results. Care should be taken that the protocols used for testing ensure highly quality data to support model validation. This collection of characterisation data should be conducted iteratively in tandem with modelling work. As required, additional physics should be added to the model until validation is achieved. Following validation, the model can be used as a design tool to iterate to the optimum structure. It will be important to carefully select the metrics used for optimisation to design a practical battery that is performant for a specified application, whilst also meeting targets related to energy, cost, and sustainability.

It is anticipated that engineering challenges will be encountered, and will need to be over-

come, as scale up is attempted. For instance, tab design must be considered to make electrical connections in a pouch or cylindrical cell format. Without the copper current collector foil, a new solution is required. It may be possible to adopt the "tabless" design used in Tesla cells by laser cutting the graphite sheet instead of the copper foil. However, unlike copper, graphite cannot readily be welded, so a new method of forming the electrical connection to the external circuit will be required. It is also possible that with further characterisation, degradation mechanisms are uncovered. For instance, pore clogging due to manufacturing debris or SEI growth could cause problems and necessitate design modifications. Forward looking trials, for instance to demonstrate suitability for high speed roll-to-roll manufacture, could also be conducted to de-risk future scale up.

Lastly, the modelling tools developed in this thesis could be expanded independently of the development required to support the production of a practical cell. There is an opportunity to produce more general tools that help other researchers contextualise their laboratory results. The normalisation model could be expanded to further breakdown the "excess mass", to include additional reference cells (besides the LGM50 cell), and to output additional cell metrics.

Outputs

Submitted

SW Hair & MSP Shaffer *Beyond slurry cast: flexible, free-standing, solvent-free and low tortuosity graphite battery electrodes* (2023).

In preparation

SW Hair, I Squires & SJ Cooper *Better metrics for better batteries: an intuitive web application to estimate commercial cell performance from laboratory results* (2023) + Poster presented at Oxford Battery Modelling Symposium 2023.

SW Hair, E Dickinson & SJ Cooper *Galvanostatic Intermittent Titration Technique: a critical review and best practice* (2023).

SW Hair & SJ Cooper *A quantitative analysis of commercial cell performance* (2023).

Patent pending

Hair *et al. Electrodes* Patent Application No. GB2215623.6 (2022).

Bibliography

[1] Battery Design. *LG INR21700 M50*. en-US. May 2023. URL: https://www.batterydesign.net/lg-inr21700-m50/ (visited on 08/15/2023).

[2] Bengt Sundén. "Chapter 6 - Thermal management of batteries". In: *Hydrogen, Batteries and Fuel Cells*. Ed. by Bengt Sundén. Academic Press, Jan. 2019, pp. 93–110. ISBN: 978-0-12-816950-6. DOI: 10.1016/B978-0-12-816950-6.00006-3. URL: https://www.sciencedirect.com/science/article/pii/B9780128169506000063 (visited on 08/17/2023).

[3] Batemo GmbH. *Batemo | Understanding Batteries*. en-US. URL: https://www.batemo.de/ (visited on 08/11/2023).

[4] QuantumScape. *Energy density: Active materials & electrode loading*. en-US. May 2023. URL: https://www.quantumscape.com/resources/blog/energy-density-active-materials-electrode-loading/ (visited on 08/31/2023).

[5] European Central Bank. "Greener and cheaper: could the transition away from fossil fuels generate a divine coincidence?" en. In: (Nov. 2022). URL: https://www.ecb.europa.eu/press/key/date/2022/html/ecb.sp221116~c1d5160785.en.html (visited on 08/10/2023).

[6] Tesla. *Master Plan Part 3 | Tesla*. en-EU. May 2023. URL: https://www.tesla.com/en_eu/blog/master-plan-part-3 (visited on 08/10/2023).

[7] Jennifer Rankin. "EU limits subsidies for burning trees under renewable energy directive". en-GB. In: *The Guardian* (Sept. 2022). ISSN: 0261-3077. URL: https://www.theguardian.com/environment/2022/sep/14/eu-limits-subsidies-for-burning-trees-under-renewable-energy-directive (visited on 08/31/2023).

[8] Jill W. Moraski, Natalie D. Popovich, and Amol A. Phadke. "Leveraging rail-based mobile energy storage to increase grid reliability in the face of climate uncertainty". en. In: *Nature Energy* 8.7 (July 2023). Number: 7 Publisher: Nature Publishing Group, pp. 736–746. ISSN: 2058-7546. DOI: 10.1038/s41560-023-01276-x. URL: https://www.nature.com/articles/s41560-023-01276-x (visited on 08/15/2023).

[9] McKinsey. *Lithium-ion battery demand forecast for 2030 | McKinsey*. Jan. 2023. URL: https://www.mckinsey.com/industries/automotive-and-assembly/our-insights/battery-2030-resilient-sustainable-and-circular (visited on 08/10/2023).

[10] Sony. *Sony Global - Press Release - Announcement of New Lithium Ion Batteries, Realizing Industry's Highest Level of Energy Density - High-power output cylindrical lithium ion battery fit for high-power supply also announced -*. Sept. 2004. URL: https://www.sony.com/en/SonyInfo/News/Press_Archive/200412/04-060E/ (visited on 08/10/2023).

[11] Yoshio Nishi. "Lithium ion secondary batteries; past 10 years and the future". en. In: *Journal of Power Sources*. Journal of Power Sources Volume 100 100.1 (Nov. 2001), pp. 101–106. ISSN: 0378-7753. DOI: 10.1016/S0378-7753(01)00887-4. URL: https://www.sciencedirect.com/science/article/pii/S0378775301008874 (visited on 08/10/2023).

[12] Alvaro Masias, James Marcicki, and William A. Paxton. "Opportunities and Challenges of Lithium Ion Batteries in Automotive Applications". In: *ACS Energy Letters* 6.2 (Feb. 2021). Publisher: American Chemical Society, pp. 621–630. DOI: 10.1021/acsenergylett.0c02584. URL: https://doi.org/10.1021/acsenergylett.0c02584 (visited on 08/10/2023).

[13] BloombergNEF. *Lithium-ion Battery Pack Prices Rise for First Time to an Average of $151/kWh*. en-US. Section: Press Release. Dec. 2022. URL: https://about.bnef.com/blog/lithium-ion-battery-pack-prices-rise-for-first-time-to-an-average-of-151-kwh/ (visited on 08/10/2023).

[14] BloombergNEF. *EVO Report 2023 | BloombergNEF | Bloomberg Finance LP*. en-US. 2023. URL: https://about.bnef.com/electric-vehicle-outlook/ (visited on 08/10/2023).

[15] Michael Fischer, Mathew Werber, and Peter V. Schwartz. "Batteries: Higher energy density than gasoline?" In: *Energy Policy* 37.7 (July 2009), pp. 2639–2641. ISSN: 0301-4215. DOI: 10.1016/j.enpol.2009.02.030. URL: https://www.sciencedirect.com/science/article/pii/S0301421509001323 (visited on 08/31/2023).

[16] Chao-Yang Wang et al. "Fast charging of energy-dense lithium-ion batteries". en. In: *Nature* 611.7936 (Nov. 2022). Number: 7936 Publisher: Nature Publishing Group, pp. 485–490. ISSN: 1476-4687. DOI: 10.1038/s41586-022-05281-0. URL: https://www.nature.com/articles/s41586-022-05281-0 (visited on 08/10/2023).

[17] Vehicle Technologies Office. *Batteries*. en. URL: https://www.energy.gov/eere/vehicles/batteries (visited on 08/10/2023).

[18] The Faraday Institution. *The Faraday Institution*. en-GB. URL: https://www.faraday.ac.uk/ (visited on 08/10/2023).

[19] Thomas P. J. Crompton. *Battery Reference Book*. en. Google-Books-ID: QmVR7qiB5AUC. Elsevier, Mar. 2000. ISBN: 978-0-08-049995-6.

[20] Panasonic. *A simple history of batteries - Panasonic Energy Co., Ltd.* en. URL: https://www.panasonic.com/global/energy/study/academy/history.html (visited on 08/10/2023).

[21] CNRS. *Galvani and "animal electricity" · Histoire de l'électricité et du magnétisme (site Ampère)*. URL: http://www.ampere.cnrs.fr/histoire/parcours-historique/galvani-volta/galvani/eng (visited on 08/10/2023).

[22] Ronald Dell and David Anthony James Rand. *Understanding Batteries*. en. Royal Society of Chemistry, 2001. ISBN: 978-0-85404-605-8.

[23] Giuliano Pancaldi. *Volta: science and culture in the age of enlightenment*. eng. Second printing, and first paperback printing. Princeton paperbacks. Princeton Oxford: Princeton University Press, 2005. ISBN: 978-0-691-12226-7.

[24] The Nobel Prize. *The Nobel Prize in Chemistry 2019*. en-US. URL: https://www.nobelprize.org/prizes/chemistry/2019/popular-information/ (visited on 08/10/2023).

[25] John B. Goodenough and Youngsik Kim. "Challenges for Rechargeable Li Batteries". In: *Chemistry of Materials* 22.3 (Feb. 2010). Publisher: American Chemical Society, pp. 587–603. ISSN: 0897-4756. DOI: 10.1021/cm901452z. URL: https://doi.org/10.1021/cm901452z (visited on 08/15/2023).

[26] Allen J. Bard and Larry R. Faulkner. *Electrochemical methods: fundamentals and applications*. 2nd ed. New York: Wiley, 2001. ISBN: 978-0-471-04372-0.

[27] Shengshui Zhang et al. "Understanding Solid Electrolyte Interface Film Formation on Graphite Electrodes". en. In: *Electrochemical and Solid-State Letters* 4.12 (Oct. 2001). Publisher: IOP Publishing, A206. ISSN: 1944-8775. DOI: 10.1149/1.1414946. URL: https://iopscience.iop.org/article/10.1149/1.1414946/meta (visited on 08/15/2023).

[28] Feixiang Wu, Joachim Maier, and Yan Yu. "Guidelines and trends for next-generation rechargeable lithium and lithium-ion batteries". en. In: *Chemical Society Reviews* 49.5 (Mar. 2020). Publisher: The Royal Society of Chemistry, pp. 1569–1614. ISSN: 1460-4744. DOI: 10.1039/C7CS00863E. URL: https://pubs.rsc.org/en/content/articlelanding/2020/cs/c7cs00863e (visited on 08/10/2023).

[29] James T. Frith, Matthew J. Lacey, and Ulderico Ulissi. "A non-academic perspective on the future of lithium-based batteries". en. In: *Nature Communications* 14.1 (Jan. 2023). Number: 1 Publisher: Nature Publishing Group, p. 420. ISSN: 2041-1723. DOI: 10.1038/s41467-023-35933-2. URL: https://www.nature.com/articles/s41467-023-35933-2 (visited on 08/11/2023).

[30] Arumugam Manthiram. "A reflection on lithium-ion battery cathode chemistry". en. In: *Nature Communications* 11.1 (Mar. 2020). Number: 1 Publisher: Nature Publishing Group, p. 1550. ISSN: 2041-1723. DOI: 10.1038/s41467-020-15355-0. URL: https://www.nature.com/articles/s41467-020-15355-0 (visited on 08/16/2023).

[31] Richard Schmuch et al. "Performance and cost of materials for lithium-based rechargeable automotive batteries". en. In: *Nature Energy* 3.4 (Apr. 2018). Number: 4 Publisher: Nature Publishing Group, pp. 267–278. ISSN: 2058-7546. DOI: 10.1038/s41560-018-0107-2. URL: https://www.nature.com/articles/s41560-018-0107-2 (visited on 08/10/2023).

[32] Matthew Sadd et al. "Investigating microstructure evolution of lithium metal during plating and stripping via operando X-ray tomographic microscopy". en. In: *Nature Communications* 14.1 (Feb. 2023). Number: 1 Publisher: Nature Publishing Group, p. 854. ISSN: 2041-1723. DOI: 10.1038/s41467-023-36568-z. URL: https://www.nature.com/articles/s41467-023-36568-z (visited on 08/15/2023).

[33] Patrick S. Grant et al. "Roadmap on Li-ion battery manufacturing research". en. In: *Journal of Physics: Energy* 4.4 (Nov. 2022). Publisher: IOP Publishing, p. 042006. ISSN: 2515-7655. DOI: 10.1088/2515-7655/ac8e30. URL: https://dx.doi.org/10.1088/2515-7655/ac8e30 (visited on 08/11/2023).

[34] Arno Kwade et al. "Current status and challenges for automotive battery production technologies". en. In: *Nature Energy* 3.4 (Apr. 2018). Number: 4 Publisher: Nature Publishing Group, pp. 290–300. ISSN: 2058-7546. DOI: 10.1038/s41560-018-0130-3. URL: https://www.nature.com/articles/s41560-018-0130-3 (visited on 08/11/2023).

[35] CRC Press. *CRC Handbook of Chemistry and Physics 104th Edition*. URL: https://hbcp.chemnetbase.com/contents/ContentsSearch.xhtml?dswid=3 (visited on 08/11/2023).

[36] MatWeb. *Aluminum, Al*. URL: https://www.matweb.com/search/DataSheet.aspx?MatGUID=0cd1edf33ac145ee93a0aa6fc666c0e0 (visited on 08/31/2023).

[37] Seung-Taek Myung, Yashiro Hitoshi, and Yang-Kook Sun. "Electrochemical behavior and passivation of current collectors in lithium-ion batteries". en. In: *Journal of Materials Chemistry* 21.27 (June 2011). Publisher: The Royal Society of Chemistry, pp. 9891–9911. ISSN: 1364-5501. DOI: 10.1039/C0JM04353B. URL: https://pubs.rsc.org/en/content/articlelanding/2011/jm/c0jm04353b (visited on 08/11/2023).

[38] MatWeb. *Copper, Cu; Annealed*. URL: https://www.matweb.com/search/DataSheet.aspx?MatGUID=9aebe83845c04c1db5126fada6f76f7e (visited on 08/31/2023).

[39] Jie Xiao et al. "From laboratory innovations to materials manufacturing for lithium-based batteries". en. In: *Nature Energy* 8.4 (Apr. 2023). Number: 4 Publisher: Nature Publishing Group, pp. 329–339. ISSN: 2058-7546. DOI: 10.1038/s41560-023-01221-y. URL: https://www.nature.com/articles/s41560-023-01221-y (visited on 08/11/2023).

[40] Xiaosong Huang. "Separator technologies for lithium-ion batteries". en. In: *Journal of Solid State Electrochemistry* 15.4 (Apr. 2011), pp. 649–662. ISSN: 1433-0768. DOI: 10.1007/s10008-010-1264-9. URL: https://doi.org/10.1007/s10008-010-1264-9 (visited on 08/11/2023).

[41] Marie Francine Lagadec, Raphael Zahn, and Vanessa Wood. "Characterization and performance evaluation of lithium-ion battery separators". en. In: *Nature Energy* 4.1 (Jan. 2019). Number: 1 Publisher: Nature Publishing Group, pp. 16–25. ISSN: 2058-7546. DOI: 10.1038/s41560-018-0295-9. URL: https://www.nature.com/articles/s41560-018-0295-9 (visited on 08/31/2023).

[42] Xinghui Zhang et al. "A review on thermal management of lithium-ion batteries for electric vehicles". en. In: *Energy* 238 (Jan. 2022), p. 121652. ISSN: 0360-5442. DOI: 10.1016/j.energy.2021.121652. URL: https://www.sciencedirect.com/science/article/pii/S0360544221019009 (visited on 08/11/2023).

[43] F. Brosa Planella et al. "A continuum of physics-based lithium-ion battery models reviewed". en. In: *Progress in Energy* 4.4 (July 2022). Publisher: IOP Publishing, p. 042003. ISSN: 2516-1083. DOI: 10.1088/2516-1083/ac7d31. URL: https://dx.doi.org/10.1088/2516-1083/ac7d31 (visited on 08/11/2023).

[44] A. A. Wang et al. "Review of parameterisation and a novel database (LiionDB) for continuum Li-ion battery models". en. In: *Progress in Energy* 4.3 (May 2022). Publisher: IOP Publishing, p. 032004. ISSN: 2516-1083. DOI: 10.1088/2516-1083/ac692c. URL: https://dx.doi.org/10.1088/2516-1083/ac692c (visited on 08/11/2023).

[45] Zhiqiang Chen et al. "Porous Electrode Modeling and its Applications to Li-Ion Batteries". en. In: *Advanced Energy Materials* 12.32 (2022). _eprint: https://onlinelibrary.wiley.com/doi/p
p. 2201506. ISSN: 1614-6840. DOI: 10.1002/aenm.202201506. URL: https://onlinelibrary.wiley.com/doi/abs/10.1002/aenm.202201506 (visited on 08/11/2023).

[46] COMSOL. *Modeling Electrochemical Reactions*. URL: https://doc.comsol.com/5.6/doc/com.comsol.help.battery/battery_ug_modeling.05.08.html#654059 (visited on 08/31/2023).

[47] Donal P. Finegan et al. "Machine-Learning-Driven Advanced Characterization of Battery Electrodes". In: *ACS Energy Letters* 7.12 (Dec. 2022). Publisher: American Chemical Society, pp. 4368–4378. DOI: 10.1021/acsenergylett.2c01996. URL: https://doi.org/10.1021/acsenergylett.2c01996 (visited on 08/16/2023).

[48] Yuliang Cao et al. "Bridging the academic and industrial metrics for next-generation practical batteries". en. In: *Nature Nanotechnology* 14.3 (Mar. 2019). Number: 3 Publisher: Nature Publishing Group, pp. 200–207. ISSN: 1748-3395. DOI: 10.1038/s41565-019-0371-8. URL: https://www.nature.com/articles/s41565-019-0371-8 (visited on 08/11/2023).

[49] About:Energy. *About:Energy | Unlock the potential of battery technology*. en. URL: https://www.aboutenergy.io (visited on 08/11/2023).

[50] Michael J. Lain, James Brandon, and Emma Kendrick. "Design Strategies for High Power vs. High Energy Lithium Ion Cells". en. In: *Batteries* 5.4 (Dec. 2019). Number: 4 Publisher: Multidisciplinary Digital Publishing Institute, p. 64. ISSN: 2313-0105. DOI: 10.3390/batteries5040064. URL: https://www.mdpi.com/2313-0105/5/4/64 (visited on 08/16/2023).

[51] Chang-Hui Chen et al. "Development of Experimental Techniques for Parameterization of Multi-scale Lithium-ion Battery Models". en. In: *Journal of The Electrochemical Society* 167.8 (May 2020). Publisher: IOP Publishing, p. 080534. ISSN: 1945-7111. DOI: 10.1149/1945-7111/ab9050. URL: https://dx.doi.org/10.1149/1945-7111/ab9050 (visited on 08/11/2023).

[52] Christoph Neef and Fraunhofer Institute for Systems and Innovation Research. *Development perspectives for lithium-ion battery cell formats*. en. Dec. 2022. URL: https://www.isi.fraunhofer.de/en/blog/themen/batterie-update/lithium-ionen-batteriezellen-entwicklung-batteriezellformate.html (visited on 08/16/2023).

[53] T. G. Tranter et al. "Communication—Prediction of Thermal Issues for Larger Format 4680 Cylindrical Cells and Their Mitigation with Enhanced Current Collection". en. In: *Journal of The Electrochemical Society* 167.16 (Dec. 2020). Publisher: IOP Publishing, p. 160544. ISSN: 1945-7111. DOI: 10.1149/1945-7111/abd44f. URL: https://dx.doi.org/10.1149/1945-7111/abd44f (visited on 08/15/2023).

[54] Zhiqiang Chen et al. "Overpotential analysis of graphite-based Li-ion batteries seen from a porous electrode modeling perspective". en. In: *Journal of Power Sources* 509 (Oct. 2021), p. 230345. ISSN: 0378-7753. DOI: 10.1016/j.jpowsour.2021.230345. URL: https://www.sciencedirect.com/science/article/pii/S0378775321008570 (visited on 08/11/2023).

[55] Changbao Zhu et al. "The nanoscale circuitry of battery electrodes". In: *Science* 358.6369 (Dec. 2017). Publisher: American Association for the Advancement of Science, eaao2808. DOI: 10.1126/science.aao2808. URL: https://www.science.org/doi/10.1126/science.aao2808 (visited on 08/16/2023).

[56] Guinevere A. Giffin. "The role of concentration in electrolyte solutions for non-aqueous lithium-based batteries". en. In: *Nature Communications* 13.1 (Sept. 2022). Number: 1 Publisher: Nature Publishing Group, p. 5250. ISSN: 2041-1723. DOI: 10.1038/s41467-022-32794-z. URL: https://www.nature.com/articles/s41467-022-32794-z (visited on 08/31/2023).

[57] Matthew J. Lacey. *Transport and transference in battery electrolytes*. 2020. URL: http://lacey.se/science/transference/ (visited on 08/31/2023).

[58] Michael Quarti and Wolfgang G. Bessler. "Model Based Overpotential Deconvolution, Partial Impedance Spectroscopy, and Sensitivity Analysis of a Lithium-Ion Cell with Blend Cathode". en. In: *Energy Technology* 9.6 (2021). _eprint: https://onlinelibrary.wiley.com/doi/ p. 2001122. ISSN: 2194-4296. DOI: 10.1002/ente.202001122. URL: https://onlinelibrary.wiley.com/doi/abs/10.1002/ente.202001122 (visited on 11/27/2023).

[59] Manuel Weiss et al. "Fast Charging of Lithium-Ion Batteries: A Review of Materials Aspects". en. In: *Advanced Energy Materials* 11.33 (2021). _eprint: https://onlinelibrary.wiley.com/doi p. 2101126. ISSN: 1614-6840. DOI: 10.1002/aenm.202101126. URL: https://onlinelibrary.wiley.com/doi/abs/10.1002/aenm.202101126 (visited on 08/11/2023).

[60] Yongxiu Chen et al. "Revealing the rate-limiting electrode of lithium batteries at high rates and mass loadings". In: *Chemical Engineering Journal* 450 (Dec. 2022), p. 138275. ISSN: 1385-8947. DOI: 10.1016/j.cej.2022.138275. URL: https://www.sciencedirect.com/science/article/pii/S1385894722037585 (visited on 08/24/2023).

[61] Solvionic. *1M LiPF6 in EC:DMC (1:1 vol.%) 99.9%*. en. URL: https://en.solvionic.com/products/1m-lipf6-in-ec-dmc-1-1-vol.-99.9 (visited on 08/11/2023).

[62] Zhengyu Ju et al. "Towards fast-charging high-energy lithium-ion batteries: From nano- to micro-structuring perspectives". In: *Chemical Engineering Journal* 454 (Feb. 2023), p. 140003. ISSN: 1385-8947. DOI: 10.1016/j.cej.2022.140003. URL: https://www.sciencedirect.com/science/article/pii/S1385894722054833 (visited on 08/25/2023).

[63] Xuekun Lu et al. "3D microstructure design of lithium-ion battery electrodes assisted by X-ray nano-computed tomography and modelling". en. In: *Nature Communications* 11.1 (Apr. 2020). Number: 1 Publisher: Nature Publishing Group, p. 2079. ISSN: 2041-1723. DOI: 10.1038/s41467-020-15811-x. URL: https://www.nature.com/articles/s41467-020-15811-x (visited on 06/18/2023).

[64] Yijun Chen et al. "Toward High-Areal-Capacity Electrodes for Lithium and Sodium Ion Batteries". en. In: *Advanced Energy Materials* 12.44 (2022). _eprint: https://onlinelibrary.wiley.com/ p. 2201834. ISSN: 1614-6840. DOI: 10.1002/aenm.202201834. URL: https://onlinelibrary.wiley.com/doi/abs/10.1002/aenm.202201834 (visited on 08/25/2023).

[65] Pengcheng Zhu, Peter R. Slater, and Emma Kendrick. "Insights into architecture, design and manufacture of electrodes for lithium-ion batteries". en. In: *Materials & Design* 223 (Nov. 2022), p. 111208. ISSN: 0264-1275. DOI: 10.1016/j.matdes.2022.111208. URL: https://www.sciencedirect.com/science/article/pii/S0264127522008309 (visited on 06/18/2023).

[66] Adam M. Boyce et al. "Design of Scalable, Next-Generation Thick Electrodes: Opportunities and Challenges". In: *ACS Nano* 15.12 (Dec. 2021). Publisher: American Chemical Society, pp. 18624–18632. ISSN: 1936-0851. DOI: 10.1021/acsnano.1c09687. URL: https://doi.org/10.1021/acsnano.1c09687 (visited on 08/16/2023).

[67] David J. Arnot et al. "Thick Electrode Design for Facile Electron and Ion Transport: Architectures, Advanced Characterization, and Modeling". In: *Accounts of Materials Research* 3.4 (Apr. 2022). Publisher: American Chemical Society, pp. 472–483. DOI: 10.1021/accountsmr.1c00281. URL: https://doi.org/10.1021/accountsmr.1c00281 (visited on 08/24/2023).

[68] Hui Zhao et al. "A Convenient and Versatile Method To Control the Electrode Microstructure toward High-Energy Lithium-Ion Batteries". In: *Nano Letters* 16.7 (July 2016). Publisher: American Chemical Society, pp. 4686–4690. ISSN: 1530-6984. DOI: 10.1021/acs.nanolett.6b02156. URL: https://doi.org/10.1021/acs.nanolett.6b02156 (visited on 08/24/2023).

[69] Wenwen Deng et al. "Constructing Gradient Porous Structure in Thick Li4Ti5O12 Electrode for High-Energy and Stable Lithium-Ion Batteries". In: *ACS Sustainable Chemistry & Engineering* 8.46 (Nov. 2020). Publisher: American Chemical Society, pp. 17062–17068. DOI: 10.1021/acssuschemeng.0c04716. URL: https://doi.org/10.1021/acssuschemeng.0c04716 (visited on 08/24/2023).

[70] J. S. Sander et al. "High-performance battery electrodes via magnetic templating". en. In: *Nature Energy* 1.8 (July 2016). Number: 8 Publisher: Nature Publishing Group, pp. 1–7. ISSN: 2058-7546. DOI: 10.1038/nenergy.2016.99. URL: https://www.nature.com/articles/nenergy201699 (visited on 08/24/2023).

[71] Dominika Gastol et al. "Microstructural design of printed graphite electrodes for lithium-ion batteries". In: *Materials & Design* 205 (July 2021), p. 109720. ISSN: 0264-1275. DOI: 10.1016/j.matdes.2021.109720. URL: https://www.sciencedirect.com/science/article/pii/S0264127521002720 (visited on 08/24/2023).

[72] Boris Bitsch et al. "Capillary suspensions as beneficial formulation concept for high energy density Li-ion battery electrodes". In: *Journal of Power Sources* 328 (Oct. 2016), pp. 114–123. ISSN: 0378-7753. DOI: 10.1016/j.jpowsour.2016.07.102. URL: https://www.sciencedirect.com/science/article/pii/S0378775316309806 (visited on 08/24/2023).

[73] Lei-Lei Lu et al. "Wood-Inspired High-Performance Ultrathick Bulk Battery Electrodes". eng. In: *Advanced Materials (Deerfield Beach, Fla.)* 30.20 (May 2018), e1706745. ISSN: 1521-4095. DOI: 10.1002/adma.201706745.

[74] Xiao Zhang et al. "Promoting Transport Kinetics in Li-Ion Battery with Aligned Porous Electrode Architectures". In: *Nano Letters* 19.11 (Nov. 2019). Publisher: American Chemical Society, pp. 8255–8261. ISSN: 1530-6984. DOI: 10.1021/acs.nanolett.9b03824. URL: https://doi.org/10.1021/acs.nanolett.9b03824 (visited on 08/24/2023).

[75] Brindha Moorthy et al. "Ice-Templated Free-Standing Reduced Graphene Oxide for Dendrite-Free Lithium Metal Batteries". In: *ACS Applied Energy Materials* 3.11 (Nov. 2020). Publisher: American Chemical Society, pp. 11053–11060. DOI: 10.1021/acsaem.0c01946. URL: https://doi.org/10.1021/acsaem.0c01946 (visited on 08/24/2023).

[76] Shuping Li et al. "Unveiling low-tortuous effect on electrochemical performance toward ultrathick LiFePO4 electrode with 100 mg cm-2 area loading". In: *Journal of Power Sources* 515 (Dec. 2021), p. 230588. ISSN: 0378-7753. DOI: 10.1016/j.jpowsour.2021.230588. URL: https://www.sciencedirect.com/science/article/pii/S0378775321010867 (visited on 08/24/2023).

[77] Chang-Jun Bae et al. "Design of Battery Electrodes with Dual-Scale Porosity to Minimize Tortuosity and Maximize Performance". In: *Advanced Materials* 25.9 (2013). _eprint: https://onlinelibrary.wiley.com/doi/pdf/10.1002/adma.201204055, pp. 1254–1258. ISSN: 1521-4095. DOI: 10.1002/adma.201204055. URL: https://onlinelibrary.wiley.com/doi/abs/10.1002/adma.201204055 (visited on 08/25/2023).

[78] Corie L. Cobb and Scott E. Solberg. "Communication—Analysis of Thick Co-Extruded Cathodes for Higher-Energy-and-Power Lithium-Ion Batteries". en. In: *Journal of The Electrochemical Society* 164.7 (Apr. 2017). Publisher: IOP Publishing, A1339. ISSN: 1945-7111. DOI: 10.1149/2.0101707jes. URL: https://iopscience.iop.org/article/10.1149/2.0101707jes/meta (visited on 08/25/2023).

[79] C.L. Cobb and M. Blanco. "Modeling mass and density distribution effects on the performance of co-extruded electrodes for high energy density lithium-ion batteries". English. In: *Journal of Power Sources* 249 (2014), pp. 357–366. ISSN: 0378-7753. DOI: 10.1016/j.jpowsour.2013.10.084.

[80] Victoria G. Rocha et al. "Direct ink writing advances in multi-material structures for a sustainable future". en. In: *Journal of Materials Chemistry A* 8.31 (Aug. 2020). Publisher: The Royal Society of Chemistry, pp. 15646–15657. ISSN: 2050-7496. DOI: 10.1039/D0TA04181E. URL: https://pubs.rsc.org/en/content/articlelanding/2020/ta/d0ta04181e (visited on 08/24/2023).

[81] Jiwei Wang et al. "Toward High Areal Energy and Power Density Electrode for Li-Ion Batteries via Optimized 3D Printing Approach". In: *ACS Applied Materials & Interfaces* 10.46 (Nov. 2018). Publisher: American Chemical Society, pp. 39794–39801. ISSN: 1944-8244. DOI: 10.1021/acsami.8b14797. URL: https://doi.org/10.1021/acsami.8b14797 (visited on 08/25/2023).

[82] Sang Ho Lee et al. "Spray printing of self-assembled porous structures for high power battery electrodes". en. In: *Journal of Materials Chemistry A* 6.27 (July 2018). Publisher: The Royal Society of Chemistry, pp. 13133–13141. ISSN: 2050-7496. DOI: 10.1039/C8TA02920B. URL: https://pubs.rsc.org/en/content/articlelanding/2018/ta/c8ta02920b (visited on 08/25/2023).

[83] S.H. Lee et al. "Spray printing and optimization of anodes and cathodes for high performance Li-Ion batteries". English. In: *Electrochimica Acta* 292 (2018), pp. 546–557. ISSN: 0013-4686. DOI: 10.1016/j.electacta.2018.09.132.

[84] Sang Ho Lee, Colin Johnston, and Patrick S. Grant. "Scalable, Large-Area Printing of Pore-Array Electrodes for Ultrahigh Power Electrochemical Energy Storage". In: *ACS Applied Materials & Interfaces* 11.41 (Oct. 2019). Publisher: American Chemical Society, pp. 37859–37866. ISSN: 1944-8244. DOI: 10.1021/acsami.9b14478. URL: https://doi.org/10.1021/acsami.9b14478 (visited on 08/25/2023).

[85] Sang Ho Lee et al. "Spray-Printed and Self-Assembled Honeycomb Electrodes of Silicon-Decorated Carbon Nanofibers for Li-Ion Batteries". In: *ACS Applied Materials & Interfaces* 11.1 (Jan. 2019). Publisher: American Chemical Society, pp. 603–612. ISSN: 1944-8244. DOI: 10.1021/acsami.8b15164. URL: https://doi.org/10.1021/acsami.8b15164 (visited on 08/25/2023).

[86] Johannes Kriegler et al. "Enhanced performance and lifetime of lithium-ion batteries by laser structuring of graphite anodes". en. In: *Applied Energy* 303 (Dec. 2021), p. 117693. ISSN: 0306-2619. DOI: 10.1016/j.apenergy.2021.117693. URL: https://www.sciencedirect.com/science/article/pii/S0306261921010539 (visited on 08/11/2023).

[87] Jan B. Habedank et al. "Femtosecond laser structuring of graphite anodes for improved lithium-ion batteries: Ablation characteristics and process design". In: *Journal of Laser Applications* 30.3 (June 2018), p. 032205. ISSN: 1042-346X. DOI: 10.2351/1.5040611. URL: https://doi.org/10.2351/1.5040611 (visited on 08/11/2023).

[88] Wilhelm Pfleging. "Recent progress in laser texturing of battery materials: a review of tuning electrochemical performances, related material development, and prospects for large-scale manufacturing". en. In: *International Journal of Extreme Manufacturing* 3.1 (Dec. 2020). Publisher: IOP Publishing, p. 012002. ISSN: 2631-7990. DOI: 10.1088/2631-7990/abca84. URL: https://dx.doi.org/10.1088/2631-7990/abca84 (visited on 08/11/2023).

[89] Wilhelm Pfleging. "A review of laser electrode processing for development and manufacturing of lithium-ion batteries". en. In: *Nanophotonics* 7.3 (Mar. 2018). Publisher: De Gruyter, pp. 549–573. ISSN: 2192-8614. DOI: 10.1515/nanoph-2017-0044. URL: https://www.degruyter.com/document/doi/10.1515/nanoph-2017-0044/html (visited on 08/11/2023).

[90] Juliette Billaud et al. "Magnetically aligned graphite electrodes for high-rate performance Li-ion batteries | Nature Energy". In: *Nature Energy* 1.8 (July 2016), p. 16097. ISSN: 2058-7546. DOI: 10.1038/nenergy.2016.97. URL: https://www.nature.com/articles/nenergy201697 (visited on 06/13/2023).

[91] Chuan Cheng et al. "Micro-scale graded electrodes for improved dynamic and cycling performance of Li-ion batteries". In: *Journal of Power Sources* 413 (Feb. 2019), pp. 59–67. ISSN: 0378-7753. DOI: 10.1016/j.jpowsour.2018.12.021. URL: https://www.sciencedirect.com/science/article/pii/S0378775318313727 (visited on 09/02/2023).

[92] Robert Morasch, Bharatkumar Suthar, and Hubert A. Gasteiger. "Simple Way of Making Free-Standing Battery Electrodes and their Use in Enabling Half-Cell Impedance Measurements via µ-Reference Electrode". en. In: *Journal of The Electrochemical Society* 167.10 (June 2020). Publisher: IOP Publishing, p. 100540. ISSN: 1945-7111. DOI: 10.1149/1945-7111/ab9b93. URL: https://dx.doi.org/10.1149/1945-7111/ab9b93 (visited on 08/24/2023).

[93] S. Zhao et al. "Graphene-based free-standing bendable films: designs, fabrications, and applications". In: *Materials Today Advances* 6 (June 2020), p. 100060. ISSN: 2590-0498. DOI: 10.1016/j.mtadv.2020.100060. URL: https://www.sciencedirect.com/science/article/pii/S2590049820300072 (visited on 08/24/2023).

[94] Samantha N. Lauro, James N. Burrow, and C. Buddie Mullins. "Restructuring the lithium-ion battery: A perspective on electrode architectures". In: *eScience* 3.4 (Aug. 2023), p. 100152. ISSN: 2667-1417. DOI: 10.1016/j.esci.2023.100152. URL: https://www.sciencedirect.com/science/article/pii/S2667141723000812 (visited on 08/24/2023).

[95] M. Baunach et al. "Delamination behavior of lithium-ion battery anodes: Influence of drying temperature during electrode processing". In: *Drying Technology* 34.4 (Mar. 2016). Publisher: Taylor & Francis _eprint: https://doi.org/10.1080/07373937.2015.1060497, pp. 462–473. ISSN: 0737-3937. DOI: 10.1080/07373937.2015.1060497. URL: https://doi.org/10.1080/07373937.2015.1060497 (visited on 08/24/2023).

[96] Andrzej P. Nowak et al. "Lignin-based carbon fibers for renewable and multifunctional lithium-ion battery electrodes". en. In: *Holzforschung* 72.2 (Feb. 2018). Publisher: De Gruyter, pp. 81–90. ISSN: 1437-434X. DOI: 10.1515/hf-2017-0044. URL: https://www.degruyter.com/document/doi/10.1515/hf-2017-0044/html?lang=en (visited on 08/24/2023).

[97] R. Yazami, K. Zaghib, and M. Deschamps. "Carbon fibres and natural graphite as negative electrodes for lithium ion-type batteries". In: *Journal of Power Sources* 52.1 (Nov. 1994), pp. 55–59. ISSN: 0378-7753. DOI: 10.1016/0378-7753(94)01933-9. URL: https://www.sciencedirect.com/science/article/pii/0378775394019339 (visited on 08/24/2023).

[98] James F. Snyder, Emma L. Wong, and Clifford W. Hubbard. "Evaluation of Commercially Available Carbon Fibers, Fabrics, and Papers for Potential Use in Multifunctional Energy Storage Applications". en. In: *Journal of The Electrochemical Society* 156.3 (Jan. 2009). Publisher: IOP Publishing, A215. ISSN: 1945-7111. DOI: 10.1149/1.3065070. URL: https://iopscience.iop.org/article/10.1149/1.3065070/meta (visited on 08/24/2023).

[99] Indrajeet V. Thorat et al. "Quantifying tortuosity in porous Li-ion battery materials". In: *Journal of Power Sources* 188.2 (Mar. 2009), pp. 592–600. ISSN: 0378-7753. DOI: 10.1016/j.jpowsour.2008.12.032. URL: https://www.sciencedirect.com/science/article/pii/S0378775308023574 (visited on 08/24/2023).

[100] Fezzeh Pouraghajan et al. "Quantifying Tortuosity of Porous Li-Ion Battery Electrodes: Comparing Polarization-Interrupt and Blocking-Electrolyte Methods". en. In: *Journal of The Electrochemical Society* 165.11 (Aug. 2018). Publisher: IOP Publishing, A2644. ISSN: 1945-7111. DOI: 10.1149/2.0611811jes. URL: https://iopscience.iop.org/article/10.1149/2.0611811jes/meta (visited on 08/24/2023).

[101] Chih-Hung Chen et al. "Simple way of making free-standing cathode electrodes for flexible lithium-ion batteries". en. In: *RSC Advances* 12.15 (Mar. 2022). Publisher: The Royal Society of Chemistry, pp. 9249–9255. ISSN: 2046-2069. DOI: 10.1039/D1RA08993E. URL: https://pubs.rsc.org/en/content/articlelanding/2022/ra/d1ra08993e (visited on 08/24/2023).

[102] Deborah D L Chung. *Carbon Materials: Science and Applications*. en. WORLD SCIENTIFIC, 2019. DOI: 10.1142/10487. URL: https://www.worldscientific.com/worldscibooks/10.1142/10487 (visited on 11/26/2023).

[103] S. H. Ng et al. "Single wall carbon nanotube paper as anode for lithium-ion battery". In: *Electrochimica Acta* 51.1 (Oct. 2005), pp. 23–28. ISSN: 0013-4686. DOI: 10.1016/j.electacta.2005.04.045. URL: https://www.sciencedirect.com/science/article/pii/S0013468605003373 (visited on 11/26/2023).

[104] Ali Abouimrane et al. "Non-Annealed Graphene Paper as a Binder-Free Anode for Lithium-Ion Batteries". In: *The Journal of Physical Chemistry C* 114.29 (July 2010). Publisher: American Chemical Society, pp. 12800–12804. ISSN: 1932-7447. DOI: 10.1021/jp103704y. URL: https://doi.org/10.1021/jp103704y (visited on 11/26/2023).

[105] GrafTech. *What is Grafoil*. 2002. URL: https://www.usseal.com/Grafoil/What-is-Grafoil.pdf (visited on 11/26/2023).

[106] Panasonic. *Thermal protection sheet (Graphite Sheet (PGS)/PGS applied products/NASBIS) - Panasonic*. en. URL: https://industrial.panasonic.com/ww/products/pt/pgs (visited on 08/11/2023).

[107] Guanming Yuan et al. "Polyimide-Derived Graphite Films with High Thermal Conductivity". en. In: *Polyimides*. IntechOpen, Sept. 2021. ISBN: 978-1-83969-885-9. DOI: 10.5772/intechopen.100374. URL: https://www.intechopen.com/chapters/78817 (visited on 08/11/2023).

[108] Jianyu Zhu, Jiemin Feng, and Zhansheng Guo. "Mechanical properties of commercial copper current-collector foils". en. In: *RSC Advances* 4.101 (Nov. 2014). Publisher: The Royal Society of Chemistry, pp. 57671–57678. ISSN: 2046-2069. DOI: 10.1039/C4RA07675C. URL: https://pubs.rsc.org/en/content/articlelanding/2014/ra/c4ra07675c (visited on 08/31/2023).

[109] Sachiko Nakamura et al. "Characterization of Pyrolytic Graphite Sheet: A New Type of Adsorption Substrate for Studies of Superfluid Thin Films". en. In: *Journal of Low Temperature Physics* 192.5 (Sept. 2018), pp. 330–345. ISSN: 1573-7357. DOI: 10.1007/s10909-018-1983-3. URL: https://doi.org/10.1007/s10909-018-1983-3 (visited on 08/16/2023).

[110] Sachiko Nakamura et al. "Low temperature transport properties of pyrolytic graphite sheet". en. In: *Cryogenics* 86 (Sept. 2017), pp. 118–122. ISSN: 0011-2275. DOI: 10.1016/j.cryogenics.2017.08.004. URL: https://www.sciencedirect.com/science/article/pii/S0011227517301212 (visited on 08/11/2023).

[111] Kristin Persson et al. "Lithium Diffusion in Graphitic Carbon". In: *The Journal of Physical Chemistry Letters* 1.8 (Apr. 2010). Publisher: American Chemical Society, pp. 1176–1180. DOI: 10.1021/jz100188d. URL: https://doi.org/10.1021/jz100188d (visited on 08/11/2023).

[112] Shung-Ik Lee et al. "A study of electrochemical kinetics of lithium ion in organic electrolytes". en. In: *Korean Journal of Chemical Engineering* 19.4 (July 2002), pp. 638–644. ISSN: 1975-7220. DOI: 10.1007/BF02699310. URL: https://doi.org/10.1007/BF02699310 (visited on 08/11/2023).

[113] D. Billaud, F. X. Henry, and P. Willmann. "Electrochemical synthesis of binary graphite-lithium intercalation compounds". In: *Materials Research Bulletin* 28.5 (May 1993), pp. 477–483. ISSN: 0025-5408. DOI: 10.1016/0025-5408(93)90130-6. URL: https://www.sciencedirect.com/science/article/pii/0025540893901306 (visited on 08/16/2023).

[114] Jakob Asenbauer et al. "The success story of graphite as a lithium-ion anode material – fundamentals, remaining challenges, and recent developments including silicon (oxide) composites". en. In: *Sustainable Energy & Fuels* 4.11 (2020). Publisher: Royal Society of Chemistry, pp. 5387–5416. DOI: 10.1039/D0SE00175A. URL: https://pubs.rsc.org/en/content/articlelanding/2020/se/d0se00175a (visited on 08/11/2023).

[115] S. J. Cooper et al. "TauFactor: An open-source application for calculating tortuosity factors from tomographic data". In: *SoftwareX* 5 (Jan. 2016), pp. 203–210. ISSN: 2352-7110. DOI: 10.1016/j.softx.2016.09.002. URL: https://www.sciencedirect.com/science/article/pii/S2352711016300280 (visited on 11/26/2023).

[116] Lucas Hille et al. "Influence of Laser Structuring and Calendering of Graphite Anodes on Electrode Properties and Cell Performance". en. In: *Journal of The Electrochemical Society* 169.6 (June 2022), p. 060518. ISSN: 1945-7111. DOI: 10.1149/1945-7111/ac725c. URL: https://dx.doi.org/10.1149/1945-7111/ac725c (visited on 07/24/2023).

[117] Fabian Duffner et al. "Post-lithium-ion battery cell production and its compatibility with lithium-ion cell production infrastructure". en. In: *Nature Energy* 6.2 (Feb. 2021). Number: 2 Publisher: Nature Publishing Group, pp. 123–134. ISSN: 2058-7546. DOI: 10.1038/s41560-020-00748-8. URL: https://www.nature.com/articles/s41560-020-00748-8 (visited on 08/17/2023).

[118] Heather Au et al. "A revised mechanistic model for sodium insertion in hard carbons". en. In: *Energy & Environmental Science* 13.10 (2020). Publisher: Royal Society of Chemistry, pp. 3469–3479. DOI: 10.1039/D0EE01363C. URL: https://pubs.rsc.org/en/content/articlelanding/2020/ee/d0ee01363c (visited on 08/17/2023).

[119] Christian Heubner et al. "From Active Materials to Battery Cells: A Straightforward Tool to Determine Performance Metrics and Support Developments at an Application-Relevant Level". en. In: *Advanced Energy Materials* 11.46 (2021). _eprint: https://onlinelibrary.wiley p. 2102647. ISSN: 1614-6840. DOI: 10.1002/aenm.202102647. URL: https://onlinelibrary.wiley.com/doi/abs/10.1002/aenm.202102647 (visited on 08/17/2023).

[120] Yeonguk Son et al. "Reliable protocols for calculating the specific energy and energy density of Li-Ion batteries". In: *Materials Today Energy* 21 (Sept. 2021), p. 100838. ISSN: 2468-6069. DOI: 10.1016/j.mtener.2021.100838. URL: https://www.sciencedirect.com/science/article/pii/S2468606921002033 (visited on 08/24/2023).

[121] Argonne National Laboratory. *BatPaC Model Software | Argonne National Laboratory*. en. URL: https://www.anl.gov/cse/batpac-model-software (visited on 11/26/2023).

[122] Marm Dixit et al. "SolidPAC is an interactive battery-on-demand energy density estimator for solid-state batteries". In: *Cell Reports Physical Science* 3.2 (Feb. 2022), p. 100756. ISSN: 2666-3864. DOI: 10.1016/j.xcrp.2022.100756. URL: https://www.sciencedirect.com/science/article/pii/S2666386422000236 (visited on 11/26/2023).

[123] Matthias Kuipers et al. "Development of a cell design environment for bottom-up estimation of performance parameters for lithium-ion batteries and virtual cell design – ISEA Cell & Pack Database (ICPD)". In: *Journal of Energy Storage* 72 (Nov. 2023), p. 108396. ISSN: 2352-152X. DOI: 10.1016/j.est.2023.108396. URL: https://www.sciencedirect.com/science/article/pii/S2352152X23017930 (visited on 11/26/2023).

[124] Joris Baars, Felipe Cerdas, and Oliver Heidrich. "An Integrated Model to Conduct Multi-Criteria Technology Assessments: The Case of Electric Vehicle Batteries". In: *Environmental Science & Technology* 57.12 (Mar. 2023), pp. 5056–5067. ISSN: 0013-936X. DOI: 10.1021/acs.est.2c04080. URL: https://www.ncbi.nlm.nih.gov/pmc/articles/PMC10061934/ (visited on 11/26/2023).

[125] tldr. *Tools for Learning, Design and Research*. URL: https://tldr-group.github.io/#/ (visited on 08/31/2023).

[126] COMSOL. *COMSOL Multiphysics Reference Manual*. URL: https://doc.comsol.com/6.1/docserver/#!/com.comsol.help.comsol/comsol_ref_chemicalspeciestransport.27.03.html (visited on 08/17/2023).

[127] COMSOL. *Detailed Explanation of the Finite Element Method (FEM)*. URL: https://www.comsol.com/multiphysics/finite-element-method (visited on 09/01/2023).

[128] Yu-Chuan Chien et al. "Rapid determination of solid-state diffusion coefficients in Li-based batteries via intermittent current interruption method". en. In: *Nature Communications* 14.1 (Apr. 2023). Number: 1 Publisher: Nature Publishing Group, p. 2289. ISSN: 2041-1723. DOI: 10.1038/s41467-023-37989-6. URL: https://www.nature.com/articles/s41467-023-37989-6 (visited on 08/31/2023).

[129] F. Degen et al. "Energy consumption of current and future production of lithium-ion and post lithium-ion battery cells". en. In: *Nature Energy* 8.11 (Nov. 2023). Number: 11 Publisher: Nature Publishing Group, pp. 1284–1295. ISSN: 2058-7546. DOI: 10.1038/s41560-023-01355-z. URL: https://www.nature.com/articles/s41560-023-01355-z (visited on 11/26/2023).

[130] TWI. *What are the different modes of laser drilling?* en-GB. URL: https://www.twi-global.com/technical-knowledge/faqs/faq-what-are-the-different-modes-of-laser-drilling.aspx (visited on 09/02/2023).

[131] Henrikki Pantsar et al. "High power fiber laser on-the-fly drilling of thin materials". en. In: AIP Publishing, Oct. 2011, pp. 792–797. DOI: 10.2351/1.5062328. URL: https://pubs.aip.org/lia/liacp/article/doi/10.2351/1.5062328/1002747/High-power-fiber-laser-on-the-fly-drilling-of-thin (visited on 08/25/2023).

[132] John Crank and John Crank. *The Mathematics of Diffusion*. Second Edition, Second Edition. Oxford, New York: Oxford University Press, Mar. 1979. ISBN: 978-0-19-853411-2.

Appendix A

Supplementary information

A.1 Feasibility of laser cutting pyrolytic graphite sheet

A number of a laser trials were conducted to assess the feasibility of cutting pyrolytic graphite sheet. To begin, a rectangular array of 100 µm diameter channels with 500 µm pitch were cut (Figure A.1). These channels were cut by programming the laser beam to trace a path around the perimeter of the channels. The resulting channels were successfully cut, albeit with some debris visible around the channel edges. The optical micrographs initially appeared to show a heat affected zone visible on the bottom, however scanning electron micrographs later indicated the presence of spluttered metal from the aluminium substrate used for micromachining (Figure A.2).

Next, a hexagonal array of 50 µm diameter channels with 100 µm pitch were cut. Channels were successfully cut, however there was again evidence of debris and incomplete material removal. Finally, a hexagonal array of 25 µm diameter channels with 100 µm pitch were drilled (Figure A.2). Rather than moving the laser beam around the channel perimeter, these channels were percussion drilled by holding the laser beam at a single spot for a fixed duration. As shown in Figure A.3, the drilled channels showed a flower-like morphology as the layered graphitic domains were exposed.

In summary, the initial feasibility trials successfully demonstrated laser cutting and drilling of channels in pyrolytic graphite sheet. Spluttered metal was detected on the bottom of the pyrolytic graphite sheet during these trials, and all future laser micromachining work was

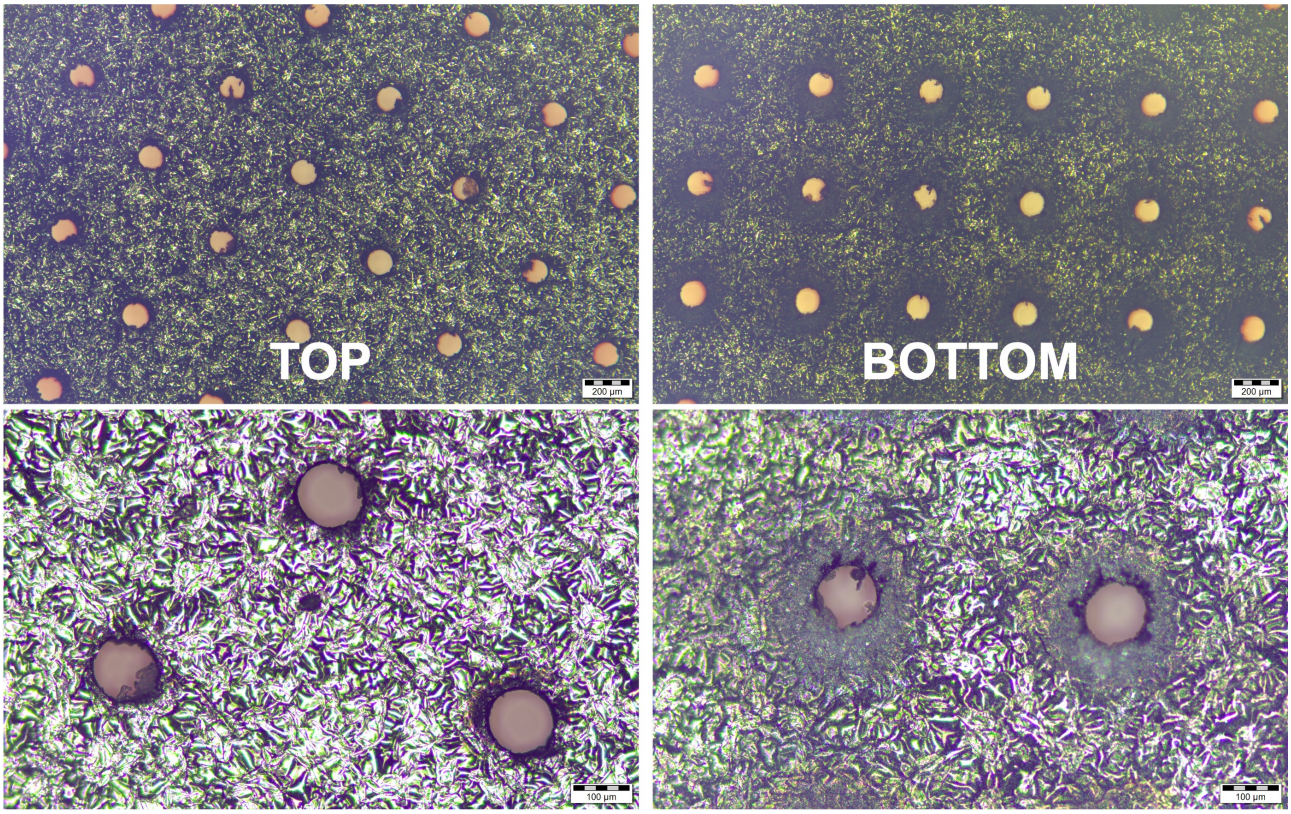


Figure A.1: Rectangular arrays of 100 µm diameter channels with 500 µm pitch were cut to check the feasibility of laser cutting pyrolytic graphite sheet. These channels were cut by programming the laser beam to trace a path around the perimeter of the channels. The resulting channels were successfully cut, albeit with some debris visible around the channel edges. The optical micrographs initially appeared to show a heat affected zone visible on the bottom, however scanning electron micrographs later indicated the presence of spluttered metal from the aluminium substrate used for micromachining (Figure A.2).

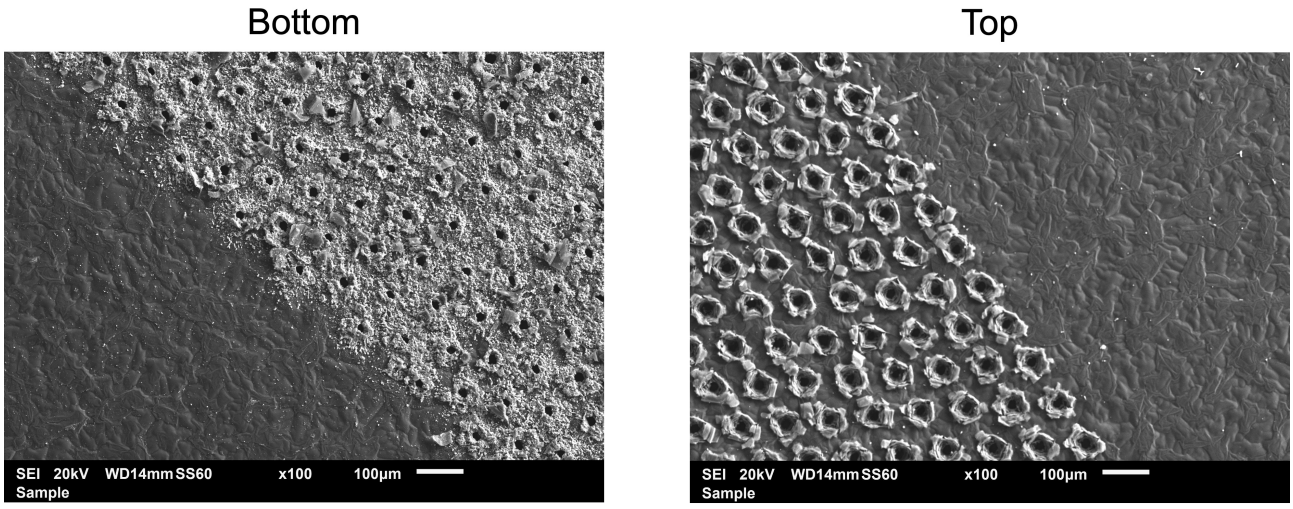


Figure A.2: Scanning electron micrographs showing a hexagonal array of 25 µm diameter channels with 100 µm pitch. Rather than moving the laser beam around the channel perimeter, these channels were percussion drilled by holding the laser beam at a single spot for a fixed duration. Spluttered metal is visible on the bottom from the aluminium substrate used for micromachining.

conducted on a graphite rather than aluminium plate.

Percussion drilling trials

As shown in Figure A.3, rather than cutting channels, percussion drilling can be used to introduce channels into a substrate with a laser. With percussion drilling, the laser is fired at a fixed location on the substrate for a specified duration of time. Each consecutive pulse removes more material and creates a deeper channel. Percussion drilling is often used for small diameter and high aspect ratio channels [130]. The channel diameter in percussion drilling is determined by the laser power and the drilling time. Further trials were therefore conducted to observe the impact of varying these two parameters on channel quality.

A 10 x 10 array of channels was drilled with drilling time and power varied along the two axes (Figure A.4). As drilling power was increased from 10% to 100% in 10% steps, the channel size increased. Conversely, as drilling time was increased from 1 ms to 10 ms in 1 ms steps, no effect on drilling performance was observed. This result may at first seem unexpected; however, if we consider that drilling time just increases the duration for which pulses are applied to a fixed spot, then the channels would be expected to get deeper but not necessarily any wider.

A second 10 x 10 array of channels was drilled with drilling time and power again varied

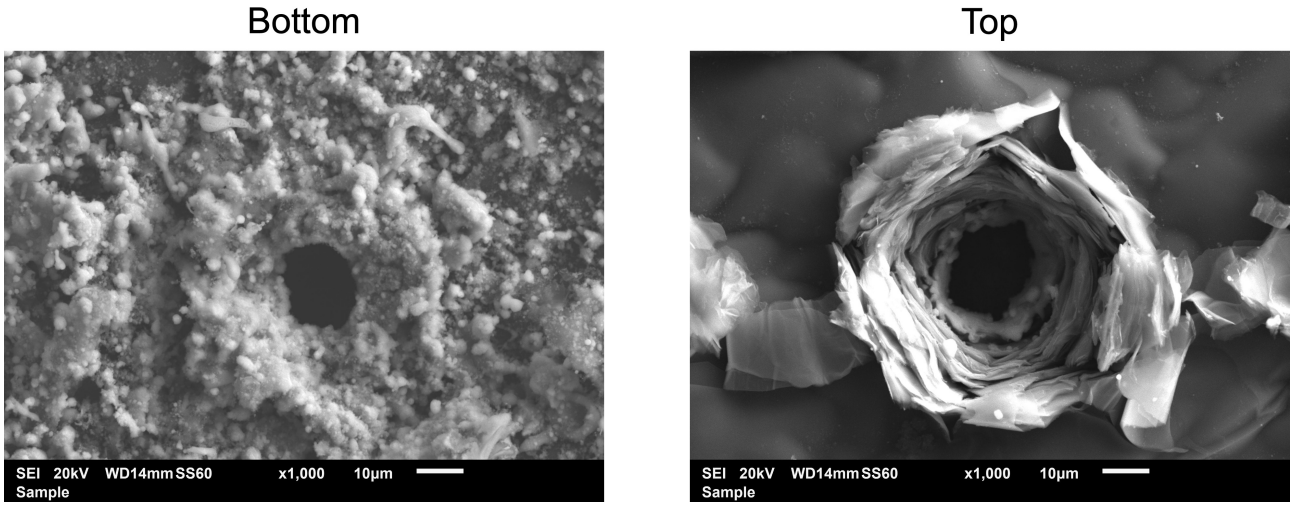


Figure A.3: Scanning electron micrographs showing 25 µm diameter percussion drilled channel. The percussion drilled channels showed a flower-like morphology as the layered graphitic domains were exposed.

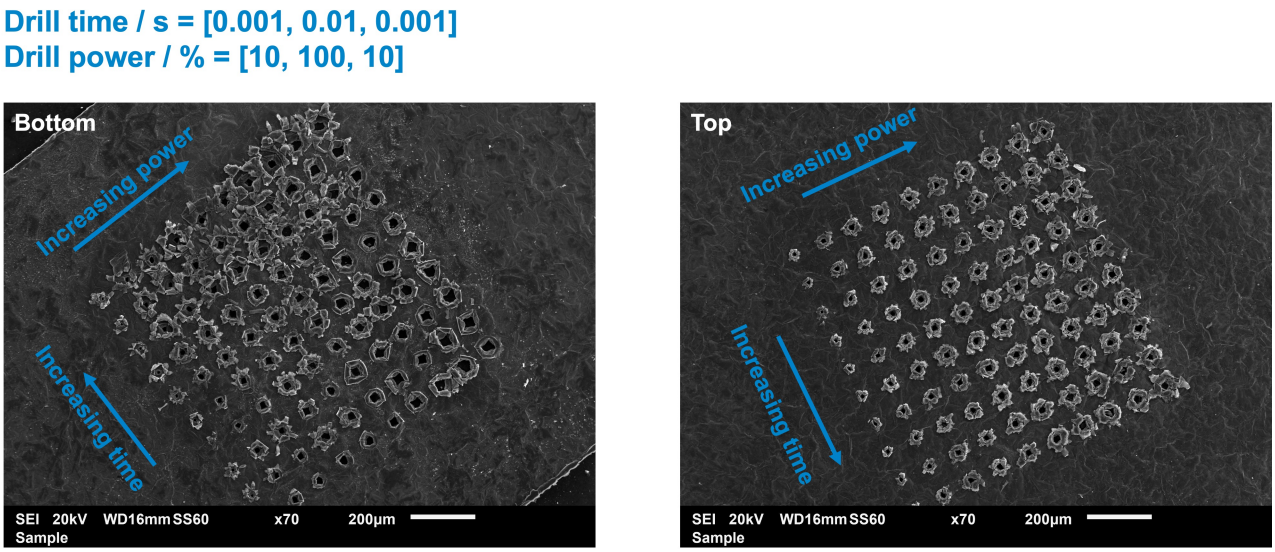


Figure A.4: A 10 x 10 array of channels was drilled with drilling time and power varied along the two axes. As drilling power was increased from 10% to 100% in 10% steps, the channel size increased. Conversely, as drilling time was increased from 1 ms to 10 ms in 1 ms steps, no effect on drilling performance was observed.

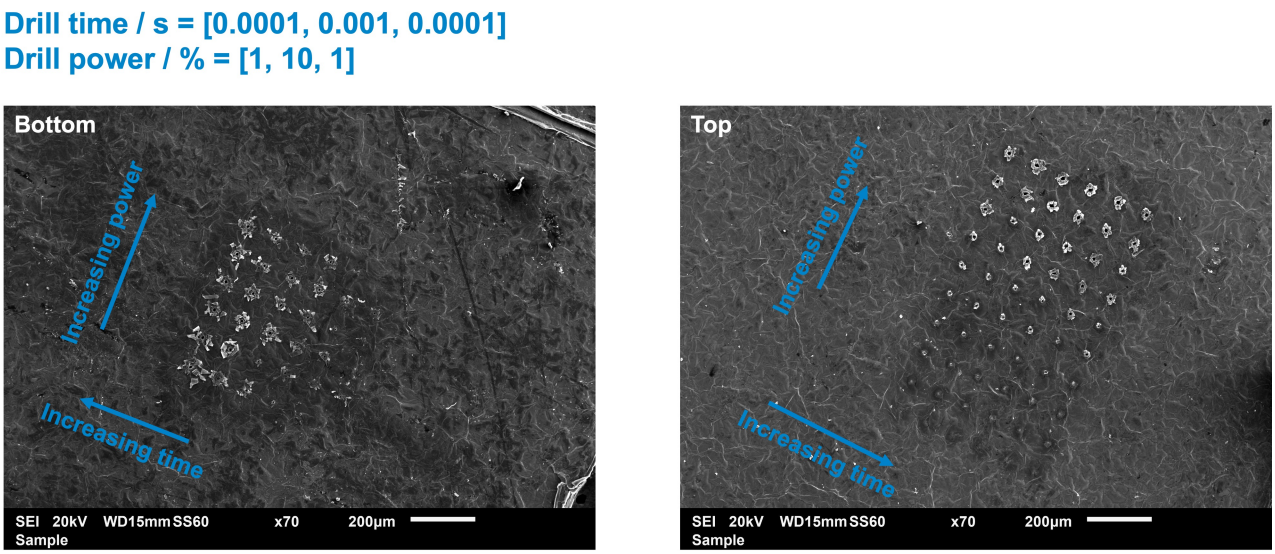


Figure A.5: A second 10 x 10 array of channels was drilled with drilling time and power again varied along the two axes, but this time lower power and drill times were used. As drilling power was increased from 1% to 10% in 1% steps, the channel size increased. As drilling time was increased from 0.1 ms to 1 ms in 0.1 ms steps, a strong effect on drilling performance was now observed. At drilling times of less than 0.5 ms, no channel was observed.

along the two axes, but this time lower drill times and drilling powers were used (Figure A.5). As drilling power was increased from 1% to 10% in 1% steps, the channel size increased. As drilling time was increased from 0.1 ms to 1 ms in 0.1 ms steps, a strong effect on drilling performance was now observed. At drilling times of less than 0.5 ms, no channel was observed.

Overall, the laser trials successfully demonstrated use of a laser to introduce through-plane channels into pyrolytic graphite sheet. Laser cutting, rather than drilling, was identified as the most suitable method of reliably producing arrays of channels with controlled channel diameter.

On-the-fly drilling trials

Previous trials investigated the introduction of channels into pyrolytic graphite sheet by either cutting or percussion drilling. Besides percussion drilling, laser drilling is often performed in "on-the-fly" mode [131]. In this mode, instead of focusing the laser on a fixed drilling location for a set amount of time, the laser is moved in a continuous sweep across the substrate, and the spacing between channels is a function of the pulse frequency and velocity (scan speed) of the laser. Each channel is therefore drilled by a single laser pulse in a single pass by default, although multiple passes can be programmed.

Significant time savings could be realised by switching from percussion to on-the-fly drilling. Pitch is determined by the pulse frequency and scan speed. Arrays of channels with different pitches and pulse power were created to explore the impact of these two parameters (Figure A.6). Arrays of 10 µm pitch channels were drilled on-the-fly using different pulse powers (100, 50, 25, 12.5, 10, 7.5 or 5 %). The area indicated by the blue square is zoomed in for the second row of images. At a pulse power of 12.5 %, channels with diameter less than 5 µm were visible on the top of the substrate but not on the bottom. Overall, on-the-fly drilling created lots of debris and was less reliable than percussion drilling or cutting.

Laser drilling hexagonal array trials

Having identified percussion drilling and cutting as the preferred modes for creating channels, these two techniques were investigated for drilling hexagonal arrays of channels as required for an electrode.

Arrays of small (5-10 µm diameter) channels with a 10 µm or 20 µm pitch were first percussion drilled (Figure A.7). The array of 20 µm pitch channels was successfully drilled, but consistency was poor. The array of 10 µm pitch channels was unsuccessful as the channels were too closely spaced. This finding highlights a key limitation of percussion drilling: it is difficult to control the channel diameter.

Laser cutting hexagonal array trials

A key advantage of laser cutting, rather than laser drilling, is that channel diameter can be controlled directly. To investigate the feasibility of cutting hexagonal arrays of channels, a series of arrays were cut (Figure A.8). Channel diameter was set as 20, 40 or 80 µm, and pitch was 1.5, 2.0 or 2.5 times the channel diameter. For each combination, a 1 mm^2 hexagonal array of channels was cut.

As channel diameter and pitch were decreased, there was a risk of the array of channels becoming too fragile. None of the arrays with 20 µm diameter channels were successfully cut. In all cases, no material was left between channels. The arrays of 40 µm channels with pitch of 100 µm or 80 µm were successfully cut, however the 60 µm pitch array at this channel size did

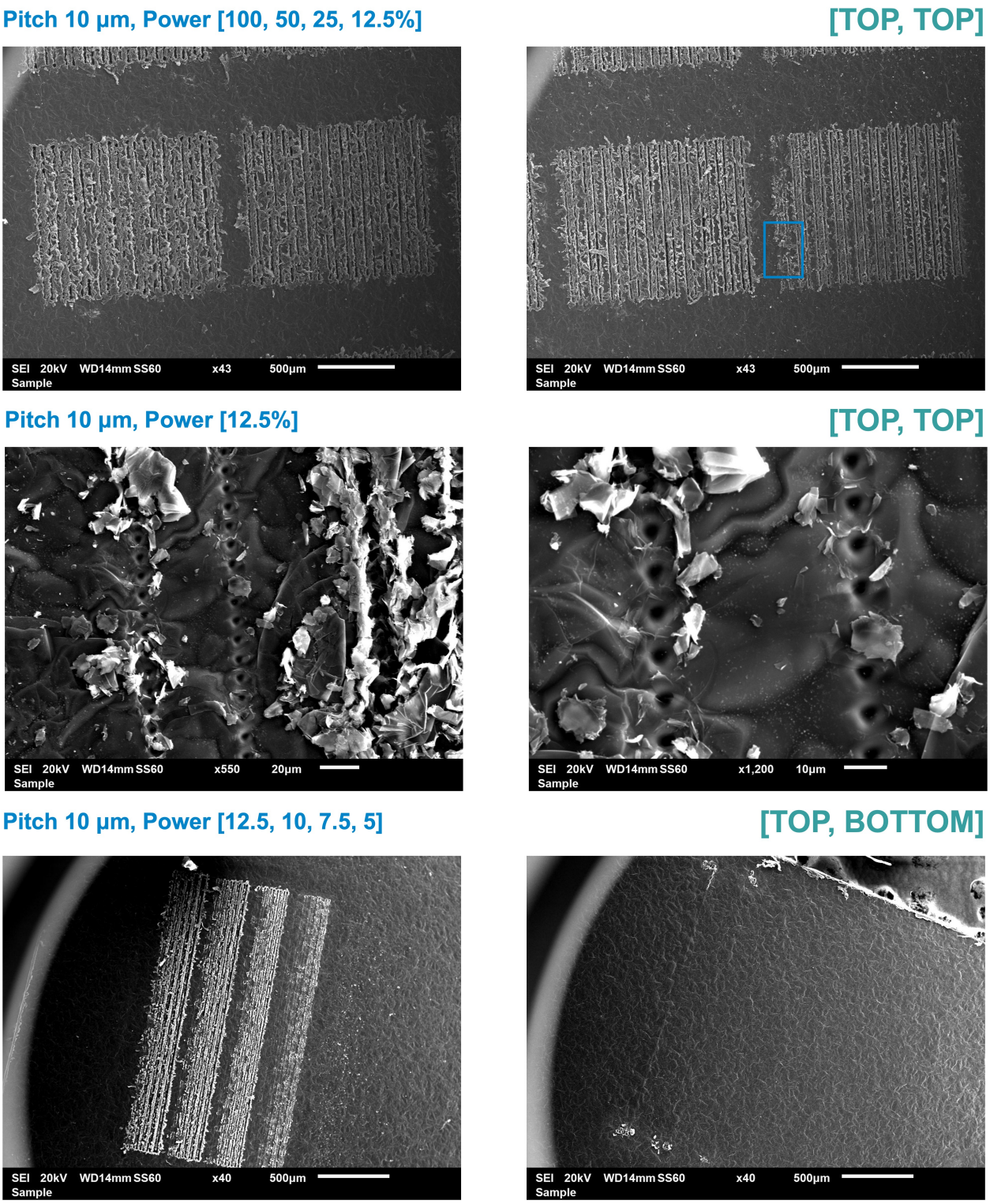


Figure A.6: Arrays were drilled to test out on-the-fly drilling. In this mode, instead of focusing the laser on a fixed drilling location for a set amount of time, the laser is moved in a continuous sweep across the substrate and the spacing between channels is a function of the pulse frequency and velocity (scan speed) of the laser. Arrays of 10 µm pitch channels were drilled on-the-fly using different pulse powers (100, 50, 25, 12.5, 10, 7.5 or 5 %). The area indicated by the blue square is zoomed in for the second row of images. At a pulse power of 12.5 %, channels with diameter less than 5 µm were visible on the top of the substrate but not on the bottom.

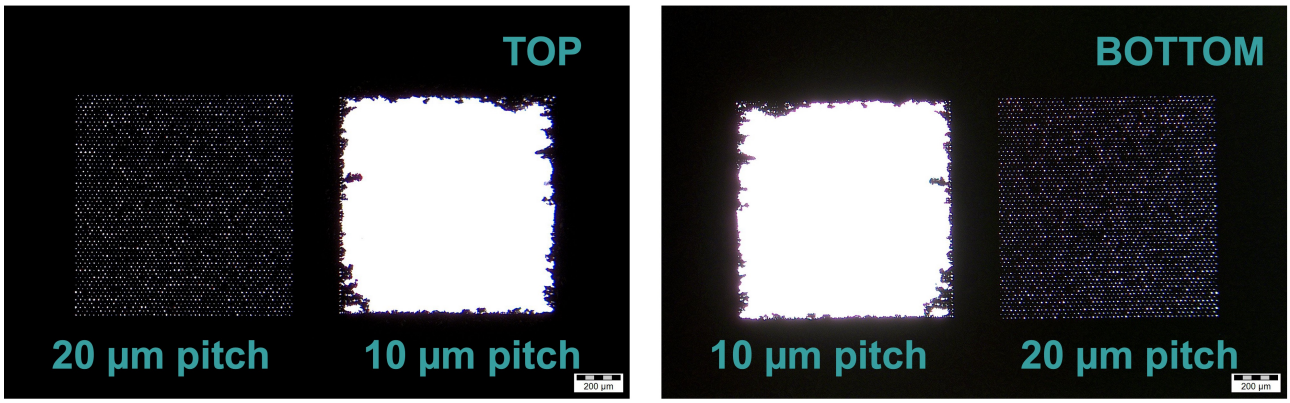


Figure A.7: Arrays of small (5-10 µm diameter) channels with a 10 µm or 20 µm pitch were percussion drilled. The array of 10 µm pitch channels was unsuccessful as the channels were too closely spaced.

not survive. All of the 80 µm channel diameter arrays were successfully cut. This experiment was repeated 6 times with the cutting speed doubled each time. Cutting speed appeared to have little impact on channel cutting.

Overall, the laser trials successfully demonstrated use of a laser to introduce through-plane channels into pyrolytic graphite sheet. Laser cutting, rather than drilling, was identified as the most suitable method of reliably producing arrays of channels with controlled channel diameter.

A.2 Planar diffusion

Batteries are typically discharged from a full state-of-charge (full lithiation of graphite in a full cell) under a constant gravimetric discharge rate. A constant gravimetric discharge rate dictates that for each gram of active material, the same amount of charge will enter or exit each second. There is therefore a constant flux of lithium ions at the active material surface, or in modelling terms, a constant flux boundary condition. Fick's second law can be used with this boundary condition (Figure A.9A) to describe the diffusion of lithium ions inside the active material and predict the concentration overpotential.

Assuming a constant value for lithium diffusivity, D, in the active material, Fick's second law for planar geometry can be used to describe the lithium ion concentration in the active material, c_i, as a function of the time, t, and distance from the active material surface, x:

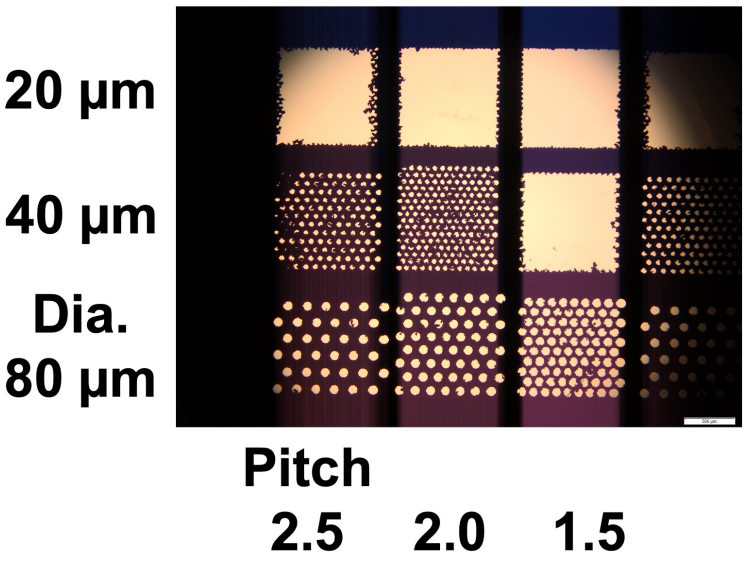


Figure A.8: To investigate the feasibility of cutting hexagonal arrays of channels, a series of arrays were cut. Channel diameter was set as 20, 40 or 80 µm, and pitch was 1.5, 2.0 or 2.5 times the channel diameter. For each combination, a 1 mm^2 hexagonal array of channels was cut. Hexagonal arrays of 80 µm diameter channels could be reliably manufactured with 200 µm, 160 µm and 120 µm channel pitch.

$$\frac{\partial c_i(x,t)}{\partial t} = D\frac{\partial^2 c_i(x,t)}{\partial^2 x} \tag{A.1}$$

with initial condition of uniform lithium concentration, c_0, throughout the active material,

$$c_i(x, t = 0) = c_0 \qquad (0 \leq x \leq l) \tag{A.2}$$

constant flux of lithium ions, F_0, at the electrode-electrolyte interface,

$$-D\frac{\partial c_i}{\partial x}\bigg|_{x=0} = F_0 \tag{A.3}$$

and no transport across the middle plane of the material due to symmetry.

$$\frac{\partial c_i}{\partial x}\bigg|_{x=l} = 0 \qquad (t \geq 0) \tag{A.4}$$

An analytical solution to Fick's second law with these boundary and initial conditions is

provided by Crank [132]:

$$C - C_0 = \frac{F_0 l}{D}\left[\frac{Dt}{l^2} + \frac{3x^2 - l^2}{6l^2} - \frac{2}{\pi^2}\sum_{n=1}^{\infty}\frac{(-1)^n}{n^2}\exp\left(-Dn^2\pi^2 t/l^2\right)\cos\frac{n\pi x}{l}\right] \tag{A.5}$$

The infinite sum in this solution can be approximated numerically, thereby allowing the concentration gradient inside the active material at any point in time to be calculated.

The flux, F_0, at the electrode-electrolyte interface will depend on the gravimetric capacity of the active material, the discharge rate being used, and the gravimetric surface area of the active material (Figure A.9A):

$$F_0 = \frac{\text{Gravimetric capacity} \times \text{Discharge rate}}{F \times \text{Gravimetric surface area}} \tag{A.6}$$

where F is the Faraday constant.

Visualising the concentration overpotential

The concentration overpotential can be visualised by solving Fick's law with a constant flux boundary condition, as shown in Figure A.9A. The model was run until a fixed lithium surface concentration of $29\,000\,\text{mol}\,\text{m}^{-3}$ (equivalent to $350\,\text{mA}\,\text{h}\,\text{g}^{-1}$) was reached. This cut-off condition is analogous to the voltage cut-off typically used to determine the end of charge or discharge. In this simplified model, kinetic, electrolyte concentration and Ohmic overpotentials are ignored by assuming a fixed surface concentration at cut-off. In practice, these other overpotentials would reduce the surface concentration at which the cut-off voltage is reached.

Fick's law with a constant flux boundary condition shows us that the lithium concentration in the active material at cut-off will depend on the diffusivity of lithium in the active material, D, the flux, F_0, of lithium ions at the interface between active material and electrolyte, and the path length, l. By performing sweeps of these parameters, we can visualise the impact of these parameters on lithium concentration in the active material, and therefore capacity, at cut-off.

First, the impact of diffusivity was investigated for a fixed gravimetric charge rate of 0.5C (Figure A.9B). As the diffusivity of lithium inside the active material decreases, a steeper concentration gradient develops. For a fixed surface cut-off concentration of lithium, a steeper

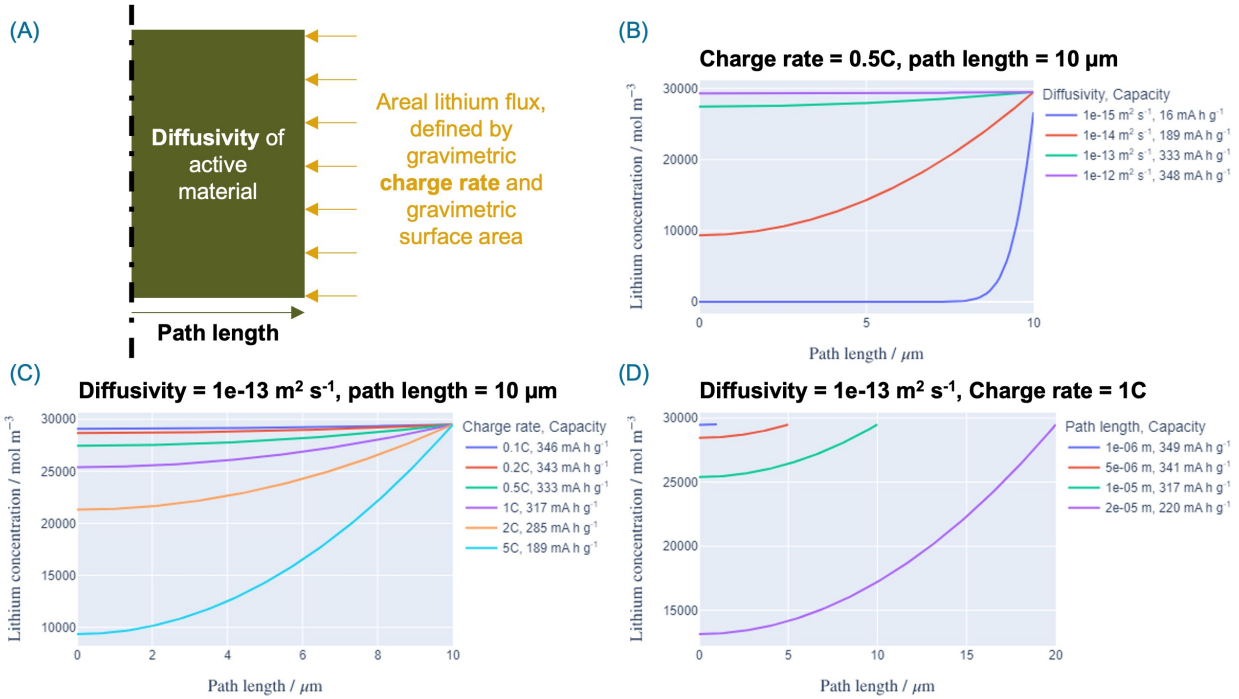


Figure A.9: Lithium concentration plotted as a function of path length when a surface concentration of 29 000 mol m^{-3} (equivalent to 350 mA h g^{-1}) was reached. The impact on the final lithium concentration profile of varying lithium diffusivity in the active material (B), charge rate (C), and path length (D) was investigated.

concentration gradient reduces the amount of lithium inside the active material, and therefore the capacity, at cut-off. As diffusivity is decreased, the effect on capacity is not linear. Only a small decrease (4%) in capacity is observed when diffusivity is decreased from 1×10^{-12} m^2 s^{-1} to 1×10^{-13} m^2 s^{-1}. However, when diffusivity is reduced from 1×10^{-13} m^2 s^{-1} to 1×10^{-14} m^2 s^{-1}, capacity falls by 43%, from 333 mA h g^{-1} to 189 mA h g^{-1}. Negligible capacity (16 mA h g^{-1}) is predicted at a diffusivity of 1×10^{-15} m^2 s^{-1}.

A similar non-linear reduction in capacity is observed as charge rate is increased (Figure A.9C). Diffusivity was fixed at a value of 1×10^{-13} m^2 s^{-1} and cut-off concentration profiles were calculated for a range of charge rates. Increasing charge rate by 5 times from 0.1C to 0.5C led to a reduction in capacity of 4%, from 346 mA h g^{-1} to 333 mA h g^{-1}. However, increasing the charge rate by 5 times from 1C to 5C led to a 40% reduction in capacity, from 317 mA h g^{-1} to 189 mA h g^{-1}.

Finally, the effect of path length on the concentration profiles is shown in Figure A.9D. As expected, for this fixed planar geometry a shorter path length is synonymous with a higher

gravimetric surface area, so areal flux is lower and a shallower concentration gradient is observed.

In summary, if a fixed surface cut-off concentration is assumed at the end of lithiation, then the concentration overpotential of an active material will depend on lithium ion diffusivity in the active material and the lithium ion flux at it surface. The magnitude of the lithium ion flux is a function of the gravimetric charge rate used for lithiation and the gravimetric surface area of the active material.